Interactions of Intrinsic Quantum Defects with a Nanoelectromechanical System

Thesis by
Mert Yuksel

In Partial Fulfillment of the Requirements for the
Degree of
Doctor of Philosophy

CALIFORNIA INSTITUTE OF TECHNOLOGY
Pasadena, California

2026
Defended August 7, 2025

Mert Yuksel
ORCID: 0000-0002-4141-4643

To my fellows

who lost their lives in the earthquake on February 6, 2023...

ACKNOWLEDGEMENTS

I would like to first thank my advisor, Michael Roukes, for his support and mentorship during the completion of this work. The vision and scientific perspective I have gained under his supervision have been deeply insightful and will remain invaluable for life. I am grateful for his encouragement of my ideas and for providing me with the independence to pursue *blue-sky* research, which ultimately led to the findings presented in this thesis.

Much of the work in this thesis is the result of a close and inspiring collaboration with Amir Safavi-Naeini and his group at Stanford, which I have greatly admired and enjoyed closely working with. I thank Amir for his great mentorship during our collaboration. It has been a pleasure to be part of their research environment, and I am sincerely grateful to him for his guidance.

I was privileged to work closely with Mark Dykman in understanding the experimental observations from a theoretical perspective and I thank Mark for sharing his great wisdom, knowledge, and experiences with me, which I have learned tons. I have greatly enjoyed our long chats to tackle problems which we had a shared excitement over, and I am looking forward to continuation of that.

There are many scientists, professors, engineers who have taught me or left a long lasting mark in my training in Caltech, or even before that. I thank Selim Hanay for training me to become an experimentalist during my studies at Bilkent University. Working with him has been one of the milestones of my scientific journey and I am grateful for his constant support. I thank my high school physics teachers Buket Turan and Yasar Aydogdu for encouraging and supporting me in science projects.

I thank our research group members who have taught me, helped me in different stages of my work, particularly Ewa, Warren, Jarvis, Laurent, Niki, Matt, Kirill, Marion, Jeff, Eric, Mark, Dvin, Tracy, Teresa, and all others.

This journey has also brought me great friendships that made the process smooth and more enjoyable. I thank Utku, my fellow companion, Scott, with whom we have lifelong bonded over many dramatic events (covid, wildfires, some unpleasant parts of PhD, etc.), Hirsh (the OG), Taylan, Alkim, Efe, Atakan, Andrea, Sahangi, Alex (pink), Cenk, Su, Bilge, Yannis, Pantelis, Alex (the Greek), Haroula, Arda, Batu, Saif, Prachi, Lucia, Aki, Shruti, Nicole, Solene, Yanky, Alea, Nikos, Nitay, Sophie, Kailah, Morgan, Tom, and everyone else I've crossed paths with along the

way at Caltech. I thank to the people in Stanford group who have also became great friends: Matthew, Oliver, Kaveh, Takuma, Felix, Samuel, Wentao, Sultan, and all others. I thank to my friends who we scattered to all over the world, but always kept in touch: Ozan, Muge, Gokhan, Cem, Orhun, Murat, Ozge, Hande, Mehmet, Onur, Selcuk, Ezgi, Suleyman and many more.

While the PhD has been a long journey in itself, the motivation and preparation that led me here were made possible through the contributions of many people. One thing I realized more clearly after coming to Caltech is how different people can approach problems — each with a different way of thinking. Some problems that seemed extremely difficult to me were solved effortlessly by others, while problems that felt natural to me challenged others. Reflecting on this, probably it makes sense—our brains form their neural connections differently, shaping distinct perspectives and strengths. For my own development, I am especially grateful to those who have helped my development from early years to now, starting with my family. They dedicated their lives to raising me and my sister Deniz, encouraging us and supporting our decisions at every stage. Although they come from non-scientific backgrounds, they gave everything they could to help me pursue my interests, and for that, I cannot thank them enough. I am grateful to have an amazing sister Deniz who has became an amazing medical doctor. İyi ki varsınız...

I thank all my other family members, cousins, aunts, uncles, for always checking on me and making me feel their constant support and giving me assurance that I have a great family looking after me. I would like to express my sorrowful respects and gratitude to all my family members and fellows who lost their lives in the earthquake in my hometown on February 6, 2023, where I spent great deal of my childhood.

It always amazes me how much you can learn from an animal, and I am grateful to have a very smart, supportive, and a bit crazy orange cat, Pasha. I thank my partner Dulce for bearing with me and always supporting me in every process since the day we have met. I have been very lucky to have such an amazing person always besides me, and looking forward to the next challenges and a life together with her.

ABSTRACT

Nanoelectromechanical systems (NEMS) resonators operating in the quantum regime provide a powerful platform for investigating mechanical motion at its most fundamental level. Their intrinsic ability to couple to environmental degrees of freedom, along with the long coherence times of their mechanical excitations (phonons), makes them particularly promising for quantum information and sensing applications. However, in this regime, the performance of NEMS resonators are predominantly affected by intrinsic material defects, acting as two-level systems (TLS). These quantum defects, ubiquitous in solid-state quantum devices at low temperatures, can exchange energy with their host field, causing dissipation and noise. Despite these dominant effects, the microscopic origin of such quantum defects is still unknown, and their interactions with phononic devices have been elusive.

Here, we present a detailed investigation into these interactions between quantum defects and phonons within piezoelectric lithium niobate NEMS resonator shielded by phononic crystals. We identify TLS defects as the primary source of excess noise at millikelvin temperatures, limiting their performance and sensitivity. By controlling the TLS frequency in situ with the application of electric field—and strain field due to piezoelectricity—we demonstrate strong resonant coupling between a mechanical mode of our NEMS resonator and a single, intrinsic TLS. Varying the resonant drive and/or temperature allows controlled ascent of the nonequidistant energy ladder and reveals the dressed states of the hybridized system. Fluctuations of the TLS on and off resonance with the mode induces switching between dressed and bare states; this elucidates the complex quantum nature of TLS-like defects in mesoscopic systems. We demonstrate that individual TLS defects can be precisely controlled and manipulated, transforming them from detrimental dissipation and noise sources into valuable quantum resources. The ability to harness this intrinsic nonlinearity of a nanomechanical resonator with quantum defects offers new directions towards quantum sensing and information.

PUBLISHED CONTENT AND CONTRIBUTIONS

[1] M. P. Maksymowych*, M. Yuksel*, O. A. Hitchcock, N. R. Lee, F. M. Mayor, W. Jiang, M. L. Roukes, and A. H. Safavi-Naeini, "Frequency fluctuations in nanomechanical resonators due to quantum defects", arXiv preprint arXiv:2501.08289 (2025),
M.Y. participated in the conception of the project, data collection and analysis, the characterization of the frequency noise, and the writing of the manuscript.

[2] M. Yuksel*, M. P. Maksymowych*, O. A. Hitchcock, F. M. Mayor, N. R. Lee, M. I. Dykman, A. H. Safavi-Naeini, and M. L. Roukes, "Intrinsic phononic dressed states in a nanomechanical system", arXiv preprint arXiv:2502.18587 (2025),
M.Y. participated in the conception of the project, prepared the experimental setup, performed the experiments, collected and analyzed the presented data, performed the simulations, and participated in the writing of the manuscript.

TABLE OF CONTENTS

LIST OF ILLUSTRATIONS

LIST OF TABLES

Chapter 1

INTRODUCTION

The work presented in this thesis investigates the fundamental physics and behavior of nanomechanical resonators operating at low temperatures where the mechanical vibrational energy consists of only a few phonons. Central to this study is a detailed exploration of intrinsic energy dissipation and frequency noise mechanisms, which currently limit the performance of these devices in quantum regime. At cryogenic temperatures, atomic-scale defects within solid-state materials emerge as the primary contributors to this dissipation and noise. By examining the interactions of these defects with the mechanical vibrations of a nanomechanical resonator, we aim to gain a deeper insight into the microscopic nature of these defects within phononic devices. The most direct approach to study these interactions is through the strong coupling of mechanical modes to individual defects—a key achievement of this work. Although typically viewed as sources of noise and loss, the intrinsic nonlinearity of these defects, once understood and controlled, offers promising avenues for novel quantum-limited sensing and quantum information applications.

As the experimental methods advanced to achieve cryogenic temperatures over the past century, there was a curiosity-driven race to explore and understand the physics of solid-state materials within the scientific community. These efforts have led to many breakthrough phenomenons, such as superconductivity, quantum Hall-effect, Josephson effect, etc. One of the anomalous behavior, which is very much related to this work, observed not long ago in 1970s was with heat capacity of amorphous glasses, as they universally vary linearly with temperature below 1 K compared to cubic dependence of crystal solids predicted by Debye theory [1]. The theoretical explanation for this behavior was given with the tunneling systems model, which suggests that the disordered atoms or group of atoms within the amorphous material can find themselves in two potentials that are both energetically favorable with a small difference and therefore can be modeled as two-level systems (TLS) [2, 3]. This model has worked very well to explain this behavior of the amorphous materials and still remains the dominant framework to describe the atomic 'defects' within the solids. Such states are abundant in amorphous solids whereas crystalline solids exhibit sparse density of tunneling sites [4].

The emergence and advancements in nanofabrication techniques have profoundly transformed low-temperature solid-state studies. These capabilities enable the fabrication of engineered devices with low dissipation in quite small volumes, containing a limited number of atoms, and consequently, a significantly reduced number of such defects compared to big bulk materials. This development has prepared the basis to allow the investigations of fundamental properties at the small ensemble and single-defect level.

Initial observations of the direct impact of these tunneling states demonstrated within the electromagnetic domain of circuit quantum electrodynamics (cQED) with superconducting microwave circuits. The studies done with Josephson junctions demonstrated that these microscopic TLS residing within the tunnel barrier cause decoherence and can strongly couple to qubits, leading to observable level splittings [5, 6]. In superconducting microwave resonators, experimental evidences showed that TLS residing at surfaces and interfaces of microwave resonators dictate the characteristic power and temperature dependence of resonator loss due to TLS interactions [7]. Later, superconducting qubits coupled to microwave resonators were employed as sensitive probes to individually study these intrinsic defects, allowing for characterization of their frequency distribution and quantum dynamics [8]. Strong coupling between an individual TLS defect and a microwave resonator, observed as a Rabi splitting, firmly established that TLS quantum impurities capable of coherently exchanging excitations with a microwave resonance mode.

Similar clear observations of individual TLS defect effects in phononic devices, such as nanomechanical resonators, presented greater experimental challenges. Further advancements were necessary, particularly in achieving higher mechanical frequencies to facilitate ground state cooling, higher quality factors, and developing more sensitive measurement techniques to detect the subtle interactions with individual defects. Advancements in nanofabrication eventually led to the miniaturization of mechanical resonators to the nanoscale, and with the emergence of advanced transduction schemes gave rise to nanoelectromechanical systems (NEMS) [9].

NEMS have emerged as a major type of dynamical mesoscopic system [10]. Beyond their fundamental appeal—given their compact size, long coherence time, and ability to sensitively detect force and motion—they provide a platform to study fundamental physics in solid-state materials and can be used for various applications in quantum technology [11–14]. Significant progress includes achieving quantum control of mechanical resonators at the single-phonon level [15] and demonstrating

quantum coherence and entanglement in mechanical systems [16–19]. The ability of mechanical resonators to interact with other quantum devices, such as qubits or superconducting microwave resonators, has important practical applications in quantum information and metrology, serving as quantum sensors [20], memories [21], or transducers [22] for interfacing different types of quantum systems. The development of phononic crystal (PnC) resonators has further enhanced quantum acoustics by increasing phonon lifetimes [12] and enabling single-quantum exchanges between qubits and mechanical oscillators [13]. As the NEMS devices have started to operate in low phonon number with the advancements in the field, the analogous TLS effects observed in cQED with microwave photons have also started to emerge in mechanical devices. The similar TLS induces dissipation and the resonance frequency shift below 1 K due to these interactions were experimentally demonstrated more recently [23].

In this thesis, we delve into exploring of these interactions of intrinsic TLS defects with mechanical vibrations of our NEMS PnC resonators in the means of understanding the fundamentals of TLS-phonon interactions. We develop an in-situ control of energy levels of TLS defects by strain tuning and use this method to bring individual TLS onto resonance with the mechanical mode. This gives us a very useful tool to use the mechanical mode as a probe for the TLS defects. We reveal that this strong coupling to intrinsic TLSs can be very strong and stable and therefore can have important applications for quantum information and sensing. As the TLS induces a nonlinearity, the TLS-mechanical mode system is analogous to hybrid microwave qubit-mechanical mode systems. We analyze this intrinsically available TLS induced nonlinearity in details and discuss its applications. Besides the strong coupling, we also observe telegraph noise at low temperatures due to these defect interactions. Our analysis brings new insights to the physics of such defects.

Besides the strong coupling and the work done with individual TLS, our work also focuses on characterization of frequency fluctuations in our NEMS resonator at low temperatures. We study the increasing noise behavior observed below 1 K with careful power and temperature sweep analysis and find the evidences of telegraph switching behavior due to individual TLS. We study the spectral diffusion of the frequency response of the mechanical mode due to these defects.

At the core of it, the work done in this thesis aims to increase our knowledge in understanding material defects in solids and their interactions with mechanical vibrations. Although these TLS defects have a bad reputation in modern quantum

devices as they are known to be a source of noise and dissipation, having control over them individually and harnessing their intrinsic nonlinearity, as demonstrated in this work, can have important applications in future devices. Most of the effort today has been focused on mitigating these defects by trying to perfect the fabrication and having perfect crystal structures, but we argue that a foundational understanding of these material defects must come first—guided by the famous saying "know your enemy." When we look at the literature, it is clear that phononic systems are coming from behind compared to photonic devices in cQED in terms of understanding the phonon-TLS interactions. This work also aims to close this knowledge gap in phononic devices.

The outline of the thesis follows this sequence. We start with introducing the fundamental concepts that are key to understanding the main results in the second and third chapter. In the fourth chapter, we go over the experimental setup and instrumentation used for the low temperature measurements performed with our NEMS devices. Fifth chapter covers the strong coupling experiments and results in details, and the sixth chapter focuses on the frequency fluctuations analysis. The last chapter briefly explains the efforts for NEMS mass sensing in quantum regime and conclude with some future motives and directions.

Chapter 2

NANOELECTROMECHANICAL SYSTEMS

This introductory chapter aims to provide the background in nanoelectromechanical systems (NEMS) that is essential for understanding the experiments and analyses presented in the chapters that follow. It begins with a brief review of NEMS and its development over the last 30+ years. Following this, we focus on one of the most prominent applications of NEMS in mass sensing. The focus then shifts from the classical to the quantum as we delve into the behavior of NEMS devices in the quantum regime. We briefly discuss the quantization of mechanical motion into phonons and their promising applications in quantum science and technology. Finally, we discuss the vision of having NEMS devices for sensing in quantum regime.

2.1 Brief Introduction to NEMS Resonators

Advancements in nanofabrication, the enhancements in the ability to shape, develop, construct the solid-state materials with nano-scale precision, have led to the miniaturization of mechanical resonators, giving rise to nanomechanical systems. One of the first examples of NEMS resonators were made in 1991 in Bell Labs by using GaAs with dimensions of 4 μm doubly-clamped beam [24]. This pioneering development highlighted the profound insight that confining mechanical motion within exceptionally small volumes, typically on the order of a few cubic micrometers (μm^3), could lead to the study of fundamental physics related to mechanical motion (phonons) in solid-state materials, such as heat transport, energy dissipation mechanisms, etc. Furthermore, it has promised to enable numerous practical applications due to the unprecedented sensitivity achievable at these scales.

The initial key challenge involved how to readout and how to excite the mechanical vibrations above the thermal excitations. One of the first method employed was magnetomotive [25] detection. Over the years, there have been many actuation and detection methods developed [26], such as optical [27, 28], piezoelectric [29, 30], piezoresistive [31], electrothermal [32], and capacitive [33] schemes. The successful integration of these actuation and sensitive detection methods marked the establishment of Nano-electro-mechanical systems (NEMS) [9].

Each transduction method ultimately serve to convert small mechanical vibrations into an electrical signal (voltage or current) for readout, or vice versa for actuation, which is demonstrated in Fig. 2.1. For example, piezoresistive detection measures the small resistance changes due to geometrical changes at the strain gauges with the mechanical motion, optical methods typically analyze the reflected or scattered light from the NEMS resonator's surface, often utilizing principles like the Doppler effect or interferometry, to precisely quantify its mechanical displacement or velocity, and piezoelectric methods directly harness the piezoelectric effect, converting mechanical strain within the material into an electrical charge or voltage. Each transduction approach possesses its own set of advantages and disadvantages, and can be more suitable for specific applications and operational environments.

Understanding the various noise processes in these devices is a critical aspect of NEMS design, as noise ultimately limits the minimum detectable motion. As it is depicted in Fig. 2.1, beyond intrinsic noise of the nanomechanical resonator, additional noise is introduced at every practical stage of operation. These different types of noises include, starting with the source noise from the actuation signal, transduction noise, thermomechanical noise, readout amplifier noise are the most known and studied sources of noises. Therefore, mitigating these combined noise sources has long been a primary objective for advancing NEMS technology.

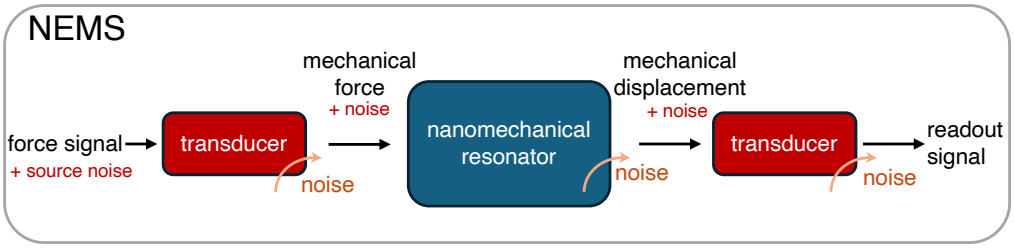

Figure 2.1: **NEMS Transduction.** A block diagram illustrating the fundamental operation of a NEMS device. An input transducer converts an external force signal into a mechanical force that excites the nanomechanical resonator. A second transducer detects the resulting mechanical displacement and converts it back into an electrical readout signal. Different noise processes take place at each stage.

The small size of NEMS resonators gives rise to high natural frequencies and low dissipation rates. In the field, there has been active research to increase the operation frequencies while also lowering the dissipation rates, as the combination of those two leads to more sensitive NEMS devices that can also achieve ground state cooling. This pursuit has led to significant advances in both the NEMS technology and also

in material science as different materials were tested to achieve this purpose. While foundational work relied heavily on silicon, the field has expanded to a diverse palette of materials, including silicon nitride, graphene and piezoelectric materials like aluminum nitride, quartz, and lithium niobate.

Early progress involved simply scaling down conventional structures like nanobeams. However, this approach has its limits, as beams become smaller and stiffer, it gets progressively harder to actuate and detect their motion due to increases in clamping effects. To overcome these scaling challenges, researchers also developed non-suspended designs like surface and bulk acoustic wave resonators which can achieve very high frequencies with relatively simple fabrication, but they often come with the trade-off of higher dissipation through acoustic radiation into the substrate.

More recently, drawing inspiration from photonic crystals (PnC) in optics, a NEMS resonator has emerged equipped with the phononic crystal shields and superconducting transducers. Combined with the strong piezoelectricity of lithium niobate and implementation of piezoelectric transduction, this device dramatically boosts the quality factor, while achieving GHz frequencies. The device at the heart of this work, fabricated from lithium niobate by the group led by Amir Safavi-Naeini at Stanford University, sits at this technological frontier and allowed us to perform the measurements presented in this thesis.

PnC NEMS resonators have emerged as a distinct class of nanomechanical devices that are engineered to control how the acoustic waves propogate. Analogous to photonic crystals that control light propagation by creating bandgaps for photons, PnCs are patterned periodic structures designed to manipulate mechanical vibrations (phonons) by introducing phononic bandgaps where phonon propagation is forbidden [34–36]. The primary advantage of PnC structures lies in their ability to effectively confine mechanical energy. By creating a defect or cavity within the periodic phononic lattice, phonons can be localized to the defect region, while propagation into the supporting anchors is suppressed due to the acoustic bandgap [37]. This leads to a boost in quality factor, as the clamping losses are eliminated by the PnC.

In Fig. 2.2, we demonstrate an example PnC structure which consists of repeating periodic array of a unit cell consisting of a large structure with higher mass, and the connector, narrow tether, with smaller mass. The bandgap arises from the presence of modes of oscillation with widely differing frequencies within the periodic lattice. Specifically, traveling phonon modes where the larger masses are predominantly

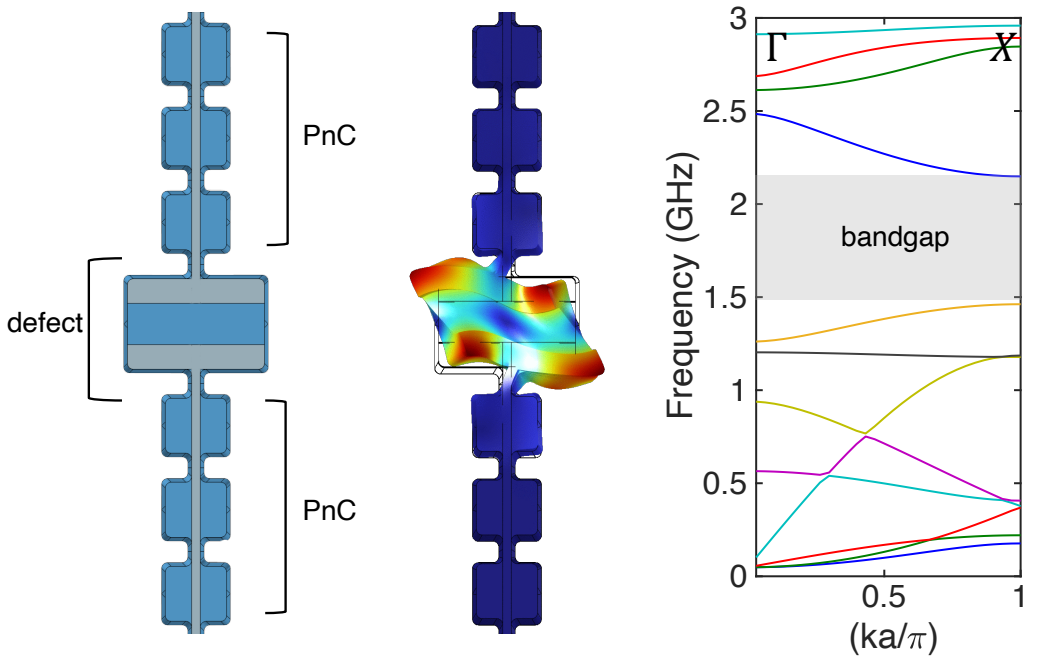

Figure 2.2: **Phononic Crystal Resonators.** A schematic of the PnC device architecture. A central defect region is designed to act as the resonator, while the surrounding periodic structures serve as PnC shields. A finite-element method (FEM) simulation at the center showing the fundamental shear mode shape. The vibrational energy is spatially confined within the defect region. The calculated phononic band structure for the periodic PnC shield material [23]. The shaded area indicates the phononic bandgap. The resonator's mode is engineered to have a frequency that falls within this bandgap.

excited result in low-frequency and these are distinctly split in frequency from modes where the tethers are predominantly excited, leading to high-frequency. The frequency bandgap, representing the range of forbidden vibrations between these low and high-frequency modes, becomes more pronounced with increasing difference in the effective masses within the unit cell.

PnC structures have became popular choice for high-Q optomechanical crystals, where carefully designed PnC cavities co-localize optical and mechanical modes to enable strong photon–phonon coupling, ground-state cooling, and coherent state transfer [12, 38, 39]. More recently, PnC strategy has been adopted in piezoelectric [37, 40] and electrostatic [14] NEMS resonators. As we shall see in the following chapters, these PnC NEMS resonators have become an essential tool for exploring mesoscopic physics, particularly in the quantum regime.

2.2 NEMS Mass Sensing Applications

Due to their small footprint, high frequency, low dissipation rates, and the implementation of effective actuation/detection methods, NEMS resonators have emerged as a great tool for mass sensing [41]. The fundamental principle relies on the relationship between the resonators mass and its resonant frequency. In classical regime, NEMS resonator can be modeled as a simple mass-spring-damper model with its resonance frequency ω_0 can be expressed as

$$\omega_0 = \sqrt{\frac{k_{\text{eff}}}{m_{\text{eff}}}} \tag{2.1}$$

where k_{eff} is the effective spring constant (stiffness) of the mechanical resonator and m_{eff} is the effective mass. Any additional mass δm absorbed onto the resonator's surface causes a change in its effective mass, therefore shifting its frequency. This frequency shift $\Delta\omega$ is proportional to added mass, given by

$$\Delta\omega \approx -\frac{\omega_0}{2}\frac{\delta m}{m_{\text{eff}}} = \delta m \mathcal{R} \tag{2.2}$$

where $\mathcal{R}$ is the mass responsivity (Hz/kg) of the NEMS resonator. This simple equation driven with a very simple idea highlights that NEMS resonators can detect minute mass changes thanks to their high resonant frequency ω_0 and a small effective mass m_{eff}. The mass sensitivity of NEMS resonators improved significantly over the years [42, 43] and this remarkable capability has enabled NEMS-Mass Spectrometry (NEMS-MS) applications such as the detection of individual nanoparticles [44], single proteins [45]. Beyond merely measuring mass, NEMS-MS technology has advanced to enable inertial imaging by utilizing frequency shifts from multiple vibrational modes [46]. This technology has proven itself to work even in nonlinear regime [47], and atmospheric pressure [48]. While the NEMS-MS platform relied on well-known mode shapes of the resonator to extract the mass of the adsorbed analyte, finger-printing method has been recently demonstrated which is more suitable to use with multi-mode 2D PnC resonators [49].

While these achievements demonstrate the powerful capabilities of NEMS mass sensors in classical regime, their ultimate sensitivity is fundamentally limited by the noise processes since it determines the minimum detectable shift in the resonance frequency. There has been many experiments and studies performed to understand these noise processes in NEMS resonators. We can consider two class of noise

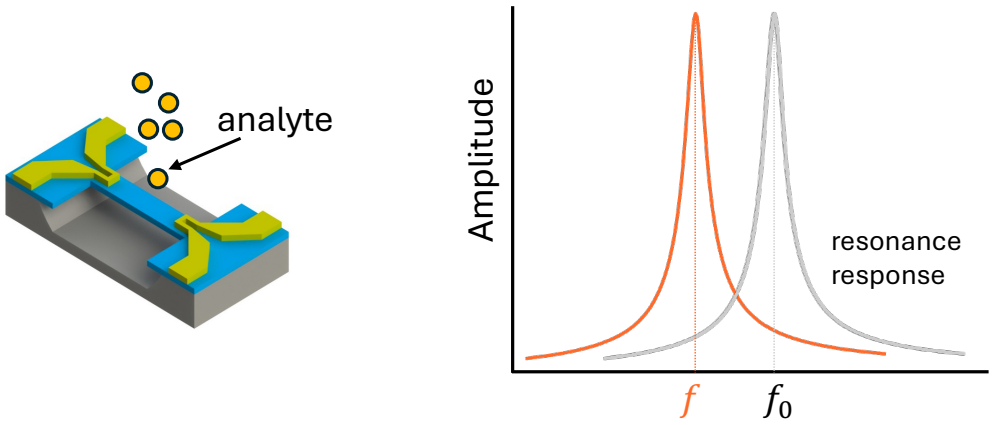

Figure 2.3: **NEMS Mass Sensing.** The basic principle of NEMS mass sensing is sketched. The adsorption of an analyte onto a NEMS resonator (left) increases its effective mass. This added mass results in a measurable downward shift in the resonance frequency from its initial value, f_0, to a new value, f (right), allowing for the quantification of the analyte's mass.

processes: intrinsic noise, which is fundamental to the resonator's mechanical properties (e.g., thermomechanical noise, surface diffusion noise, and two-level system (TLS) noise), and extrinsic noise, which originates from the transducer and readout circuitry. Most of the modern NEMS resonators have been limited by external effects, and there has been an effort to understand the intrinsic limitations, particularly thermomechanical noise, of these mesoscopic systems [41, 50].

Thermomechanical noise arises from the thermally driven random motion of the mechanical device, that can be quantitatively understood through the fluctuation-dissipation theorem [51]. Using our one dimensional harmonic oscillator model for NEMS resonator with effective mass m_{eff} and effective spring constant $k_{\text{eff}} = m_{\text{eff}}\omega_0^2$, the mean square displacement fluctuation $\langle x_{\text{th}} \rangle$ due to thermal energy of the bath can be written by

$$\frac{1}{2} m_{\text{eff}} \omega_0^2 \langle x_{\text{th}}^2 \rangle = \frac{1}{2} k_B T \tag{2.3}$$

where k_B is the Boltzmann's constant. Following the derivation from [41], for a mechanical resonator with a readout by phase-locked loop that keeps the resonant amplitude fixed at x_c, the mass sensitivity can be expressed as

$$\delta M \approx 2M_{\text{eff}} \left(\frac{k_B T}{m_{\text{eff}} \omega_0^2 \langle x_c^2 \rangle} \right)^{1/2} \left(\frac{\Delta f}{Q \omega_0} \right)^{1/2} \tag{2.4}$$

This formulation indicates that, for a nanomechanical resonator primarily limited by thermomechanical noise, the mass sensitivity can be significantly enhanced by a higher quality factor Q, a larger characteristic amplitude (x_c) or dynamic range, a higher resonant frequency (ω_0), and lower effective mass (m_{eff}). Therefore, this provides a strong motivation for the fabrication of lower mass NEMS resonators operating at high frequencies and low temperatures. Combined with superconducting transduction methods, which inherently increases the quality factor, low temperature NEMS operations might in fact considered appealing. However, as we shall see in the following chapters, this is not the case and this idealized scenario is often complicated by other dominant noise mechanisms, particularly those arising from two-level tunneling systems (TLS) in material defects. Before delving into these complexities, it is essential to first establish a foundational understanding of NEMS in the quantum regime.

2.3 NEMS in Quantum Regime

NEMS devices have long been envisioned as crucial platforms for investigating the fundamental principles of condensed matter physics and quantum mechanics [11], ever since their emergence. Realizing this potential, however, critically depends on operating these macroscopic mechanical systems within the quantum regime. This regime is achieved when the thermal energy ($k_B T$) is lower or comparable to single quanta of mechanical vibrational energy ($\hbar\omega_0$), so that NEMS can only have few phonons. While having a high frequency NEMS device and lowering the bath temperature in a cryogenic setup seems as a straightforward solution, having an efficient mechanical to electrical domain transduction which will be capable of measuring single phonon excitation while not increasing the temperature of the device has also been a critical challenge.

A pivotal advancement in addressing this challenge has been the successful ground-state cooling of NEMS device, achieved by coupling the resonator to a superconducting qubit. In this approach, the qubit is driven to preferentially absorb energy from the resonator, and can cool the mechanical resonator by extracting phonons. Ground state cooling of a NEMS resonator was achieved with various methods, by coupling to a optical cavity [52], phonon cavity electromechanics [53], squeezing mechanical motion [54], and coupling to superconducting qubits [16, 18]. Most

recently, the nonlinearity from transmon qubits has been exploited to directly resolve the energy levels of a PnC NEMS resonator [13].

NEMS devices are exceptionally well-suited for this type of quantum coupling due to several inherent advantages. Their nanoscale dimensions, high mechanical quality factors, and high resonant frequencies make them an attractive platform for strong motional coupling to other quantum systems, such as superconducting qubits and microwave or optical resonators. These features have significantly attracted researchers from the quantum information field, leading to the exploration of NEMS devices as potential quantum memories [55] and as transducers [56] for efficient conversion between microwave and optical photons.

While the operation of NEMS devices in the quantum regime has been gaining popularity for quantum information processing applications, they have also proven invaluable platforms for studying the fundamentals of quantum mechanics itself. As in any solid-state material, the performance of NEMS resonators in the quantum regime is significantly affected by energy exchange with two-level system (TLS) defects inherent within their materials. A clear evidence of this interaction was explored in studies investigating the loss channels in piezoelectric PnC resonators [23] and the increased loss and frequency red-shift observed below 1K is contributed to TLS interactions. Consequently, NEMS resonators operating in the quantum regime serve as ideal platforms to investigate complex phonon physics and the nature of TLS interactions, topics we will delve into in greater detail in the following chapters.

2.4 Quantum Sensing with NEMS

As NEMS technology continues to develop within the quantum regime, it holds great potential for the ultrasensitive detection and characterization of individual small particles, particularly proteins, extending beyond mass sensing [57]. This capability can open new opportunities for a deeper understanding of proteomics [58]. From a physics perspective, proteins can be modeled as intricate, nature-made nano structures, comprised of various combinations of carbon, hydrogen, oxygen, nitrogen, and sulfur atoms, along with specific functional groups (e.g., amino, carboxyl) depending on the protein type. Some proteins even contain single heavy metal atoms (e.g., an iron atom in hemoglobin), effectively acting as a nature-made atomic-scale trap. These complex, solid-state protein structures possess their own intrinsic vibrational modes and structural resonances. In the quantum regime, where thermal noise is minimized and quantum interactions become dominant,

the subtle energy exchange and coherent coupling between NEMS resonators and these molecular structures can become significantly more apparent and measurable. Therefore, this rapidly developing technology presents a transformative potential for advancing proteomics, enabling characterization at an unprecedented single-molecule level.

While the sensing and characterization of proteins with NEMS in the quantum regime represents the ultimate goal of our group's vision, achieving this demanding level of performance first requires a deeper understanding of NEMS devices operating in this regime. This critical understanding can only be attained by studying the interactions between the NEMS device and TLS defects, as these are currently recognized as the dominant source of energy dissipation and decoherence in such systems. In the following chapter, we will therefore cover the TLS model of these material defects, before delving into their interactions with our NEMS resonators.

Chapter 3

TUNNELING SYSTEMS IN SOLIDS AT LOW TEMPERATURES

In the early 1970s, the physics community was puzzled with the anomalous properties of amorphous solids at low temperatures. The experiments performed with different glasses at liquid helium temperatures demonstrated that the specific heat of amorphous solids *universally* varies nearly linearly (T) with temperature below 1 K [1]. The Debye model which sufficiently explains the temperature dependence of specific heat of crystalline materials (T^3) was not adequate for this observed behavior in disordered solids. Within few years, the "tunneling model" was suggested [2, 3] and proven to be a useful model to describe the properties at low temperatures. After many years of research and experiments, it has been known that the low-temperature properties of solids largely influenced by the contribution or interaction with tunneling systems [4].

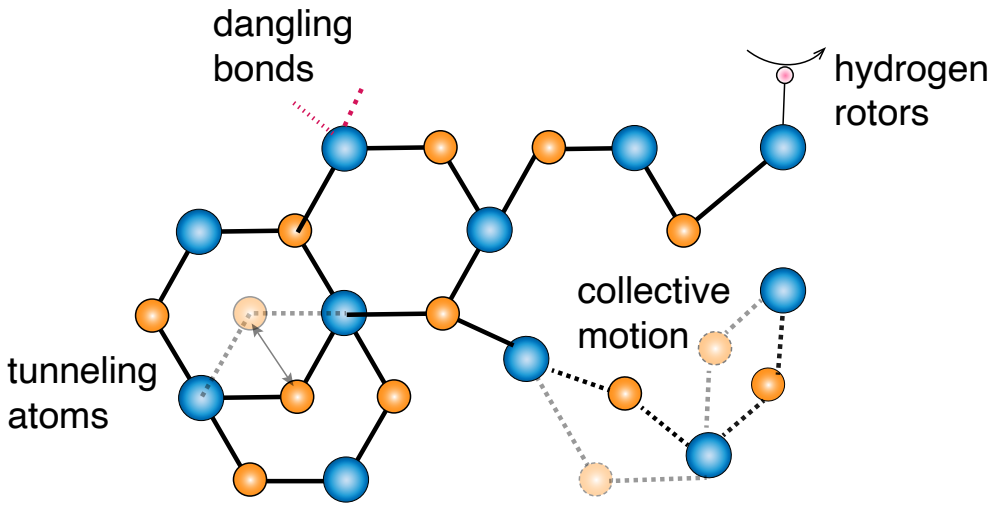

Figure 3.1: **TLS Defects Models from Literature.** Depicted here are several atomic-level models for the formation of TLS defects within a solid. Examples include individual atoms or group of atoms undergoing quantum tunneling, exhibiting collective motion, and the influence of structural imperfections such as dangling bonds and hydrogen defects [59].

The microscopic nature of these tunneling systems remains one of the important open questions in condensed matter physics to date. The standard tunneling model (STM) predicts that atoms, a group of them, or more complicated atomic structures

can have two nearly degenerate configurations energy states separated by a barrier, modeled as a particle in double-well potential [60] and simply defined as a two-level system (TLS). While amorphous materials host an abundant number of TLSs, similar tunneling states can also manifest from atomic-scale defects within crystalline materials, on surfaces, and at material interfaces [61–63]. Some of the example mechanism is demonstrated in Fig. 3.1. The properties of these TLS defects are influenced by their local environment in the disordered atomic lattice. Due to a wide-range of local environment, their potential barrier varies and, therefore, their energies and relaxation times. The standard tunneling model assumes very broad intrinsic parameters of the TLS's.

TLS defects have been observed and studied in various quantum devices, including circuit QED systems, microwave resonators, optical cavities, superconducting qubits, and nanomechanical resonators. As a TLS behaves like a nonlinear quantum object, its interaction with bosonic fields is of particular interest for applications in quantum sensing and information processing. However, in many applications, TLS-induced defects are a significant source of noise and decoherence and are avoided. Nevertheless, these interactions are unavoidable with the current technology and a thorough understanding of their behavior is essential. This work aims to characterize and understand TLS interactions within the mechanical domain using our NEMS resonators. In this chapter, we will quantitatively analyze how a TLS couples to a phononic field.

3.1 Two-Level System Model

According to the standard tunneling model, a TLS is represented by a double-well potential demonstrated in Fig.3.1. Key parameters defining this system are the tunneling energy between two wells, denoted as Δ_0, and an asymmetry energy ε, which represents the energy difference between the two minima of the wells. The tunneling rate Δ_0 represents the coupling between the two states, and using Wentzel-Kramers-Brillouin (WKB) approximation, it is expressed as

$$\Delta_0 = \hbar\omega_0 e^{-\lambda} \tag{3.1}$$

where λ is the tunneling parameter. λ can be written in terms of the double-well potential parameters as

$$\lambda = \sqrt{\frac{2mV}{\hbar^2}}d. \tag{3.2}$$

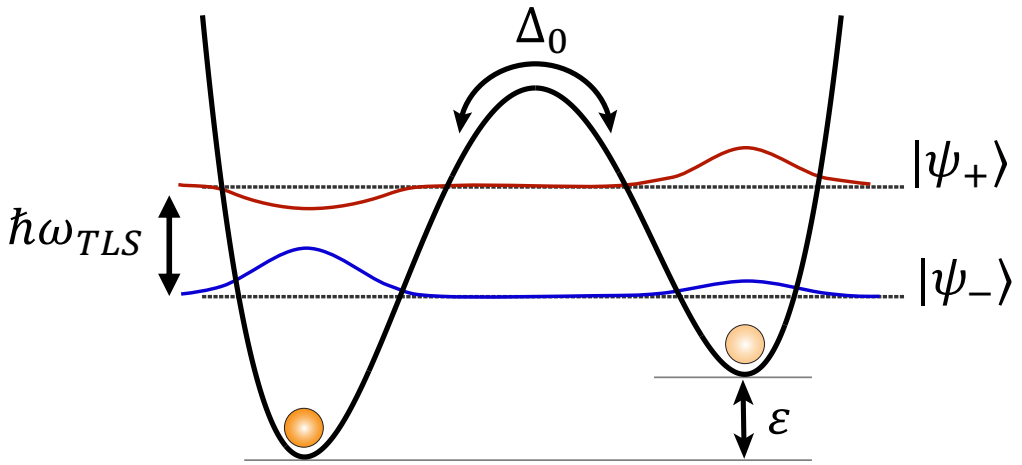

Figure 3.2: **Double-well Potential Model for a TLS.** The double-well potential energy landscape for a TLS. A particle can reside in two minima separated by an energy barrier. The energy difference between the two-wells is the asymmetry energy ε and quantum tunneling between these wells is characterized by the tunneling energy Δ_0. The energy eigenstates, $|\psi_+\rangle$ and $|\psi_-\rangle$, are formed by superpositions of the localized states, with an energy separation given by $\hbar\omega_{TLS}$.

Here, m denotes the mass of the particle, V is the barrier height relative to the energy minima, and d is the separation between the two minima along the configurational coordinate. These tunneling states arise from various local atomic configurations and structural rearrangements which leads to a wide spectrum of parameters of Δ_0 and ε.

According to this framework, the asymmetry energy is assumed to have a uniform distribution which suggests that any two local configurations are equally likely within a certain range [4, 59]. On the other hand, the exponential dependence on the tunneling parameter λ means that Δ_0 can span many orders of magnitude even for small variations in barrier height or width. Therefore, it is generally assumed that Δ_0 is logarithmically distributed. A key assumption of the tunneling model is that [2, 3] the density of states $P(\varepsilon, \Delta_0)$ for the TLS should be a constant in terms of the parameters ε and λ:

$$P(\varepsilon, \lambda) d\varepsilon d\lambda = P_0 d\varepsilon d\lambda \tag{3.3}$$

where P_0 is the constant density. It is convenient to use as independent variables Δ_0 and ε:

$$P(\varepsilon, \Delta_0)\, d\varepsilon\, d\Delta_0 = \frac{P_0}{\Delta_0}\, d\varepsilon\, d\Delta_0. \tag{3.4}$$

We can define a convenient basis for this system: $|L\rangle$ and $|R\rangle$, which represent the particle localized in the left and right potential well, respectively. Hamiltonian of such a system is

$$H_{\text{TLS}} = \frac{1}{2}\begin{pmatrix} -\varepsilon & \Delta_0 \\ \Delta_0 & \varepsilon \end{pmatrix}. \tag{3.5}$$

By using the Pauli operators

$$\sigma_x = \begin{pmatrix} 0 & 1 \\ 1 & 0 \end{pmatrix} \quad \text{and} \quad \sigma_z = \begin{pmatrix} 1 & 0 \\ 0 & -1 \end{pmatrix} \tag{3.6}$$

we can write the standard compact form of the TLS Hamiltonian:

$$H_{\text{TLS}} = -\frac{\varepsilon}{2}\sigma_z + \frac{\Delta_0}{2}\sigma_x. \tag{3.7}$$

Solving for the eigenvalues of this Hamiltonian, we find the energy levels of

$$E_{\pm} = \pm\frac{1}{2}\sqrt{\varepsilon^2 + \Delta_0^2} \tag{3.8}$$

and the energy difference between these two states, referred as energy splitting, is denoted by

$$\Omega \equiv \hbar\omega_{\text{TLS}} = \sqrt{\varepsilon^2 + \Delta_0^2} \tag{3.9}$$

and this definition allows us to write the energy eigenvalues as $E_{\pm} = \pm\Omega/2$. The TLS Hamiltonian takes a diagonal form with these eigenvalues on its diagonal:

$$H_{\text{TLS}} = \frac{1}{2}\hbar\omega_{TLS}\sigma_z. \tag{3.10}$$

The true eigenstates of the Hamiltonian can be written as superpositions of the local eigenstates $|R\rangle$ and $|L\rangle$ as;

$$|\psi_-\rangle \equiv |g\rangle = \cos(\alpha)|L\rangle - \sin(\alpha)|R\rangle \tag{3.11}$$

$$|\psi_+\rangle \equiv |e\rangle = \sin(\alpha)|L\rangle + \cos(\alpha)|R\rangle \tag{3.12}$$

where the mixing angle 2α is defined by the ratio of the tunneling energy to the asymmetry:

$$\tan(2\alpha) = \frac{\Delta_0}{\varepsilon}. \tag{3.13}$$

Therefore, angle α characterizes how the original localized states are mixed to form the true energy eigenstates of the TLS.

This basic formulation provides the fundamental structure of the TLS model. By leveraging the derived density of states, one can show that materials containing TLS defects exhibit a specific heat $C_V \propto T$ at low temperatures, a deviation from the Debye model's T^3 dependence. While this chapter focused solely on the intrinsic properties of TLS, our primary interest lies in their interactions with the environment and phonons, which will be explored in detail in the following section.

3.2 TLS Interactions

In amorphous materials, the ensemble of TLS defects interacts with oscillating fields, such as the electric field in a microwave resonator or the strain field in a mechanical resonator. This interaction is the microscopic origin of both energy dissipation and a temperature-dependent shift in the device's resonance frequency at low temperatures. The nature of this interaction can be separated into two distinct types: a resonant (on-resonance) process that governs energy loss, and a dispersive (far-from-resonance) process that governs frequency shifts.

The primary mechanism for energy loss at low temperatures and low powers is the resonant absorption of energy quanta by TLS. This occurs when the energy of TLS is in close proximity of the resonance frequency (ω_r). A TLS in its ground state can absorb energy (a phonon) and transition to its excited state, effectively removing energy from the resonator field. This dissipative process is described by the TLS-induced loss tangent, δ_{TLS}. The loss tangent depends on both temperature (T) and the average number of photons in the resonator (n), as described by Eq. (3.14):

$$\delta_{TLS}(n,T) = \frac{\delta^0_{TLS}\tanh\left(\frac{\hbar\omega_r}{2k_BT}\right)}{\sqrt{1+n/n_c}} \tag{3.14}$$

where δ^0_{TLS} is the intrinsic loss tangent, the term in the numerator reflects the population difference between the ground and excited states of the resonant TLS, as dictated by Boltzmann statistics, and term in the denominator describes the power dependence where n_c is the critical photon number.

The quality factor limited by TLS interactions, shown in Eq. (3.15), is given by [23]:

$$Q_{TLS}(n,T) = \frac{1}{\delta_{TLS}(n,T)} = \frac{\sqrt{1+n/n_c}}{\delta^0_{TLS}\tanh\left(\frac{\hbar\omega_r}{2k_BT}\right)}. \tag{3.15}$$

This equation clearly shows that the Q-factor increases (loss decreases) with both increasing temperature and increasing drive power, which are hallmark signatures of TLS-dominated loss in resonant devices.

While resonant TLS cause dissipation, the vast majority of TLS are off-resonant ($\omega_{TLS} \neq \omega_r$). These TLS cannot easily absorb energy from the field directly. Instead, they undergo a dispersive interaction, where they are virtually excited and de-excited by the driving field. This collective interaction of the entire off-resonant TLS ensemble alters the effective dielectric constant or elastic modulus of the host material. Since the resonance frequency of a device depends on its material properties, this change manifests as a temperature-dependent shift in the resonance frequency, ω_r.

This fractional frequency shift is described by Eq. (3.16):

$$\frac{\Delta\omega_r(T)}{\omega_r(T_0)} = \frac{\delta^0_{TLS}}{\pi}\left[\mathrm{Re}\left(\Psi\left(\frac{1}{2}+\frac{\hbar\omega_r}{2\pi i k_BT}\right)\right) - \ln\left(\frac{\hbar\omega_r}{2\pi k_BT}\right)\right]^T_{T_0}. \tag{3.16}$$

This relation tells us that the magnitude of the frequency shift is proportional to the same intrinsic loss tangent, δ^0_{TLS}, that governs the resonant loss. This is expected because they are two consequences of the same underlying TLS defect population, just at different frequencies. The complex expression involving the Digamma function (Ψ) and the logarithm arises from integrating the dispersive response over the entire energy distribution of the off-resonant TLS. This mathematical form accurately predicts the characteristic logarithmic temperature dependence of the frequency shift

observed at low temperatures, which transitions to a different behavior at higher temperatures ($k_B T \gtrsim \hbar\omega_r$).

In summary, the resonant interaction with a small fraction of TLS leads to energy loss ($1/Q$), while the collective dispersive interaction with the entire population of off-resonant TLS leads to a temperature-dependent resonance frequency. We observe these affects in our experiments discussed in next chapters.

3.3 Strong Coupling Model

Here, we will quantitatively study when a single TLS strongly interacts with a phononic mode of a nanomechanical resonator.

In the linear regime, each mechanical vibration mode of the NEMS resonator can be modeled as a quantum harmonic oscillator with a vibrational frequency ω_m. The Hamiltonian for this single mechanical mode is then written as

$$H_{\mathrm{m}} = \hbar\omega_m a^\dagger a \tag{3.17}$$

where $\omega_m/2\pi$ is the frequency of the mechanical mode, and a ($a^\dagger$) are the annihilation (creation) operators. The Hamiltonian is proportional to the number operator $N = a^\dagger a$ and its eigenstates ($|n\rangle$) known as Fock states (or number states) $|n\rangle$ corresponds to an energy $E_n = \hbar\omega_m n$ yielding an equally spaced ladder of energy levels. The difference between consecutive levels is ($\hbar\omega_m$), representing the energy of a single phonon. At a cryogenic stage temperature of roughly 10 mK, the unperturbed mechanical mode primarily remains in its ground state ($|0\rangle$). Occasional phonon excitations may arise through thermal processes, and can also be actively driven by an external field.

We revisit the TLS Hamiltonian we derived in Eq.3.10 and introduce TLS raising (lowering) operators:

$$\sigma_+ = |e\rangle\langle g| \text{ and } \sigma_- = |g\rangle\langle e| \tag{3.18}$$

which represents the excitation from $|g\rangle$ to $|e\rangle$ and the relaxation from $|e\rangle$ to $|g\rangle$, respectively. For convenience when modeling energy exchange with the resonator, we shift the energy scale to set the ground state $|g\rangle$ to zero energy, resulting in the Hamiltonian:

$$H_{\mathrm{TLS}} = \hbar\omega_{\mathrm{TLS}}\sigma_{+}\sigma_{-}. \tag{3.19}$$

TLS can couple to the mechanical motion of the resonator through the local strain field. As the resonator vibrates, it creates an oscillating strain, S, which in turn can modulate the energy levels of the TLS. The magnitude of the strain is proportional to the resonator's displacement, which is described in the quantum picture by the operator $x = x_{\mathrm{zpf}}(a + a^{\dagger})$, where x_{zpf} is the zero-point fluctuation amplitude of the mechanical mode.

The interaction between the TLS and the strain field can be described by an interaction Hamiltonian, H_{int}. In the most general case, the strain can both shift the energy splitting of the TLS and induce transitions between its ground and excited states. These two effects are known as longitudinal (σ_z and transverse (σ_x) coupling, respectively.

The *transverse* coupling is essential for the coherent exchange of energy and can be expressed using the raising and lowering operators as $\sigma_x = \sigma_{+} + \sigma_{-}$. The transverse interaction Hamiltonian is therefore:

$$H_{\mathrm{int,x}} = \hbar g_x(\sigma_{+} + \sigma_{-})(a + a^{\dagger}). \tag{3.20}$$

Here, g_x is the transverse coupling rate. This is the term that enables the resonant exchange of a single phonon from the resonator for a single excitation of the TLS, and vice versa. There is also *longitudinal* coupling:

$$H_{\mathrm{int,z}} = \hbar g_z\sigma_z(a + a^{\dagger}) \tag{3.21}$$

which modulates the TLS frequency. As we are interested in on-resonance conditions ($\omega_{\mathrm{TLS}} \approx \omega_m$), we can omit this term as it is more dominant and related to dispersive coupling. Combining the individual Hamiltonians for the mechanical mode, the TLS , and the transverse interaction, the total Hamiltonian for the coupled system is:

$$H = \hbar\omega_m a^{\dagger}a + \hbar\omega_{\mathrm{TLS}}\sigma_{+}\sigma_{-} + \hbar g_x(\sigma_{+} + \sigma_{-})(a + a^{\dagger}). \tag{3.22}$$

This Hamiltonian is often simplified by moving into an interaction picture and applying the Rotating Wave Approximation (RWA). The RWA is valid when the coupling

strength is much smaller than the resonator and TLS frequencies ($g_x \ll \omega_m, \omega_{\mathrm{TLS}}$) and when the two are nearly resonant ($\omega_m \approx \omega_{\mathrm{TLS}}$). In this approximation, we neglect the rapidly oscillating terms that do not conserve energy on average. These are the "counter-rotating" terms, namely $\sigma_+ a^\dagger$ (simultaneous creation of a phonon and a TLS excitation) and $\sigma_- a$ (simultaneous annihilation of both).

Under the RWA, the transverse interaction term simplifies significantly, and the total Hamiltonian takes the form of the Jaynes-Cummings model, adapted for a quantum acoustic system:

$$H_{\mathrm{JC}} = \hbar\omega_m a^\dagger a + \hbar\omega_{\mathrm{TLS}}\sigma_+\sigma_- + \hbar g(\sigma_+ a + \sigma_- a^\dagger) \tag{3.23}$$

where g is the effective coupling rate (related to g_x). This Hamiltonian is the cornerstone of cavity quantum electrodynamics and its solid-state analogues. The first two terms describe the free evolution of the mechanical mode and the TLS, respectively. The third term is the crucial interaction term, describing the coherent exchange of a single quantum of energy between the two systems. It is this term that gives rise to the hybridization of the mechanical and TLS states, leading to the formation of new eigenstates, often called dressed states, and the characteristic vacuum Rabi splitting that is the hallmark of the strong coupling regime, which we will experimentally study in the following chapters.

In the experiments, the mechanical motion is excited by an applied electrical field through piezoelectric effect via the microwave signal input. For the quantitative formulation, we can consider that the resonator is coupled to the continuum of electromagnetic modes in the input transmission line. The interaction at the input port allows the resonator mode a to exchange energy with the field modes $b(\omega)$ in the line. The input field for a monochromatic drive at frequency ω_d can be written as:

$$\langle b_{\mathrm{in}}(t)\rangle = \alpha_{\mathrm{in}} e^{-i\omega_d t} \tag{3.24}$$

where α_{in} is the amplitude of the input field. The average photon flux of the input signal is $|\alpha_{\mathrm{in}}|^2$, which is proportional to the input power P via $P = \hbar\omega_d|\alpha_{\mathrm{in}}|^2$. This input field drives the resonator mode via the piezoelectric coupling. The effective Hamiltonian describing this drive process is given by:

$$H_{\text{drive}} = i\hbar\sqrt{\kappa_e}(a\langle b_{\text{in}}^{\dagger}(t)\rangle - a^{\dagger}\langle b_{\text{in}}(t)\rangle) \tag{3.25}$$

where κ_e is the coupling rate between the resonator and the transmission line, which quantifies the efficiency of energy conversion between the electrical and mechanical domains. Inserting the expression for the classical field amplitude, we obtain:

$$H_{\text{drive}} = i\hbar\sqrt{\kappa_e}(a\alpha_{\text{in}}^{*}e^{i\omega_d t} - a^{\dagger}\alpha_{\text{in}}e^{-i\omega_d t}). \tag{3.26}$$

By choosing the phase of the input drive such that α_{in} is real and positive, and factoring out common terms, we rearrange this to obtain the final form of the drive Hamiltonian:

$$H_{\text{drive}} = i\hbar\sqrt{\kappa_e}\alpha_{\text{in}}(ae^{i\omega_d t} - a^{\dagger}e^{-i\omega_d t}). \tag{3.27}$$

Together with the Jaynes-Cummings Hamiltonian H_{JC} (from Eq. 3.23), the full system is now defined by the full Hamiltonian:

$$H_{\text{full}}/\hbar = \omega_m a^{\dagger}a + \omega_{\text{TLS}}\sigma_{+}\sigma_{-} + \text{g}(a\sigma_{+} + a^{\dagger}\sigma_{-}) + i\sqrt{\kappa_e}\alpha_{\text{in}}(ae^{i\omega_d t} - a^{\dagger}e^{-i\omega_d t}). \tag{3.28}$$

We then move to the rotating frame at the drive frequency ω_d by the unitary transformation with:

$$U(t) = \exp\left[i\omega_d t(a^{\dagger}a + \sigma_{+}\sigma_{-})\right]. \tag{3.29}$$

The Hamiltonian in this new rotating frame, H', is given by the relation $H' = UH_{\text{full}}U^{\dagger} + i\hbar(\partial_t U)U^{\dagger}$. Applying this transformation makes the drive term time-independent and shifts the energies of the resonator and the TLS. The resulting Hamiltonian is:

$$H'/\hbar = (\omega_m - \omega_d)a^{\dagger}a + (\omega_{\text{TLS}} - \omega_d)\sigma_{+}\sigma_{-} + g(a\sigma_{+} + a^{\dagger}\sigma_{-}) + i\sqrt{\kappa_e}\alpha_{\text{in}}(a - a^{\dagger}). \tag{3.30}$$

We can simplify this expression by defining the detuning frequencies relative to the external drive $\Delta_m = \omega_m - \omega_d$ and $\Delta_{\text{TLS}} = \omega_{\text{TLS}} - \omega_d$, and the final time-independent Hamiltonian in the rotating frame can be written as:

$$\frac{H'}{\hbar} = \Delta_{\mathrm{m}} a^\dagger a + \Delta_{\mathrm{TLS}} \sigma_+ \sigma_- + \mathrm{g}\left(a\sigma_+ + a^\dagger \sigma_-\right) + i\sqrt{\kappa_e}\alpha_{\mathrm{in}}\left(a - a^\dagger\right). \tag{3.31}$$

This is the primary theoretical tool for describing our system's behavior under an external drive.

3.3.1 Equation of Motion

The Hamiltonian derived in Eq. 3.31 describes the coherent, internal dynamics of the coupled resonator-TLS system under an external drive. However, in any real experiment, the system is not perfectly isolated. It inevitably interacts with its surrounding environment, leading to irreversible processes like energy decay and decoherence. To provide a realistic description, we must treat our system as an open quantum system.

The evolution of the system's density matrix, ρ, is described by the Lindblad master equation [64]. It is important to note that this formalism relies on the Born-Markov approximation. This approximation assumes the coupling between the system and its environment (bath) is weak, so the state of the bath is not significantly altered [65, 66]. Moreover, it assumes that the bath has no memory of the system's past; its correlation time is much shorter than the characteristic timescales of the system's evolution. In this memoryless limit, the system's future evolution depends only on its present state. For most solid-state quantum devices at cryogenic temperatures, where the environmental fluctuations are very fast, these approximations are well-justified [67].

The general form of the Lindblad master equation is:

$$\dot{\rho} = -\frac{i}{\hbar}[H', \rho] + \sum_j \mathcal{D}[L_j]\rho \tag{3.32}$$

where the L_j are the Lindblad operators or jump operators, each describing a specific channel of interaction with the environment. The Lindblad superoperator, $\mathcal{D}[L]\rho$, is defined as:

$$\mathcal{D}[L]\rho \equiv L\rho L^\dagger - \frac{1}{2}(L^\dagger L\rho + \rho L^\dagger L). \tag{3.33}$$

Our system has two primary components that couple to the environment: the mechanical resonator and the TLS. The mechanical mode has an intrinsic energy loss

rate, κ_i and we can model this as coupling to a thermal bath at temperature T, which has an average phonon occupancy $n_{\text{th}} = (e^{\hbar\omega_m/k_BT} - 1)^{-1}$. This opens two dissipation channels: loss of a phonon to the environment, with operator $\sqrt{\kappa_i(n_{\text{th}}+1)}a$ and absorption of a thermal phonon, with operator $\sqrt{\kappa_i n_{\text{th}}}a^\dagger$. The resonator is also coupled to the external waveguide at a rate κ_e. This waveguide can function as a thermal bath at temperature T, therefore, it is a good practice to use total decay rate $\kappa = \kappa_i + \kappa_e$ instead of κ_i, but for our system the dominant term is found to be κ_i. These terms also can be considered as spontaneous emission and absorption of phonon due to thermal bath interactions.

Similarly, the TLS interacts with its environment at a rate γ_{TLS}. Assuming the same thermal bath, decay from $|e\rangle$ to $|g\rangle$, with operator $\sqrt{\gamma_{\text{TLS}}(n_{\text{th}}+1)}\sigma_-$ and thermal excitation from $|g\rangle$ to $|e\rangle$, with operator $\sqrt{\gamma_{\text{TLS}}n_{\text{th}}}\sigma_+$.

Combining the unitary evolution from H' with all four dissipative channels, we arrive at the complete master equation for the system's density matrix ρ.

$$\begin{aligned}\dot{\rho} = &-\frac{i}{\hbar}[H', \rho] + \kappa_i(n_{\text{th}}+1)\mathcal{D}[a]\rho + \kappa_i n_{\text{th}}\mathcal{D}[a^\dagger]\rho \\ &+ \gamma_{\text{TLS}}(n_{\text{th}}+1)\mathcal{D}[\sigma_-]\rho + \gamma_{\text{TLS}}n_{\text{th}}\mathcal{D}[\sigma_+]\rho \end{aligned} \tag{3.34}$$

This equation provides a complete description of the system's dynamics and is the foundation for simulating experimental observables. Solving the master equation for the density matrix ρ allows us to predict the outcome of any measurement on the system. One can typically solve for the steady-state density matrix ($\dot{\rho} = 0$) for continuous-wave experiments, or integrate the master equation over time for pulsed experiments. For our experiments, we are mostly interested in steady-state solution.

The average number of phonons in the resonator, $\langle n\rangle$, is the expectation value of the number operator $N = a^\dagger a$:

$$\langle n\rangle = \langle a^\dagger a\rangle = \text{Tr}(a^\dagger a\,\rho). \tag{3.35}$$

Plotting $\langle n\rangle$ versus drive frequency reveals the system's resonance spectrum. Coherences are captured by the off-diagonal elements of the density matrix. The complex amplitude of the resonator's motion is given by:

$$\langle a\rangle = \text{Tr}(a\rho) \tag{3.36}$$

which directly relates to the measurable output field of the device. We can use this to simulate the reflection coefficient of the coupled system. The complex value of $\langle a \rangle_{ss}$ quantifies the coherent state amplitude of the mechanical resonator mode. We can relate this internal mode amplitude to the external field which is actually measured. Using the input-output theory for one port system, the operator for the output field, a_{out}, is related to the input field, a_{in}, and the internal system operator, a, by the following relation [68]:

$$\alpha_{out} = \alpha_{in} + \sqrt{\kappa_e} a. \tag{3.37}$$

Note here that the sign of this can change depending on the choice of the drive term in the Hamiltonian. The reflection coefficient S_{11} is defined as the ratio of the complex amplitude of the output field to that of the input field. Using our notation where the input drive amplitude is α_{in}, we have:

$$S_{11}(\omega_d) = \frac{\alpha_{out}}{\alpha_{in}}. \tag{3.38}$$

By numerically solving for $\langle a \rangle_{ss}$ at each drive frequency ω_d across a desired range, we can fully reconstruct the reflection spectrum, $|S_{11}(\omega_d)|$, and its phase, which, as we will see, is directly compared to the data measured experimentally. But first, we shall explain the experimental methods used for these quantum measurements in the next chapter.

Chapter 4

EXPERIMENTAL METHODS AT CRYOGENIC TEMPERATURES

[Door meten tot weten] By measurement to knowledge...

H. K. Onnes

Experimental physics has been an essential instrument for physicists to test their hypotheses and explore the laws of nature. This is particularly true for low temperature physics, where the exploration of a new phenomena at cryogenic temperatures has consistently pushed the boundaries of our knowledge. At the core of these exploration lie a well-engineered experimental setups for the measurements to take place in an environment that is vastly different from our own. Therefore, it is important to review the cryogenic methods used in this work.

The foundations of low temperature physics were laid in 1880s, where there was a great effort on liquefying of common gasses. The most common method used for the liquefaction was to use pressure cycles and cool down the liquid until its boiling temperature. By using this method, oxygen (1877, 90 K), nitrogen (1883, 77 K), hydrogen (1898, 20 K), and lastly helium (1908, 4K) was liquefied (Fig. 4.1. The significant time gaps between these milestones underscore that advancing cryogenic methods was a slow process, demanding years of dedicated engineering and development. After the liquefaction of helium, entirely new experimental methods were necessary to achieve even lower temperatures. Decades later, the idea of using the enthalpy of mixing between isotopes of helium (^{3}He and ^{4}He) was proposed to break the 1 K barrier. After years of dedicated development, this was successfully demonstrated in 1964, marking the age of millikelvin (mK) temperatures. Today, this dilution method is the cornerstone of modern commercial refrigerators that systematically provide the ultra-low temperature environments required for a vast range of quantum physics experiments.

Each time a new record low temperature was reached, it emerged naturally for physicists to ask how the fundamental properties of matter would behave. Although low temperature physics and quantum mechanics initially grew as separate disciplines, this motivation turned the cryogenic laboratory into the ideal playground for

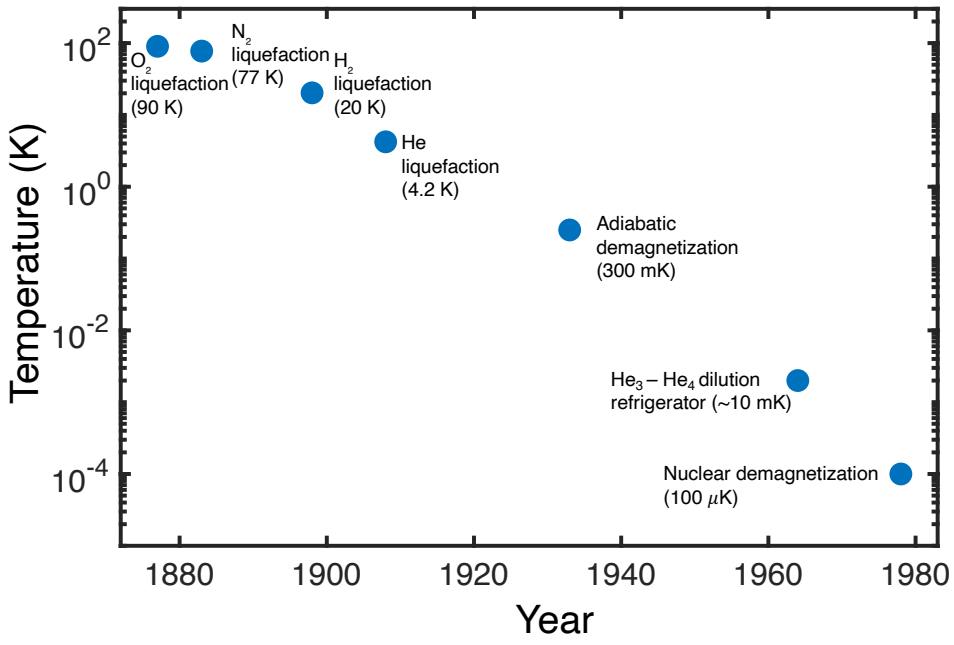

Figure 4.1: **Advancements in Low Temperature Physics.** Evolution of the record lowest temperatures achieved in cryogenic systems over the years with key milestones indicated. Lower temperatures have been reached through successive innovations in local cooling techniques; however, dilution refrigerators remain the most widely used cryogenic platform for condensed-matter physics experiments.

quantum exploration and enabled landmark discoveries like superconductivity. For our experiments with NEMS devices at low temperatures, our motivation is not so different as we are interested to know how the mechanical motion of solids behaves and interact with its environment in quantum regime. Exploring and studying this behavior demands systematic measurements and through analysis. And every good measurement starts with a good experimental setup.

From a practical perspective, building a cryogenic setup might be considered analogous to preparing a space mission; the entire experiment is assembled at room temperature and must be engineered to function after cooling. This requires careful consideration of different effects, including the thermal and electrical effects. Consequently, the material selection is critical to ensure proper thermalization, electrical conduction, or insulation as desired. The complexity is further exemplified by the wiring for microwave measurements, which demands specialized techniques and different considerations for actuation versus detection lines to manage heat loads and signal integrity. Given the brief introduction to experimental methods for low

temperature physics here, in the following sections of this chapter, we will cover the details of cryogenic experimental setups that was used in this work for the measurements of NEMS resonators. I had the fun and privilege of developing multiple cryogenic setups in the lab, and I wish the methods and knowledge gained from rigorous work, trial-error methods explained here will be useful to some in the field.

4.1 Cryogenic Coolers

There are two types of cryogenic setups used during this work; dilution refrigerator where most of the measurements in quantum regime performed (Chapter 5 and 6), and the hybrid platform consists of continuous flow cryostat and the mass spectrometry where NEMS-mass spectroscopy experiments (covered in Chapter 7) took place. The characterization of NEMS devices in quantum regime was done in a dilution refrigerator which can achieve millikelvin temperatures. In this section, the details of the both setups are discussed.

4.1.1 Continuous Flow Cryostat

The continuous flow cryostats are one of the earliest methods for cooling the solid-state materials to the temperatures of the boiling point of the cryogen. Here, we will mainly focus on the operation of Lakeshore Super Tran-300 continuous flow cycle cooler. The operating principle of the cryostat derives directly from the evaporative cooling. The liquid cryogen is stored in a vacuum insulated container, which is called dewar and no different than thermally insulated thermoses everybody use, and transffered to the surface where the heat exchange will take place. The flow of liquid cryogen can be achieved by taking advantage of the vapor pressure inside the dewar, which is similar to water jugs with a water pump dispenser on the top found in many homes. As the cryogen vapor pressure inside the dewar builds up, this forces the liquid through a transfer line that extends to the base of the dewar. The transfer line is usually a vacuum insulated metal bellow to preserve the cryogen in its liquid state throughout the transfer line. The flow of the cryogen is controlled by a manual needle control valve. Upon exiting the transfer line, the liquid cryogen contacts with the cold finger which is thermally conductive, usually made out of copper for high conductivity. As the liquid cryogen evaporates upon contact, it takes up some energy from the environment by

$$\dot{Q} = \dot{n}L \tag{4.1}$$

where $\dot{Q}$ is the cooling power (W), $\dot{n}$ is the mass flow rate (kg/s) across the liquid-vapor boundary, and L is the latent evaporation heat per particle (J/kg). Mass flow rate is proportional to the vapor pressure

$$\dot{n} \propto P_{\text{vap}}(T) \tag{4.2}$$

which has a $e^{-1/T}$ dependency. Therefore, the cooling power decreases rapidly as temperature decreases.

After this energy exchange gas leaves from the exhaust to the ambient pressure. Continuous replenishment of cryogen liquid can achieve evaporative cooling close to boiling point of the liquid. Final temperature is reached when there is a balance between the cooling power and heat sources such as heat from transfer line ($\dot{Q}_{\text{line}}$) and external heat from experiments ($\dot{Q}_{\text{ext}}$). At the steady state, cooling power and these heat sources will balance

$$\dot{Q}_{\text{cooling}} = \dot{Q}_{\text{line}} + \dot{Q}_{\text{ext}} \tag{4.3}$$

and the final temperature achieved will be dependent on these external factors [69]. Therefore, to reduce these heating factors, cryogenic systems require engineering for good isolation and efficient cooling. The schematic of such evaporative cooling operation is demonstrated in Fig.4.2.

Although the working principle is straightforward, handling cryogens require extra attention for safety and the continuity of the operation. The cryostat is made of all passive components, there are no active components that flows the liquid into the transfer lines, only the vapor pressure inside the dewar. Therefore, the challenge lies in maintaining the flow of the cryogen for longer hours. This control is adjusted only by the flow regulator valve. If higher flow rate is needed, an external pump can be connected from the exhaust port of the cryostat. The key to find the right balance is to observe the amount of vapor that comes out of the exhaust of the cryostat and the pressure inside the dewar. If the regulator valve is open more than it needs to be, then the flow in the beginning will be so high and you will observe liquid coming out from the exhaust. Eventually the dewar pressure will go down, and then the flow will be intermittent and not continuous. The cryogen liquid will be consumed in couple hours (depending on the size of the dewar) without making sufficient use of it. In an ideal setting, opening the valve only slightly would give sufficient cooling

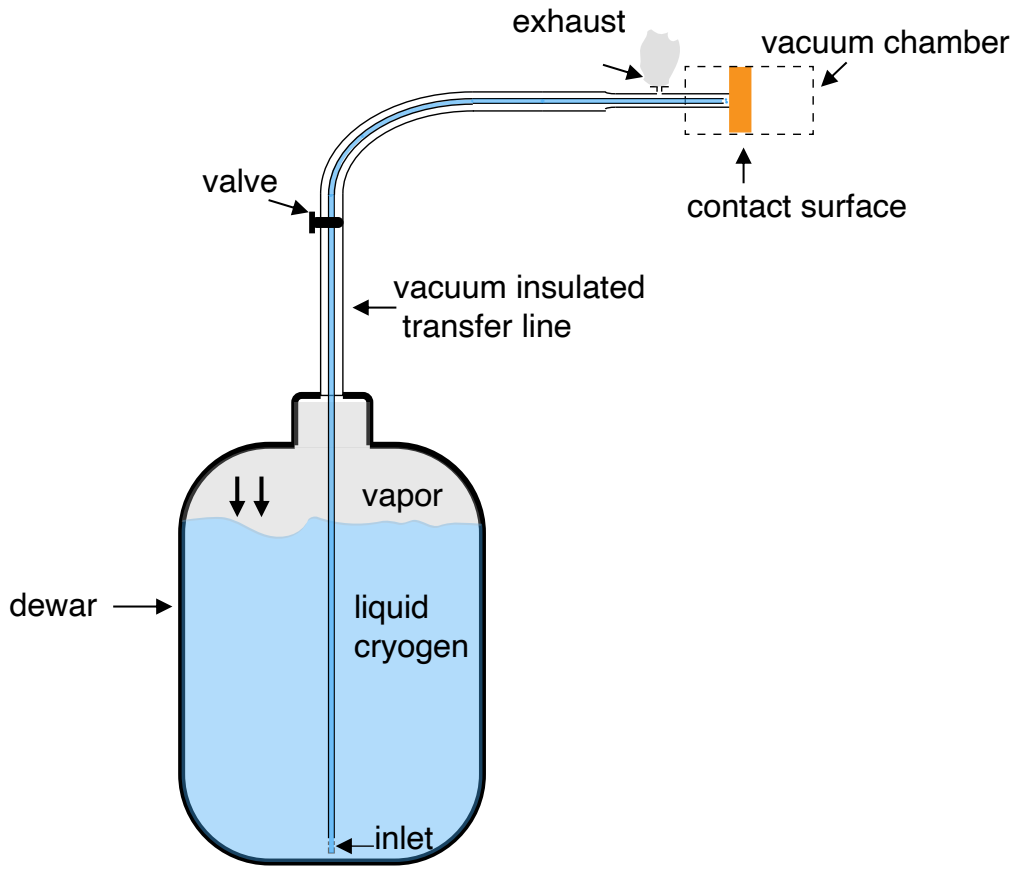

Figure 4.2: **Continuous Flow Cooling.** Schematic of a continuous flow cryostat. Vapor pressure in the dewar drives liquid cryogen through a vacuum-insulated transfer line to a heat exchanger which is the contact surface that is connected to the device under test inside the vacuum. The cryogen evaporates as it absorbs heat, cooling the surface, and the resulting gas is vented through the exhaust.

to maintain the minimum temperature reached, observed by stable dewar pressure and the stable exhaust in gas form. In the initial cooldown, valve can be opened up further to decrease the cooldown time as the evaporation will also be faster initially, however, if the liquid is coming from the exhaust that means the flow is so faster than it should be, thereby the cryogen is basically wasted.

During the start of the operation, the dewar must be filled close to full, to build up the vapor pressure faster, otherwise, the pressure necessary for the liquid flow will take a while to build up. Note that the fluctuations in the dewar pressure at the initial stage is expected and this behavior is caused by the shape of the dewar. The dewar's body has a cylindrical shape which turns into a cone shape and then a smaller diameter

cylinder until the mouth. Therefore, as the liquid level reduces inside the dewar, vapor volume increases nonlinearly until the liquid level reaches the cylindrical main body of the dewar. Once it reaches, then the pressure stability holds till the cryogen finishes. Therefore, it is worth to observe the initial temperature drop and the dewar pressure.

In the most recent years, this kind of cryostats have been mostly replaced by the closed cycle coolers. One of the main reasons is that in continuous flow cryostats, cryogen liquid is consumed and boil-off gas upon contact with the cold finger is usually exhausted to atmosphere. Therefore, cryogen liquid has to be resupplied for each cooldown and extended operation time at the low temperatures. This reduces the efficiency of the method, whereas in closed-cycle coolers there is no waste of cryogen. This becomes more critical subject especially when an expensive cryogen is used. Nevertheless, continuous flow cycle coolers retain some advantages, for example, they are more compact and do not have any active components, such as pumps, compressors, or pulse tubes. Therefore, there is less vibration which can be very important depending on the application. Moreover, these cooling method often reaches to the base temperature faster than closed cycles. In conclusion, continuous flow cryostats can be a good choice depending on application. In our system, we use such cooling in our NEMS mass sensing experimental setup.

The minimum temperature achieved in this type of cooling is determined by the boiling temperature of the cryogen at the ambient pressure. There are two commonly used cryogens for this kind of cooling; nitrogen and helium. Although the cryostat and the working principle remains the same, cooling procedures vary by the type of the cryogen which we will discuss in the following subsections.

4.1.1.1 Liquid Nitrogen Cooling

Liquid nitrogen (LN2) is the most convenient cryogen for an easy and cheap operation that can reach to temperatures around $\sim$ 77 K. The safety protocols should be followed carefully while transferring the LN2 to the dewar. While putting the tip of the transfer line into the dewar, one needs to make sure that the dewar leg is clean and warmed up from the previous cooldown. If the inlet holes at the tip of the dewar leg stays cold from the previous cooldown, the moisture in the air will freeze on the surface and block the intake valve with ice and there will be no cryogen intake. After carefully installing the dewar leg, the other end of the transfer line (cryostat leg) can be installed to the cryostat and then cooling can be started.

It is completely safe to leave the exhaust open to air while working with LN2. In time, ice will build up around the exhaust due to freezing of moisture in the air. It shouldn't build up so much if the flow is maintained at optimum level, but if it builds up so much it might lead to blocking of the exhaust line. Therefore, the best action is to connect the exhaust port to a pipe.

Once all of the LN2 in the dewar is consumed, one can quickly tap the dewar without warming up the whole system, but should follow the procedure to make sure no clog in the transfer line.

4.1.1.2 Liquid Helium Cooling

Liquid Helium (LHe) can reach to temperatures around $\sim$ 4 K, however, we could achieve slightly higher temperatures than that due to the heat loads in the system. Working with LHe is more challenging than handling LN2. One reason is that helium has lower latent heat so it will evaporate much faster than nitrogen gas, if handled wrong, pressures can increase drastically with the evaporation of LHe and cause damage to the cryostat. Also, LHe is much more expensive than LN2, and this is the reason why LHe is not popularly used in continuous flow coolers due to the waste nature of the method. Therefore, there must be some extra steps taken when operating with LHe.

Since LHe is expensive, one can choose to use LN2 for initial cooling and then switch to LHe. However, this method should be done very carefully. Before transfering the LHe through transfer leg, the line has to be under vacuum, because if the line has some trace gasses such as nitrogen, oxygen, LHe temperatures will freeze them to solid and clog the transfer line which will lead to rapid pressure build-up. Once this happens, there is no way back but to remove the transfer leg and warm it up until the line is clear again.

The safe operation of LHe is achieved with the implementation of rough pump from the exhaust port of the cryostat. The transfer line is vacuumed with initial pumping and then the regulator valve is opened to let LHe flow. During initial cooldown, the valve should be opened and closed with increasing periods of time for approximately 5 minutes to make sure the helium is able to flow without problem in the line. This can be observed with a pressure gauge connected to the outlet of the rough pump, pressure oscillations must be observed correlated with the valve opening and closing. After this initial gusting, pump could be turned off, otherwise

it will consume the LHe very rapidly, and LHe will keep flowing with its vapor pressure just like in LN2 case.

After the operation, LHe flow can be stopped with the valve, and it is recommended to start the pump again to prevent build-up solids inside the exhaust line and the transfer leg.

4.1.2 Dilution Refrigerator

The closed cycle coolers are the most effective way of cooling as the cryogen liquid is conserved during operation and the low temperatures can be attained continuously without interruption. The most famous example of this type of cooler is the dilution refrigerator which have gained popularity with the recent advancements in quantum research. The working principle of a dilution refrigerator is an fascinating subject that involves admirable engineering and knowledge of quantum physics. One can learn how to operate a dilution refrigerator just by following the steps in the manual, however, becoming a master of it requires understanding the fundamental principles that are used in the cooling process and gaining an intuition from it.

A dilution refrigerator has two main cooling mechanisms. The first is the two-staged pulse-tube (PT) cooler, which provides the initial cooling of the dilution unit from room temperature down to $\sim$ 4 K. The first stage of the PT is connected to 50 K plate and provides 50 W cooling power, whereas the second stage is at the base temperature of 4K with 1-2 W cooling power and can be connected to other plates thermally with heat switches. The working principle of the PT unit is very similar to any refrigeration cycle, which relies on cyclic compression and expansion of the working gas, which in this case is helium. With this method, stable temperature around 4 K in the unit is achieved. Moreover, the PT coolers are designed to have no moving parts at the cold head to prevent any mechanical vibrations that could interrupt the measurements.

Dilution unit use the heat of mixing of the two helium isotopes to obtain low temperatures and allow continuous operation at the base temperature. These isotopes are ^{4}He, which is the most common helium, and ^{3}He which is very expensive and acquired as a byproduct of a nuclear reaction or sparsely found in natural resources. ^{4}He obeys Boson statistics and has a superfluid transition temperature of 2.17 K, whereas missing a single neutron ^{3}He has a spin 1/2 and therefore obeys Fermi statistics and has a transition temperature much lower than ^{4}He. The transition temperature of the mixture depends on the concentration of ^{3}He and the phase

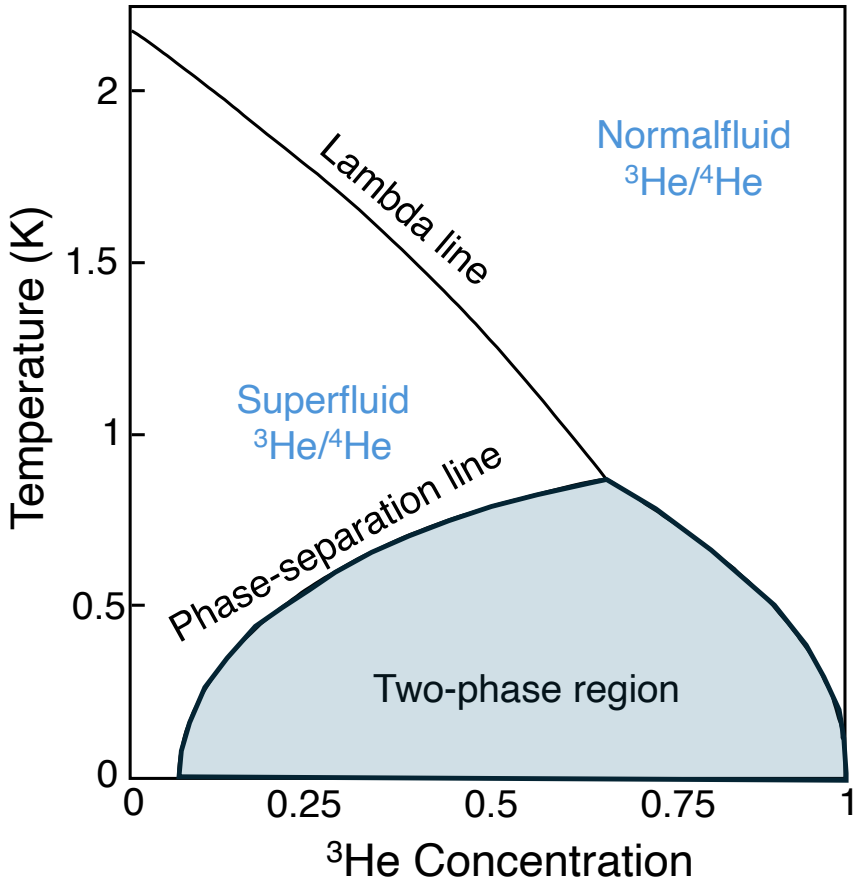

Figure 4.3: **Phase Diagram of Liquid ^{3}He-^{4}He Mixtures.** The diagram shows the normalfluid and superfluid phases of ^{3}He-^{4}He mixtures, separated by the lambda line. Below the tricritical point at ~0.87 K, the mixture enters a two-phase region where it separates into a ^{3}He-rich (concentrated) phase and a ^{3}He-dilute phase. This phase separation is the foundational principle of dilution refrigeration. The date plotted here is adapted from Pobell [69].

diagram of ^{3}He/^{4}He mixture is demonstrated in Fig.4.3. Below 0.87K, the ^{3}He/^{4}He mixture liquid eventually separates into two phases, one rich in ^{4}He and the other rich in ^{3}He which floats on top of the mixture. As temperature approaching the zero, the ^{3}He concentration has a finite value around 6.4% and this finite solubility is of utmost importance for 3He–4He dilution refrigeration technology.

Enthalpy, ΔH of this mixing is given by

$$\Delta H \propto \int \Delta C dT \tag{4.4}$$

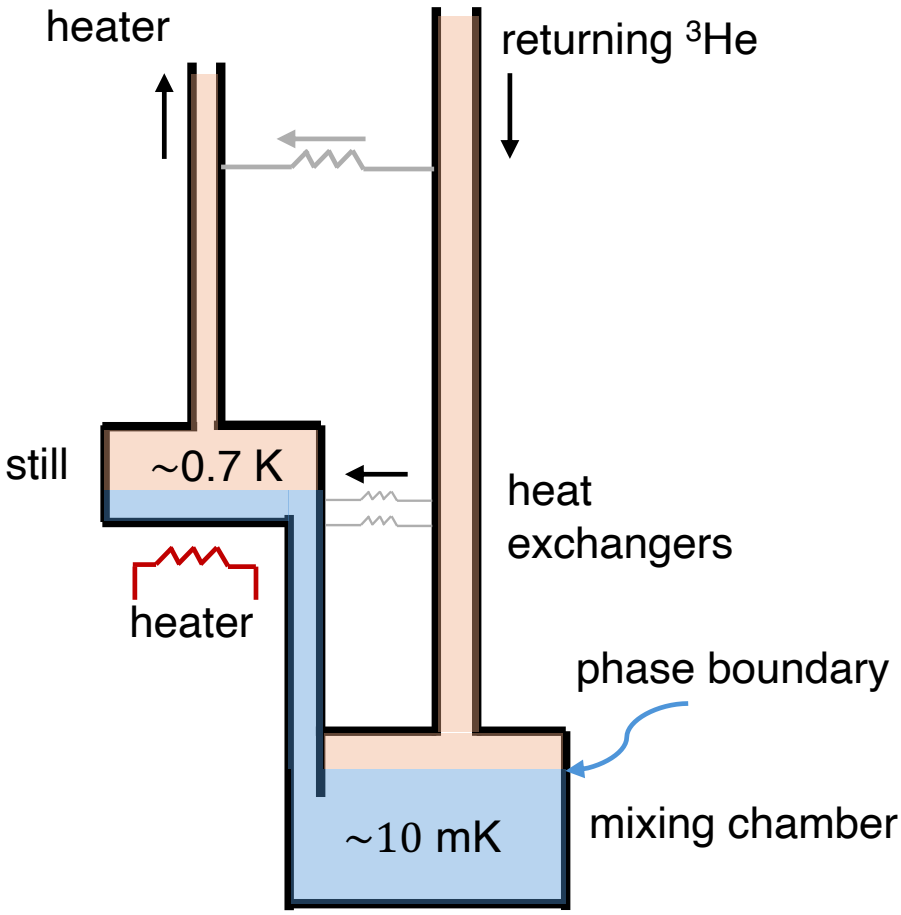

Figure 4.4: **Schematic of a Dilution Refrigerator Unit.** Concentrated ^{3}He enters from the top, is pre-cooled by a series of heat exchangers, and passes through a flow-limiting impedance before entering the mixing chamber. In the mixing chamber, the primary cooling occurs as ^{3}He atoms move from the concentrated phase to the dilute phase, reaching temperatures in the millikelvin range. The ^{3}He then travels to the still, which is heated to approximately 0.7 K to selectively evaporate the ^{3}He. This vapor is removed by a pump and re-circulated to sustain the cooling cycle.

and the specific heat capacity of concentrated and diluted ^{3}He are proportional to T at low temperatures, the cooling power follows

$$\dot{Q} \propto x\Delta H \propto T^2 \tag{4.5}$$

dependency. To take advantage of this cooling power, we need to take out ^{3}He from the diluted phase, which sits at the bottom of the mixture, and then ^{3}He from the concentrated phase will cross the phase boundary with a molar flow rate n_3, and will generate cooling power associated with

$$\dot{Q}_{\text{cooling}} = \dot{n_3}(H_{\text{d}}(T) - H_{\text{c}}(T)) \propto T^2. \tag{4.6}$$

According to this calculations, it is clear that we can achieve continuous cooling power if we can continuously remove the ^{3}He from diluted phase. The way to do that is not that different than distill processing in beer making. In a dilution refrigerator, mixing chamber, where the mixing process take place, is connected to a distiller, which is a 'still' stage and distills the ^{3}He from the diluted phase. A small heat applied to the still stage removes some of the ^{3}He which collected by the external pumping process. At the same time, returning ^{3}He during the circulation is cooled by the outgoing low temperature ^{3}He via well-engineered heat exchanger that reside in cold plate which is a stage between the mixing chamber and the still. Then, ^{3}He is added back to the mixing chamber so that ^{3}He can continuously cross the phase boundary resulting in cooling. This process is summarized in Fig.4.4.

Combination of PT cooling and the dilution unit define the working principle of modern dilution refrigerators. While PT provides the stable cold environment at 4K for dilution process to happen, mixing chamber and continuous circulation pumping can easily achieve $10mK$ base temperature. While the cooling power is rather well defined in PT cooling, dilution unit cooling power depends on the flow rate of ^{3}He which is a function of pressure and temperatures of different stages in the dilution unit. Therefore, pressures and temperatures are well monitored and maintained during the continuous operation. Example values for average cooling power achieved at each stage of our dilution unit are tabulated in Table 4.1.

Table 4.1: Average Cooling Powers at Each Stage of the Dilution Refrigerator.

Stage	Cooling Power
50 K	30 W
4 K	1.5 W
Still	40 mW
Cold Plate	200 μW
Mixing Chamber	20 μW

4.2 Instrumentation and Cabling

Building an experimental setup for cryogenic measurements demands a level of foresight and precision that exceeds what is required at room temperature. Solid materials undergo dramatic changes in their mechanical and electrical properties

when cooled to millikelvin temperatures. Therefore, an experimental physicist should be well-aware of these effects and take into account in material choices.

The experiments performed in this thesis mostly consist of microwave measurements performed in a dilution refrigerator and continuous flow cryostat. The setup was built from scratch inside the dilution refrigerator and the insights and methods gained from it is shared in this section. We will first cover the main effects including thermal expansion, thermal contact, and electrical conductance and later demonstrate the work done in our setup for the measurements.

4.2.1 Thermal Expansion

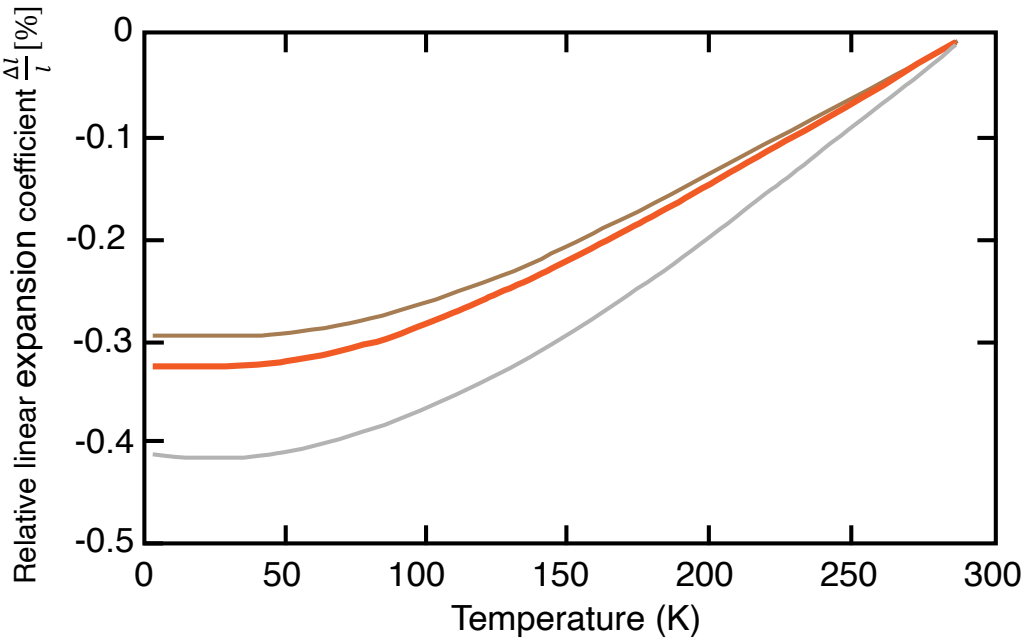

Figure 4.5: **Thermal Contraction of Materials.** Integrated linear thermal contraction, $\Delta l/l$, for several materials used in cryogenic construction, normalized to zero at room temperature. The plot highlights the significant contraction of metals relevant to this work, including aluminum (gray), stainless steel (brown), and copper alloys (orange), which must be accounted for in mechanical design. Figure adapted from Pobell [69].

Thermal expansion in solids is governed by the temperature-dependent shift in the average atomic spacing. The linear expansion coefficient given by

$$\alpha(T) = \frac{1}{l}\left[\frac{\partial l}{\partial T}\right]_p \tag{4.7}$$

reflects the fractional change in length, l, per Kelvin, and $\alpha(T)$ vanishes at $T = 0$. At low temperatures, the number of excitations and amplitudes of atomic vibrations around their equilibrium position r_0 decrease, whereas at higher temperatures these will increase. Variations in bonding strength and crystal structure yield distinct $\alpha(T)$ curves for each material which is demonstrated in Fig.4.5.

Selecting materials with compatible thermal expansion coefficients is critical when designing joints, surface mounts, and connectors. The safest approach is to use the same material wherever possible. For example, since most of the dilution-refrigerator plates are gold-plated oxygen-free-high-conductivity (OFHC) copper, we try to use copper attachments with copper or brass screws to minimize differential contraction during cooldown. 50K plate is made out of aluminum, therefore we use aluminum screws and attachments. Thermal contraction can also compromise electrical contacts: since microwave cables terminate in SMA connectors that screw into feedthrough flanges on each stage, a mismatch between the expansion coefficients of the cable's connector and the flange fasteners can cause the joint to loosen as the system cools. This can compromise the continuity of the ground connection, leading to significant signal noise and reflections in the electrical connections. Figure 4.6 demonstrates example mounting of custom-designed and manufactured feedthrough flanges to each temperature stages of the dilution refrigerator. Both the feedthroughs and the flange made out of gold plated OFHC copper.

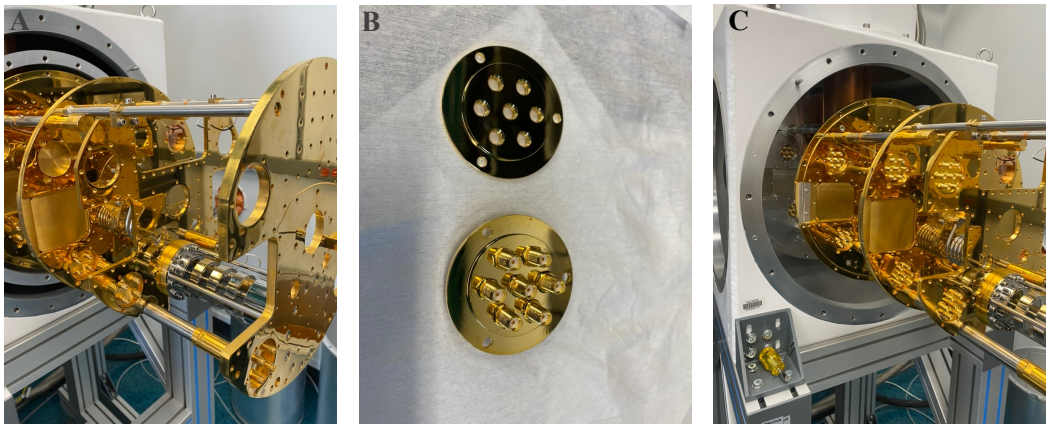

Figure 4.6: **Mounting Custom Feedthroughs.** **(A)** The gold-plated copper stages of the dilution refrigerator prior to installation. **(B)** The custom-designed components: a flange with SMA connectors and its corresponding mounting plate. Both are made from gold-plated OFHC copper to ensure matched thermal contraction. **(C)** The final assembly mounted on a refrigerator stage, ensuring robust electrical connections at millikelvin temperatures.

4.2.2 Thermal Conductance

Dilution refrigerators have different temperature stages that have different temperatures, although all the stages are physically connected to each other within the same frame. Thermalization, making or avoiding a thermal contact, is one of the most important aspects in building a setup in a dilution refrigerator.

Thermal conductivity is a material property related to heat transport capabilities of materials. Lattice vibrations (phonons) and electrons are the two main contributions to the heat transfer withing materials. Every material have different thermal conductivity coefficient, κ, and the rate of heat flow per unit area A is given by

$$\dot{Q}/A = -\kappa \nabla T. \tag{4.8}$$

Choosing materials with the appropriate κ enables tailoring heat flow at each interface. For mechanical support where you want to limit heat leaks—for example in dilution refrigerator between the OFHC copper plates—stainless steel links are ideal because their low κ blocks unwanted conduction. Where strong thermalization is needed (e.g., from a sample mount into the mixing chamber), using high κ OFHC copper: solid blocks, braids or thick straps that efficiently sink heat into the cold bath.

Beyond choosing materials by their conductivity, making a good contact is also important for good thermalization. For the experiments, device under test should be well-thermalized to the stage. To maximize real contact area and fill microscopic voids, a thin film of cryogenic vacuum grease—typically a hydrocarbon-based compound such as Apiezon N—can be applied between mating surfaces. When using OFHC copper, it is essential to remove any oxide layer just before assembly, since even a few nanometres of copper oxide can dramatically increase the thermal boundary resistance and impede heat flow into the bath.

Copper braids are another widely used method in cryogenic setups, as they are more flexible than the rigid counterparts and can be used as an extension to the stage. In our setup, we designed and fabricated multiple parts to ensure well-thermalization of our sample device and the microwave measurement components, such as amplifiers, circulators, etc. Figure 4.7 demonstrates some example mounts used in our setup.

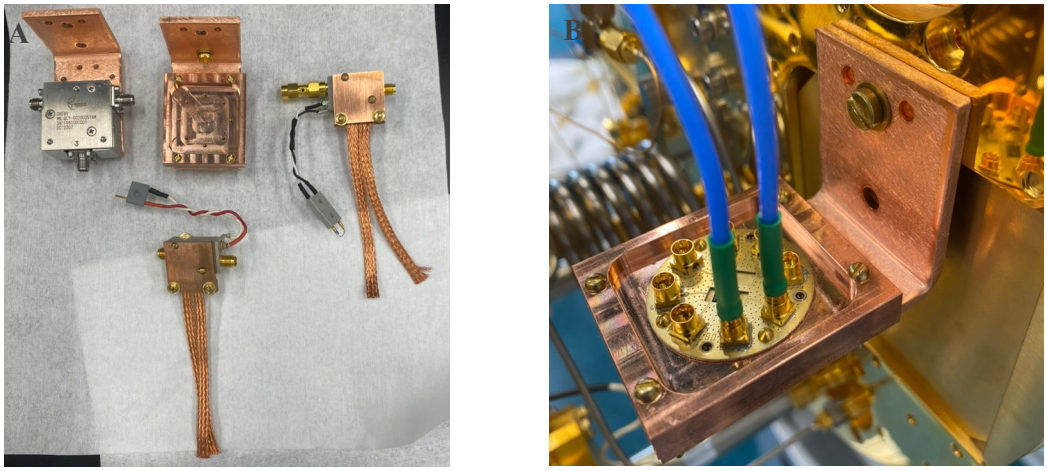

Figure 4.7: **Thermal Mounts for Cryogenic Components.** **(A)** A collection of custom-fabricated mounts made from OFHC copper. These include stages for microwave components like circulators and flexible thermal links made from copper braids. **(B)** An example of a thermal mount installed on a mixing stage, providing a robust thermal anchor for our NEMS device.

4.2.3 Wiring of a Dilution Refrigerator

Wiring inside the dilution refrigerator serves as a connection between the device under test, which is well-thermalized at the base temperature of the fridge, and the measurement hardware which is at room temperature. This connection must have well-electrical contact to capture the lowest amplitude signals while having a good thermal resistance not to carry heat from the room temperature. Therefore, we have to carefully consider the heat load from the cables that we put between the temperature stages. There are three main types of heat loads; passive load, active load, and radiative load.

Passive loads are the fixed loads which arise from steady-state thermal conduction, usually due to a thermal link to a warmer plate. Cables are one of the main sources of passive loads. A coaxial cable with a length l and cross-sectional areas A_c (central conductor), A_o (outer conductor) and A_d (dielectric), linking two baths at temperatures T_{cold} and T_{hot} will result in a heat flow

$$\dot{Q}_{\text{passive}} = \int_{T_{\text{cold}}}^{T_{\text{hot}}} [\kappa_c(T)A_c + \kappa_d(T)A_d + \kappa_o(T)A_o]dT. \tag{4.9}$$

Active loads originate from on-state dissipation, for example DC bias currents in an amplifier, or the dissipation through cables when power is applied [70]. In a microwave measurement, usually a microwave tone generated by the signal

generator or some hardware at room temperature has a certain input impedance, which is usually 50 ohm. The Johnson-Nyquist noise will have induced voltage fluctuations with a power spectral density given by [71]

$$S_V^{th}(T,\omega) = 2R\hbar\omega \frac{1}{\exp(\hbar\omega/k_BT) - 1} \tag{4.10}$$

where the last part of the equation is the photon occupation number given by Bose-Einstein distribution. At the classical limit ($\hbar\omega << k_BT$), this formulation converges to $S_V^{th}(T,\omega) = 2k_BTR$, or in terms of frequency well-known Johnson-Nyquist formulation $S_V^{th}(T,f) = 4k_BTR$. Therefore, when a coaxial cable is connected from room temperature to the base temperature of a cryostat, thermal photons propagate and carry this thermal noise to the milliKelvin stages. In order to match the thermal noise floor at the base temperature, this drive line has to be attenuated significantly. At our operating frequency 2 GHz (($\hbar\omega/k_B \approx 96$ mK), a 50 ohm resistor at 300 K would emit $[n(\omega) \approx \frac{k_BT}{\hbar\omega} \approx \frac{300\,\mathrm{K}}{0.096\,\mathrm{K}} \sim 3.1 \times 10^3]$ thermal photons. To suppress this down to well below one photon at the mixing-chamber plate, we therefore install three 20dB attenuators anchored at the 4 K, cold plate (100 mK), and mixing-chamber (10 mK) stages. Each attenuator absorbs thermal radiation from the stage above it (by a factor of 100 photons) and re-emits noise corresponding to its own physical temperature. This cascaded filtering ensures that the line's noise floor is thermalized to the millikelvin environment.

Lastly, radiative load is primarily due to the emissivity of materials. As each stage of a cryostat operates at a different temperature, blackbody radiation will be emitted from warmer surfaces and absorbed by colder ones. The net radiative heat transfer between two surfaces, often approximated for parallel plates or large enclosures, is given by the Stefan-Boltzmann Law and approximated for parallel plates with same area A as

$$\dot{Q}_{radiative} = \sigma A \left(\frac{1}{\frac{1}{\epsilon_H} + \frac{1}{\epsilon_C} - 1} \right) (T_H^4 - T_C^4) \tag{4.11}$$

where σ is the Stefan-Boltzman constant. This effect is well managed in modern dilution refrigerators by the use of radiation shields at the different temperature stages.

In our refrigerator wiring we employed four different coaxial cables, each with distinct dimensions and conductor materials: UT-034-B-B, featuring beryllium-

copper inner and outer conductors with a 0.034 inch overall diameter; UT-085-B-SS, with a beryllium-copper inner conductor, a stainless-steel outer conductor, and a 0.085 inch diameter; UT-085-SS-SS, with stainless-steel inner and outer conductors and a 0.085 inch diameter; and SC-219/50-NbTi-NbTi, which uses niobium-titanium inner and outer conductors and measures 0.0085 inch in diameter. In Fig. 4.8 we demonstrate the cross-section of these cables with the materials used and the thermal conductivity of these materials. Since the NbTi used as a superconducting cable, for temperatures well below the superconducting transition, electronic thermal conductivity goes as a power of the temperature and, is predicted to fall-off exponentially at very low temperatures [72]. Therefore, its thermal heat load is negligible compared to the other cables, and for this reason, it is not included in the heat load comparison. In Fig.4.9 we calculate the heat loads from each type of cables if they were to used to link different temperature stages of the dilution refrigerator. The analysis demonstrate that UT-B-SS cable has the highest heat load, due to its larger diameter and BeCu inner conductor which has a good thermal conductivity. UT-034-B-B has the lowest heat load due to its lower diameter, although it has BeCu inner and outer conductor. Since these values are for a single cable, using the cooling power values of the fridge from Table4.1, we can also calculate how many cables we can have.

In terms of the microwave signal attenuation, their loss per meter values are tabulated in Table 4.2.

Table 4.2: Microwave Attenuation at 2 GHz for Selected Coaxial Cables

Cable type	Attenuation (dB/m) at 2 GHz
UT-034-B-B	2.9
UT-085-B-SS	2.1
UT-085-SS-SS	4.2

For the drive line, which propagates the microwave signal from room temperature down to the mixing chamber, two primary considerations guide cable selection: minimizing heat load on the cryogenic stages and ensuring sufficient electrical attenuation to thermalize the incoming noise to the mixing chamber's noise floor. We utilize UT-085-B-SS cables from room temperature to the 4K stage. While these cables have a comparatively higher heat load than other options used in the cryostat, they are selected for this segment due to the long distances between stages (e.g., from 50K to 4K) where they provide robust mechanical support while delivering

acceptable microwave attenuation. From the 4K stage down to 10mK, we transition to UT-034-B-B cables. Their smaller diameter and optimized construction offer a significantly lower heat load (compared to B-SS cables) and the necessary level of microwave attenuation for the coldest stages. We do not use fully stainless steel (SS-SS) cables for microwave transmission due to their significantly higher electrical loss compared to copper-based or specialized cryogenic coaxial cables.

On the other hand, for the detection line, which carries the signal from the milliKelvin stages up to room temperature, the requirements differ. While minimizing heat load remains crucial, electrical attenuation must be strictly avoided to preserve the weak signals from the experiment. Therefore, we employ superconducting NbTi cables for the detection line from the mixing chamber (10mK) up to the 4K stage. These cables offer negligible electrical loss at cryogenic temperatures, losing their superconductivity around 10K. From the 4K stage up to room temperature, we again use UT-085-B-SS cables due to their balance of acceptable thermal performance and relatively low microwave attenuation for this section of the line.

4.2.3.1 Assembly of Coaxial Cables

After making a decision of which cable to use to link between which plates in the dilution refrigerator, we have assembled our own coaxial cables at desired lengths and variations. While RF cables can be ordered from commercial suppliers, custom lengths or non-standard connectors often incur long lead times and extra cost. Since there are few sources that walk through coaxial cable assembly step by step, this section covers our practical experience.

The assembly process consists of properly attaching to each ends of the cable with a proper RF connector, which is an SMA connector in our case. SMA connector consists of 2 main parts; center pin which connects to inner conductor, and an outer shell that bonds to the cable's shield. Two common connection methods are crimping and soldering. Crimping provides mechanical contact by compressing two metal parts together, and while relatively easy and straightforward with appropriate tools, it generally offers less reliable contact compared to soldering, particularly for superconducting cables [73]. For this reason, we opted for the soldering method for our cables.

The cable assembly process begins with a pre-ordered semi-rigid coaxial cable, which is cut to the desired length. To prepare the cable for connector attachment, the outer conductor is removed at a specific length to expose the inner conductor and

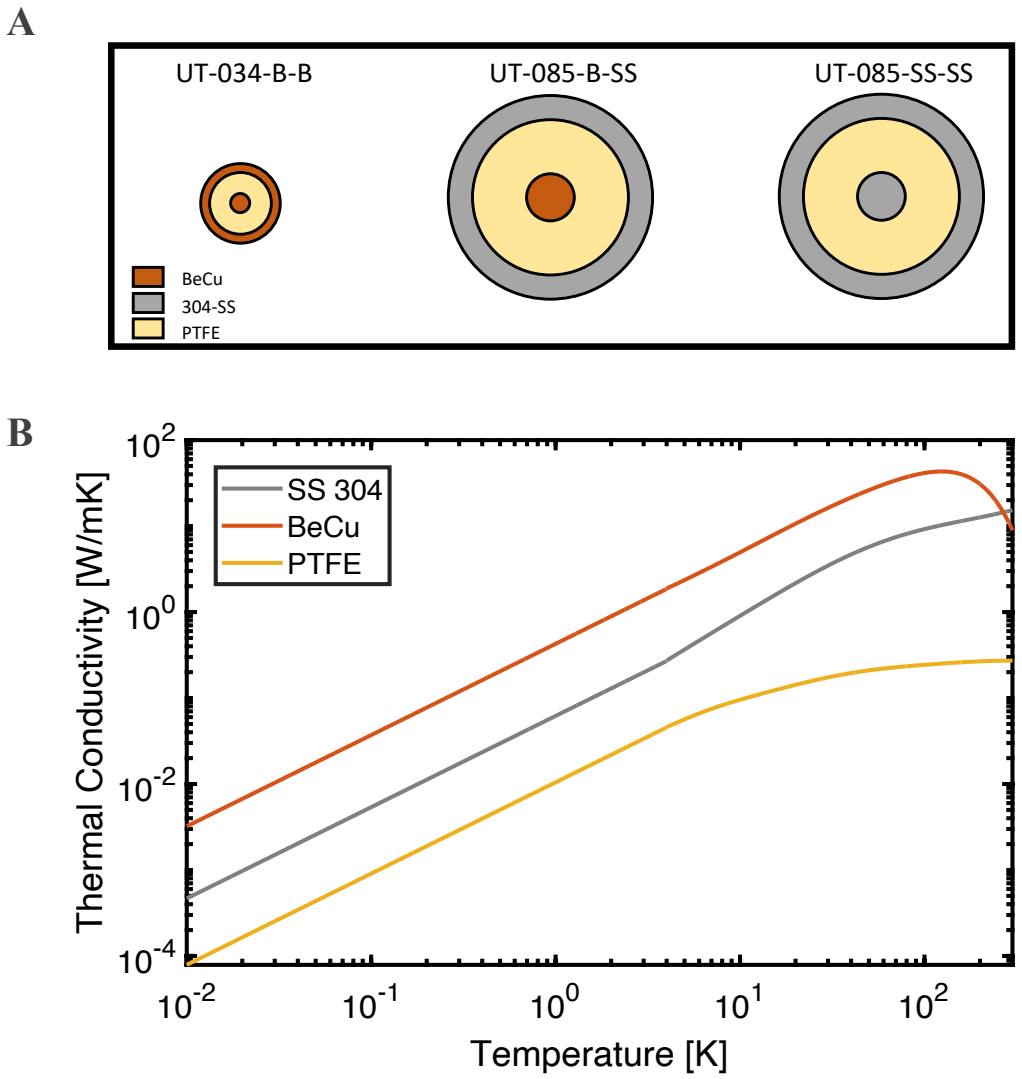

Figure 4.8: **RF Cable Choices. (A)** Cross-sectional diagrams of semi-rigid cables, showing the constituent materials: Beryllium Copper (BeCu), Stainless Steel (SS 304), and PTFE dielectric. **(B)** Thermal conductivity as a function of temperature for these materials.

provide a clean surface for soldering the center pin. The length of this exposed inner conductor is critical, as it is optimized for proper soldering and optimal electrical transmission. Deviations from these precise lengths can introduce significant signal loss, particularly at GHz frequencies.

For cables made with mechanically stiff materials, such as stainless steel, peeling the outer shell can be challenging, and specialized tools are rare due to stainless steel's inherent strength. An effective technique to achieve a clean cut and expose the inner conductor involves using a fine-grit file (Fig. 4.10A) to create a small defect on the

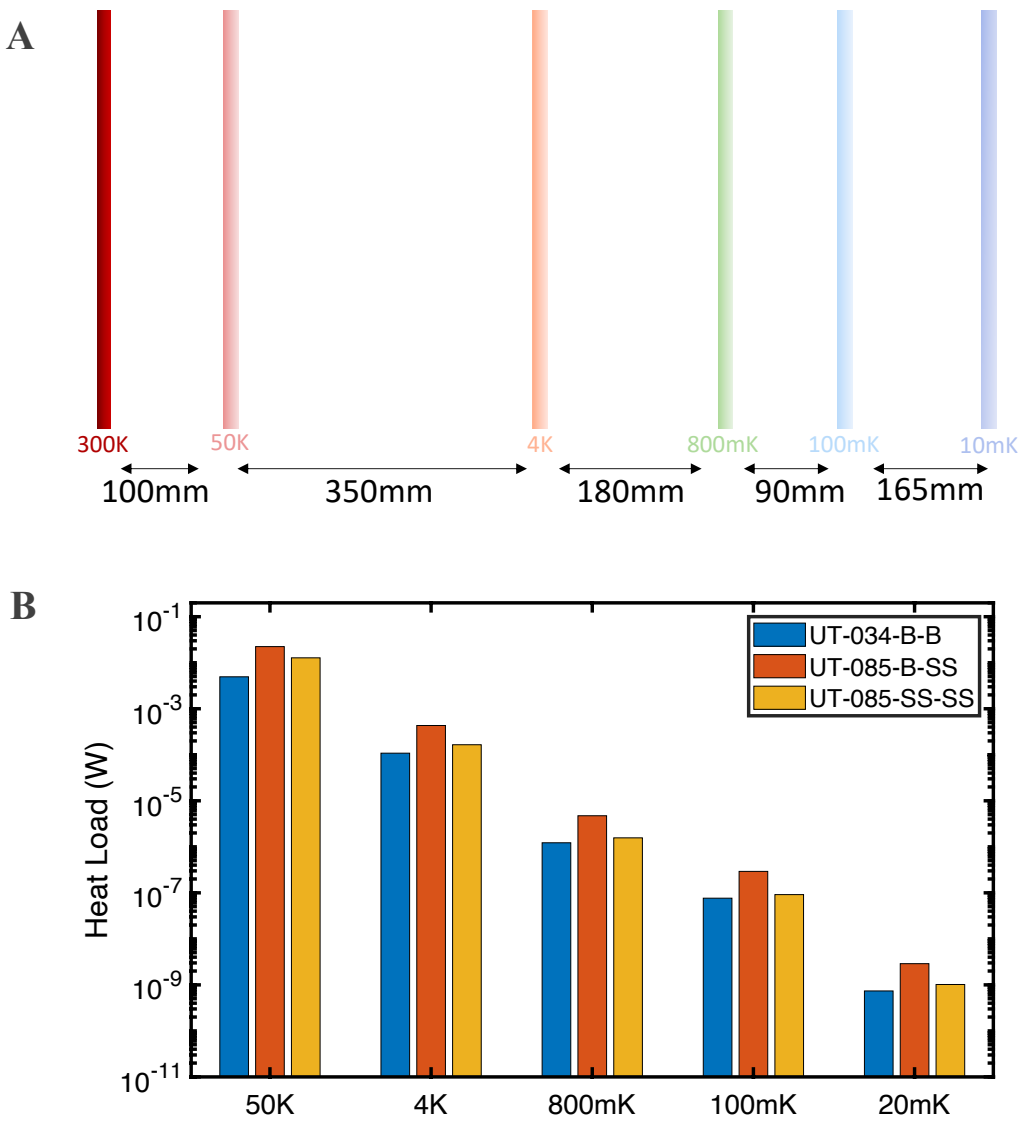

Figure 4.9: **Passive Heat Load from Cables.** **(A)** A schematic of the temperature stages and their physical separations within the cryostat, used as a model for the passive heat load calculation. **(B)** The calculated passive heat load delivered to each stage by three different types of semi-rigid coaxial cables.

outer surface(Fig. 4.10B), allowing the metal to be snapped cleanly(Fig. 4.10C). This method ensures a precise, circular cross-section, which is essential for optimal performance.

The next crucial step is soldering the center pin to the inner conductor of the cable, as demonstrated in Fig. 4.10D. This can be quite challenging due to the very small contact area. We found that pre-tinning the inner conductor is extremely helpful for

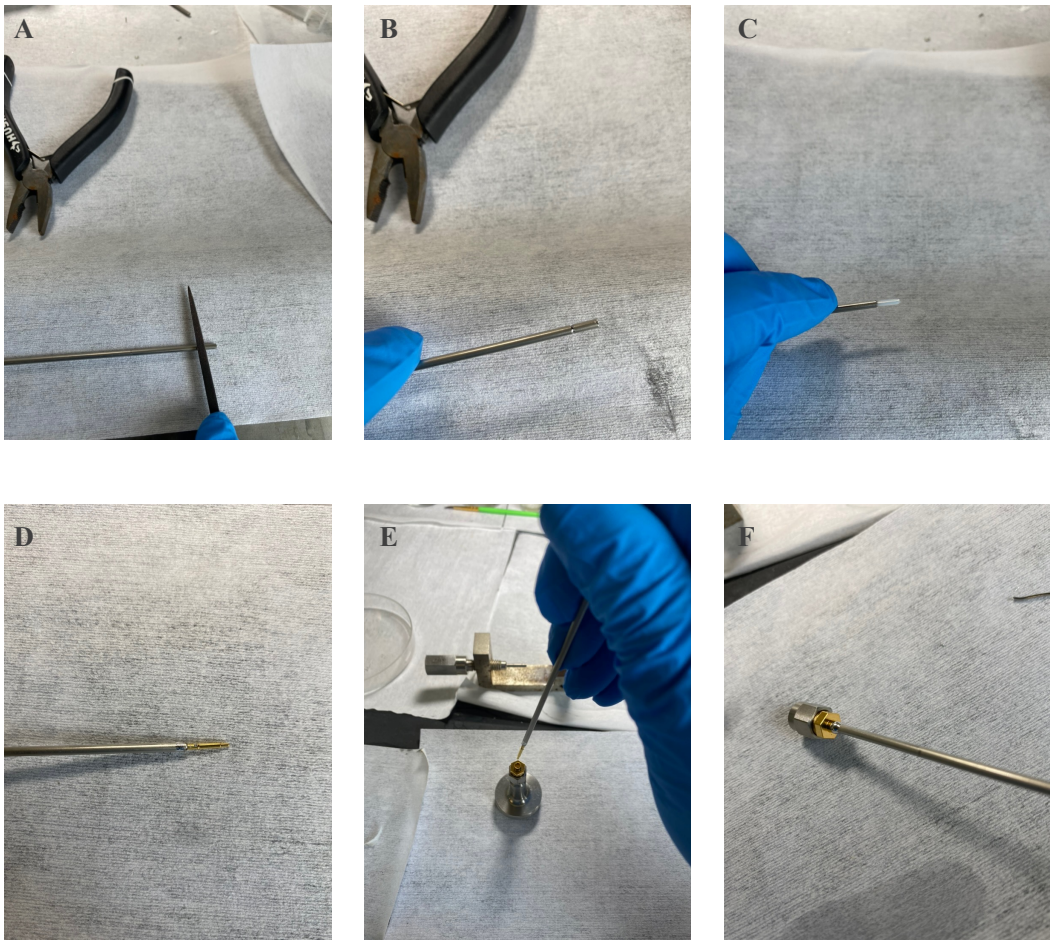

Figure 4.10: **Soldering Coaxial Cables.** **(A-C)** Preparing the cable end by scoring the outer conductor with a file before snapping it cleanly. **(D)** Soldering the center pin to the inner conductor. **(E)** Using an assembly kit to ensure proper alignment of the connector shell. **(F)** Soldering the outer shell to the cable's outer conductor to complete the connection.

achieving a strong, reliable solder joint. Center pin should be free from any excess solder as this can create changes in impedance of the transmission line. At this stage, it is very easy to accidentally make a connection between the inner and the outer shell, which can cause short circuits. Even a tiny amount of solder can create contact with high resistance and this should be avoided.

Once the center pin is securely soldered, the subsequent step involves connecting the SMA shell to the cable's outer conductor. Utilizing a passive SMA assembly kit (Fig. 4.10E) proves highly beneficial for aligning, holding, and precisely positioning the components. The primary challenge at this stage is accurately setting the insertion depth of the center pin within the SMA shell. To facilitate this, we

employed an SMA kit equipped with a stopper, ensuring the center pin is positioned at the optimum depth for proper electrical contact and impedance matching. At the final stage (Fig. 4.10F), the SMA outer shell is soldered to the cable's outer conductor. This process is repeated for the other end of the cable.

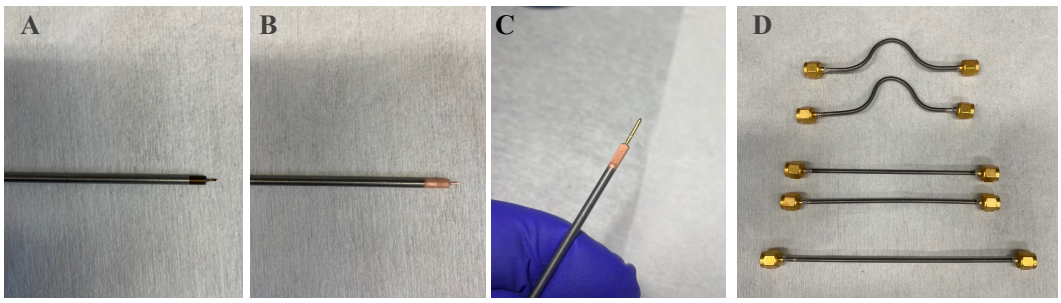

Figure 4.11: **NbTi Coaxial Cable.** **(A)** The NbTi inner conductor after being treated in a NaOH solution to form a dark oxide layer. **(B)** The same conductor after being electroplated with copper to create a solderable surface. **(C)** A close-up view of the soldered SMA center pin on the copper-plated tip. **(D)** A collection of completed NbTi cables with various lengths and thermal-relief bends.

Although this method works for stainless steel and berillium copper cables, NbTi is very hard to solder directly because have an extremely tough oxide layer that is impervious to even the most aggressive fluxes. Therefore, we followed the procedures described by [73], which uses electroplating copper to the surface of the NbTi and then soldering to the SMA connector. The steps followed for this assembly is summarized in Fig. 4.11. After making a clear cut and exposing the inner conductor, first electrolicitc cell (sodium hydroxide (NaOH) in deionized water) achieves a special oxide layer on the NbTi that will allow the copper to adhere to the titanium. This creates this dark oxide layer demonstrated in Fig. 4.11A. The second cell consists of an acidic copper plating solution made of 220 g/l of copper sulfate pentahydrate (CuSO4· 5H2O) with 40 ml/l of sulfuric acid (H2SO4) in deionized water achieves a thin layer of copper in Fig. 4.11B. Then following the same steps, we assembled many cables according to our needs Fig. 4.11D.

In addition to the coaxial cables, we also fabricated the DC wiring for our dilution refrigerator for DC bias applications. This wiring primarily consists of twisted pair (TWP) cables, which are made by twisting two small-diameter insulated conductive wires together. To ensure proper thermalization, the TWP cables are wrapped around a copper bobbin at each stage of the refrigerator. Due to their very small diameter, these cables are typically bundled, such as in configurations of 12 pairs,

and terminated with 24-pin Fischer connectors for integration. This wiring is designed for excellent electrical isolation, and the inclusion of a low-pass filter at the 4 K stage further reduces high-frequency noise. A significant challenge with these small-diameter wires is their fragility, making them prone to breakage and accidental short circuits during handling and installation.

Chapter 5

STRONG COUPLING OF MECHANICAL VIBRATIONS TO INDIVIDUAL TLS DEFECTS IN A NANOMECHANICAL RESONATOR

[1] M. Yuksel*, M. P. Maksymowych*, O. A. Hitchcock, F. M. Mayor, N. R. Lee, M. I. Dykman, A. H. Safavi-Naeini, and M. L. Roukes, "Intrinsic phononic dressed states in a nanomechanical system", arXiv preprint arXiv:2502.18587 (2025),

Nanoelectromechanical systems (NEMS) provide a platform for probing the quantum nature of mechanical motion in mesoscopic systems. When operated in the few-phonon regime, a NEMS resonator becomes a sensitive tool to study the phonon coherence, allowing direct investigation of energy distribution and interactions with its environment and the microscopic sources of decoherence. In this limit, material defects—ubiquitous in solid-state devices—play an important role. These intrinsic defects modeled as two-level systems (TLS) can exchange energy with the mechanical mode, and affect the dynamics of mechanical motion. While these interactions are typically studied as a collective source of noise and dissipation, they can be understood at the most fundamental level by achieving strong coupling between a single TLS and the mechanical mode. Such interactions have been extensively characterized in photonic and superconducting microwave resonators; however, a comparable level of understanding and experimental validation has been lacking in phononic devices. Therefore, it is crucial to elucidate how individual TLS defects interact with mechanical vibrations in NEMS, both to advance quantum-limited sensing and to shed light on fundamental dissipation mechanisms in solids.

Beyond its importance for the fundamental understanding of TLS defects in solids, this strong interaction holds great potential for achieving a long-sought goal in the field. The quantum nature of phononic devices manifests most profoundly when the device vibrations are nonlinear and, currently, achieving vibrational nonlinearity at the single-phonon level is an active area of pursuit in quantum information science. Despite much effort, however, this has remained elusive. In this chapter, we report the first observation of intrinsic mesoscopic vibrational dressed states [74]. The requisite nonlinearity results from strong resonant coupling between an eigenmode

of our NEMS resonator and a single, two-level system (TLS) that is intrinsic to the device material.

In this chapter, first we will explain how to control the TLS *in situ* by varying mechanical strain, tuning it in and out of resonance at will with the mechanical mode of our NEMS resonator. This method allows us to observe strong coupling of the mode with multiple intrinsic TLSs individually. In the second section, we observe that varying the resonant drive and/or temperature allows controlled ascent of the nonequidistant energy ladder and reveals the energy multiplets of the hybridized system. In the third section, we report fluctuations of the TLS on and off resonance with the mode induces switching between dressed and bare states; this elucidates the complex quantum nature of TLS-like defects in mesoscopic systems. These quintessential quantum effects emerge directly from the *intrinsic* material properties of mechanical systems—without need for complex, external quantum circuits. Our work provides long-sought insight into mesoscopic dynamics and offers a new direction to harness nanomechanics for quantum measurements.

5.1 Strong Coupling between NEMS Resonator and Individual Two-Level System

For this study, we employ lithium niobate (LN) NEMS resonators that are isolated from the environment by phononic crystals (PnC) [13, 23, 75] and cooled to millikelvin temperatures in a dilution refrigerator. The PnC structure achieves low decay rates of phonons and TLSs, while using LN allows us to effectively induce a static crystal strain via its piezoelectric properties. As we show, this enables tuning the TLS frequency with exquisite control. Long-lived phonons confined to sub-wavelength volumes combined with the TLS tunability enable several key findings. In this section, we measure mode splitting and reveal a double avoided-crossing pattern which, as we show, is a characteristic feature of strong resonant coupling of a NEMS mode to TLS defects. We report the first observation of the the strong coupling between the mechanical vibrations of a NEMS resonator and an individual TLS defect in a *purely* mechanical system. TLSs with different level spacings that are strongly coupled to the mode are also observed. Their energy spectra are highly stable, showing reproducibility across repeated thermal cycles (10 mK to $\sim$ 1 K), variations in input power, and DC bias sweeps. This allows us to reproducibly address individual TLSs by tuning them in and out of resonance with the mode. The details of this NEMS-TLS strong coupling model discussed in details.

5.1.1 Piezoelectric Phononic Crystal Defect Resonator

Our NEMS resonator is comprised of thin-film lithium niobate (LN, 250 nm) with aluminum (50 nm) electrodes deposited on top (Fig. 5.1A) [75]. The fabrication details of our phononic crystal (PnC) nanoelectromechanical systems (NEMS) resonators are explained in A.

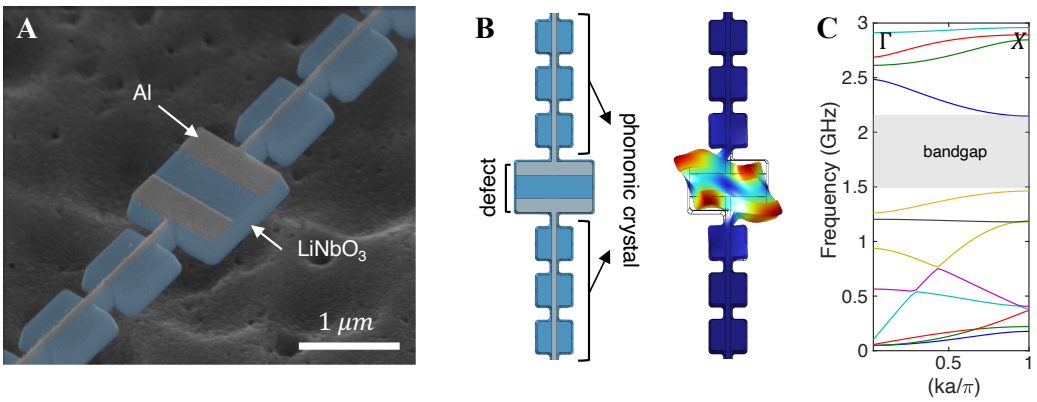

Figure 5.1: **Phononic Crystal Resonator.** **(A)** False colored scanning electron micrograph (SEM) of the lithium niobate ($LiNbO_3$) (blue) phononic crystal resonator with aluminum (gray) electrodes. **(B)** The device geometry consists of the repeating pattern of mirror cells, which forms the phononic crystal structure creating an acoustic bandgap (on the right). The mechanical resonator is a "defect" in the phononic crystal, and the shear mode is confined within the bandgap in **(C)**.

The resonator is embedded in a suspended periodic array of cells (Fig. 5.1B), which form a PnC that supports a complete acoustic bandgap (Fig. 5.1C). The resonator is a "defect" in the PnC. Its acoustic eigenmode that we study is within the bandgap and is thus well-localized, which leads to a long phonon lifetime. The aluminum electrodes facilitate piezoelectric transduction of mechanical vibrations [76]. Here, we experiment with a $\sim 1.1 \times 1.1 \mu m^2$ "defect" resonator with a fundamental shear mode frequency of $\omega_m/2\pi \approx 1.873$GHz.

We thermalize the sample chip to our dilution refrigerator at $T \approx 10$mK ($k_B T/\hbar \ll \{\omega_m, \omega_{\mathrm{TLS}}\}$) to achieve low phonon number in the mechanical mode. A simplified schematic of our microwave reflection measurement setup is shown in Fig. 5.2. A simple microwave reflection measurement (S_{11})is efficient to characterize our PnC NEMS resonators. A microwave signal that is at the resonance frequency of the mechanical mode and incident to the device through aluminum electrodes simply facilitate the excitations of mechanical vibrations via piezoelectric effect. The reflected wave from the electrode carries the information about the resonance,

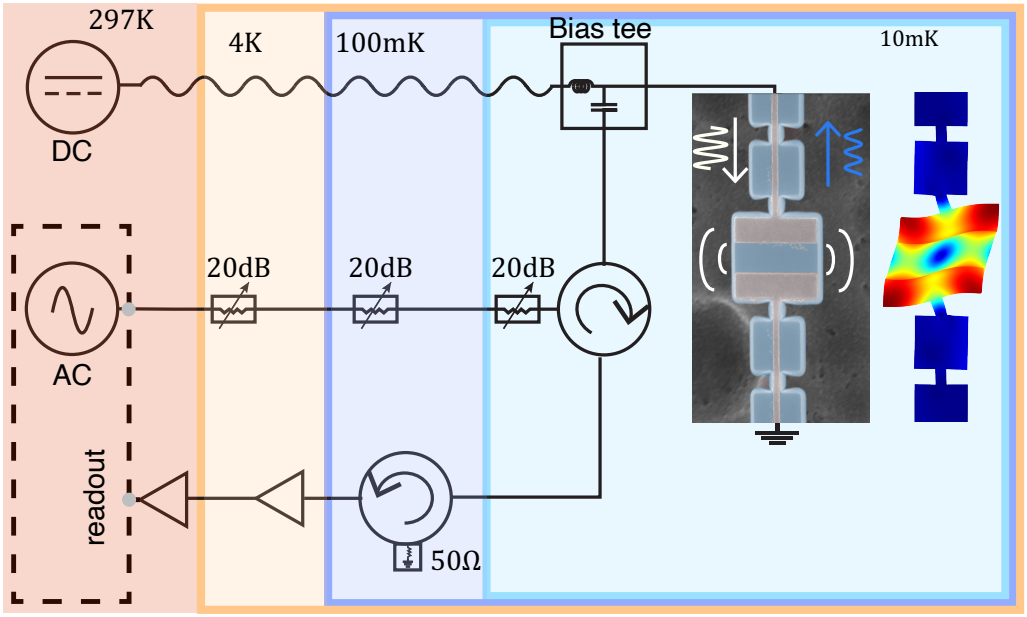

Figure 5.2: **Experimental Setup.** Schematic of the microwave reflection measurement S_{11} setup used to probe the fundamental shear mode localized at the center of the LN PnC resonator in our dilution refrigerator.

as its amplitude and phase respect to the incident wave has been altered due to this piezoelectric transduction.

This system can simply be modeled as a microwave waveguide coupled to the mechanical mode with a coupling rate κ_e. The model is sketched in Fig. 5.3A. In the linear regime, mechanical mode is modeled as a quantum harmonic oscillator with equal energy levels separated by ω_m. The microwave feedline contains a continuum of electromagnetic modes that constitute an external "bath." This bath couples to the mechanical mode via the piezoelectric properties of the lithium niobate (LN) device layer, resulting in an external energy exchange at a rate κ_e.

The Hamiltonian for this model can be written in rotating frame around the drive frequency ω_d as:

$$H/\hbar = \Delta_m a^\dagger a + i\sqrt{\kappa_e}\alpha_{in}(a - a^\dagger) \tag{5.1}$$

where $\Delta_m = \omega_m - \omega_d$. We can write the Heisenberg equation of motion $\dot{a} = \frac{i}{\hbar}[H, a] - \kappa/2$ where $\kappa = \kappa_i + \kappa_e$, which gives us the relation; $\dot{a} = -i(\Delta_m + \kappa/2)a - \sqrt{\kappa_e}\alpha_{in}$. At steady state ($\dot{a} = 0$), and with the boundary condition $\alpha_{out} = \alpha_{in} + \sqrt{\kappa_e}a$, we can write the expression for the reflection coefficient:

$$S_{11} = 1 - \frac{\kappa_e}{i\Delta_m + \kappa/2}. \tag{5.2}$$

In Fig.5.3B, we demonstrate an example S_{11} measurement. At on-resonance frequency, the amplitude of the reflected wave is significantly reduced as more of the incident microwave photons are translated into phonons via the piezoelectric effect. Therefore, by sweeping drive frequency ω_d across the mode frequency ω_m, the reflection coefficient S_{11} capture the steady-state response of the resonator, demonstrating a Lorentzian dip in $|S_{11}|$ at resonance.

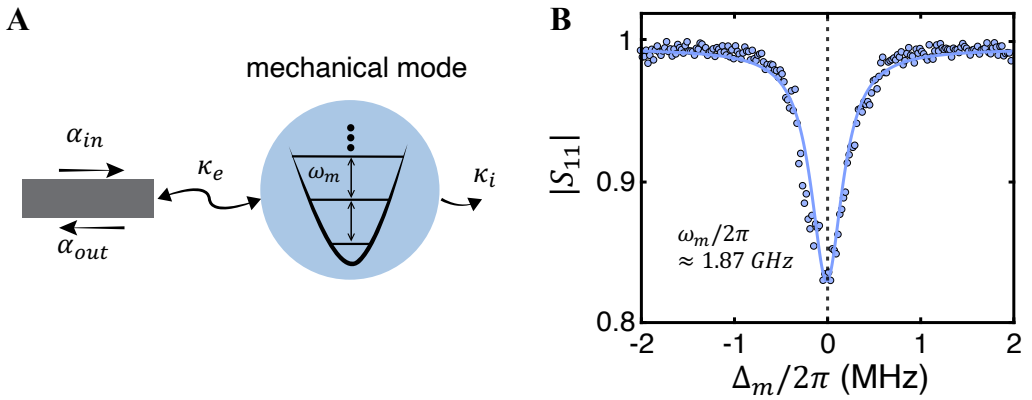

Figure 5.3: **Characterization of the NEMS. (A)** Schematic of the resonator model used to characterize the dynamics. **(B)** The reflection spectrum S_{11} of the mechanical mode.

5.1.2 Intrinsic TLS Defects

The structurally disordered aluminum-LN interface, amorphous LN leftover from fabrication, aluminum oxide, and the LN crystal itself can host numerous TLS defects, which could couple strongly to the local acoustic field. Previous studies on PnC resonators have shown anomalous frequency red-shifts and increased losses below $\sim$ 1 K [23, 40, 77], arising from coupling to a quasi-continuum of TLS defects with a broad distribution in frequency. In contrast, when an individual TLS is strongly coupled with the mechanical mode on-resonance, the system's dynamics become dominated by this localized interaction rather than ensemble effects. Therefore, we are interested in bringing strongly coupled TLSs onto resonance with the mechanical mode.

A conventional TLS model, which is explained in chapter 3, is sketched in Fig. 5.4 as a particle in a double-well potential with asymmetry energy ε and a tunneling

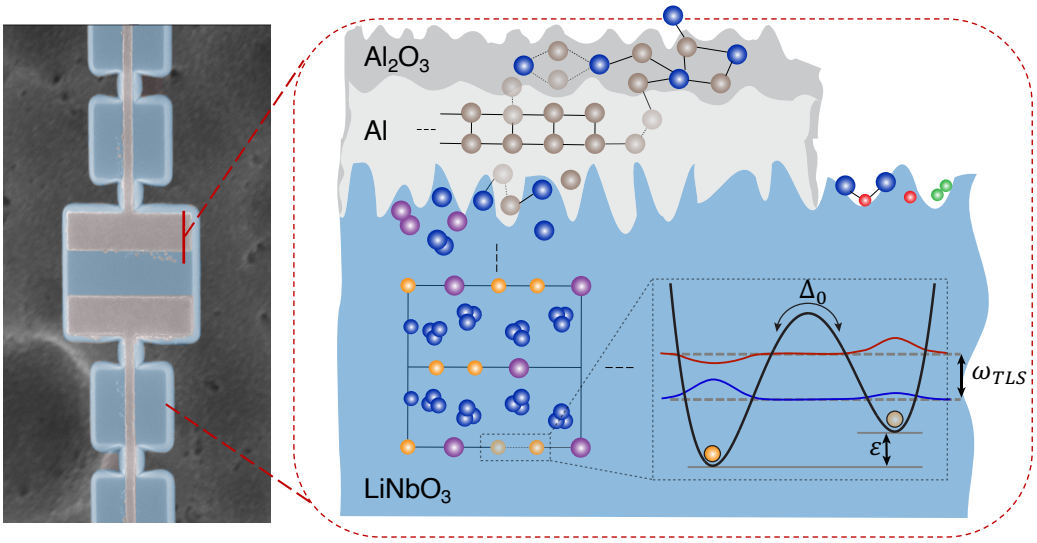

Figure 5.4: **Intrinsic TLS Defects in NEMS.** Toy model of the atomic structure in the cross section of the resonator. TLS can reside on the surface, within the bulk material or at the interfaces. Each TLS is modeled as a particle in a double-well potential with tunneling rate Δ_0 and asymmetry energy ε. The two energy states are separated by the TLS frequency ω_{TLS}.

energy Δ_0 between the two minima. The ground $|g\rangle$ and excited $|e\rangle$ eigenstates are superpositions of the intra-well states with an energy splitting $\hbar\omega_{\mathrm{TLS}} = \sqrt{\Delta_0^2 + \varepsilon^2}$, where ω_{TLS} is the TLS transition frequency.

To reconfigure the TLS bath and bring an individual TLS into resonance with the mechanical mode, we apply a DC bias voltage V_{dc} across the aluminum electrodes of our device (Fig. 5.5A). In the piezoelectric LN, this creates both a static electric field $\vec{E}$ and an associated strain field $\vec{S} = \hat{d}\vec{E}$, where $\hat{d}$ is the piezoelectric tensor [76]. While both of these coupled fields can perturb the local TLS environment, modifying the well asymmetry ε, the dominant coupling is considered to be via strain field as we don't observe TLS with direct electrical probing far from the mechanical resonance. To first order, the response to the applied bias is linear [8, 78], resulting in a DC-dependent TLS frequency of:

$$\omega_{\mathrm{TLS}} = \frac{1}{\hbar}\sqrt{\Delta_0^2 + \left(\varepsilon_0 + \frac{\partial\varepsilon}{\partial V_{\mathrm{dc}}}V_{\mathrm{dc}}\right)^2} \tag{5.3}$$

where $\partial\varepsilon/\partial V_{\mathrm{dc}}$ is the TLS sensitivity to DC voltage and ε_0 is the intrinsic asymmetry energy in the absence of the applied DC field. As seen from Fig. 5.5B and the

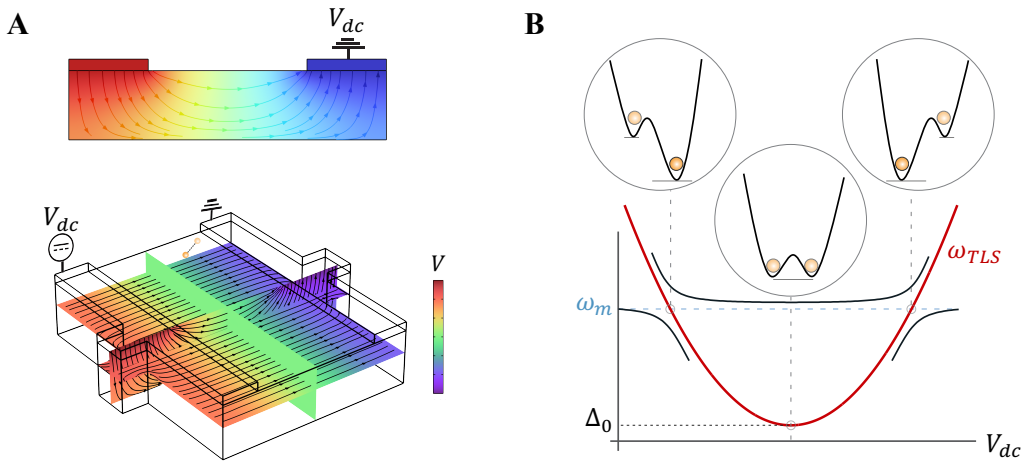

Figure 5.5: **Frequency Tuning of Intrinsic TLSs. (A)** Applied DC bias V_{dc} across the aluminum electrodes of the device creates an electric field within the bulk LN. **(B)** Tuning mechanism of the TLS frequency (ω_{TLS}) via the DC bias V_{dc}. The anticipated linear dependency of ε on the static electric field results in a hyperbolic dependency of TLS frequency on DC bias, $\omega_{\mathrm{TLS}}(V_{\mathrm{dc}})$. Consequently, two distinct V_{dc} values yield the same ω_{TLS}, corresponding to mirrored configurations of the double-well potential about Δ_0.

symmetry of Eq. 5.3, there are two distinct values of V_{dc} that result in the same ω_{TLS}. Similar methods have achieved in-situ control of TLS frequencies in superconducting qubits and microwave resonators, e.g., by bending the device chip [8, 79–81] or via DC-electric field biasing [82].

5.1.3 Observation of Strong Coupling

An oscillatory strain field resonant with ω_{TLS} can induce transitions from $|g\rangle \rightarrow |e\rangle$, allowing energy exchange at a coupling rate g. The resonant mechanical mode-TLS interaction is depicted in Fig. 5.6A, where γ_{TLS} is the TLS relaxation rate, and g is the coupling rate as addition to the mechanical mode parameters defined earlier. This coupled system is described by the JC Hamiltonian [83]. In the frame of a resonant drive at frequency ω_d, assuming the rotating wave approximation, this Hamiltonian reads (see chapter 3 for details):

$$\frac{H}{\hbar} = \Delta_{\mathrm{m}} a^{\dagger} a + \Delta_{\mathrm{TLS}} \sigma_{+} \sigma_{-} + \mathrm{g}(a\sigma_{+} + a^{\dagger}\sigma_{-}) + i\sqrt{\kappa_e}\alpha_{\mathrm{in}}(a - a^{\dagger}) \tag{5.4}$$

where $\Delta_m = \omega_m - \omega_d$ and $\Delta_{\mathrm{TLS}} = \omega_{\mathrm{TLS}} - \omega_d$ are the detunings, σ_{+} (σ_{-}) are the TLS raising (lowering) operators, a ($a^{\dagger}$) are the phonon annihilation (creation) operators,

and $\alpha_{\text{in}} \approx \sqrt{P/\hbar\omega_d}$ is the amplitude of the drive field related to the coherent drive power P incident to the mode.

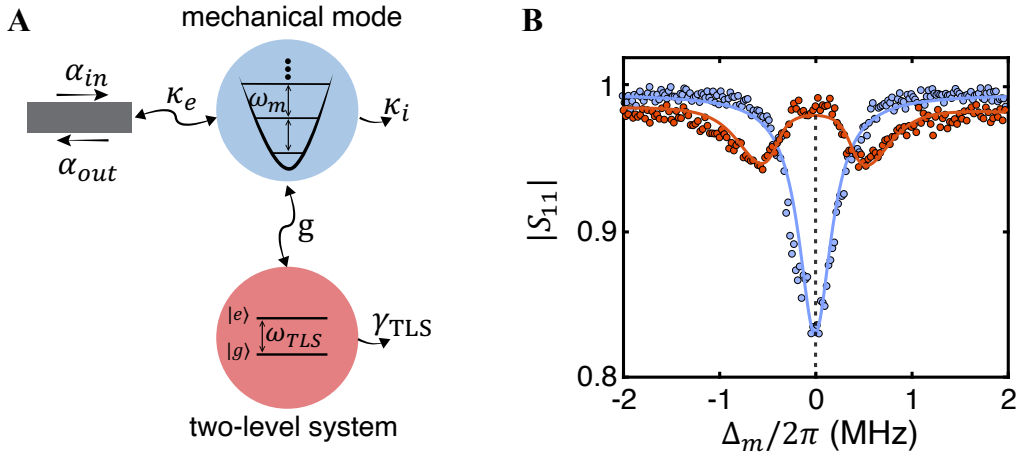

Figure 5.6: **Strong Coupling Regime.** **(A)** Schematic of the strong coupling model between the mechanical mode and an individual TLS defect, illustrating the interaction dynamics. **(B)** Example $|S_{11}|$ spectra for large (blue) and zero (orange) detuning between the NEMS and a strongly coupled TLS, characterized by a bare Lorentzian resonance and Rabi splitting, respectively.

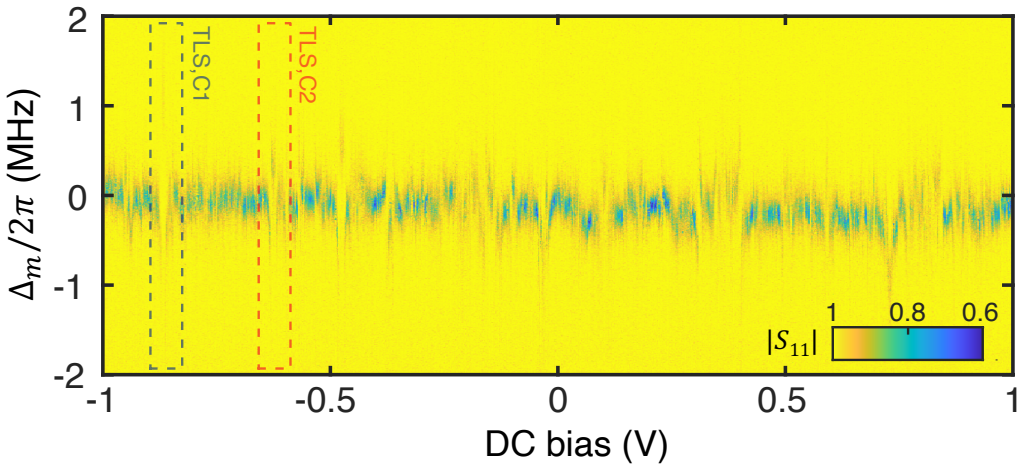

Figure 5.7: **TLS Spectroscopy.** The $|S_{11}|$ spectra near the mode frequency ($\Delta_m = \omega_m - \omega_d$) as a function of V_{dc} reveal many TLS crossings at different bias voltages.

To exploit the strong coupling regime between the mode and single TLS, we apply a coherent microwave drive at low power, $P = -150$ dBm, ensuring the intracavity phonon number is near zero. By sweeping ω_d across the mode frequency ω_m, we measure the reflection coefficient (S_{11}) and capture the steady-state response of the

resonator. When all strongly coupled TLSs are far detuned from the mode, we observe a linear resonator response as shown in Fig. 5.6B (blue). When a strongly coupled TLS is brought into resonance with the mechanical mode, the resonator frequency response splits into two—a phenomenon known as Rabi splitting and a hallmark demonstration of strong coupling (Fig. 5.6B, orange).

By performing this spectroscopic measurement while sweeping the DC bias, we can map the interactions between the resonator and the entire ensemble of tunable defects. In the resulting spectrum, plotted in Fig. 5.7, we display $|S_{11}|$ as a function of drive detuning (Δ_m) over a wide range of V_{dc}. We observe multiple avoided crossings at different V_{dc}, corresponding to different TLS defects tuned into resonance with the mechanical mode. Figure 5.8 presents measurements with finer DC steps over a narrower range, revealing clear evidence of two double avoided crossings each associated with an individual TLS, denoted TLS,C1 and TLS,C2 centered at ~ -865mV and ~ -623mV, with mode-TLS coupling rates $g/2\pi$ of 2.4MHz and 1.7MHz, respectively.

To quantitatively analyze our observations, we model the coupled TLS-phonon system including environmental interactions. An analytical expression for S_{11} can be derived in the low-temperature regime ($n_{\mathrm{th}} = 0$, where $n_{\mathrm{th}} = [\exp(\hbar\omega_m/k_BT)-1]^{-1}$) [81, 84]. A formulation for arbitrary n_{th} was given in [85]. Here, we provide numerical results equivalent to this formulation. The master equation for the density matrix ρ of the coupled TLS-mode system is [86]:

$$\begin{aligned}\dot{\rho} = &-\frac{i}{\hbar}[H,\rho] + (n_{\mathrm{th}}+1)\kappa_i D[a]\rho + n_{\mathrm{th}}\kappa_i D[a^\dagger]\rho \\ &+ \gamma_{\mathrm{TLS}}(n_{\mathrm{th}}+1)D[\sigma_-]\rho + \gamma_{\mathrm{TLS}}n_{\mathrm{th}}D[\sigma_+]\rho \end{aligned} \tag{5.5}$$

where $D[x]$ is the Lindblad damping superoperator defined by $D[x]\rho = x\rho x^\dagger - \frac{1}{2}\left(x^\dagger x\rho + \rho x^\dagger x\right)$ and H is given by Eq. 5.4. Simulating the full reflection spectra requires a two-step process. First, for a given V_{dc}, we calculate the corresponding TLS frequency ω_{TLS} with Eq. 5.3. Second, we use this specific TLS frequency in the H to solve the master equation for the steady-state density matrix ρ_{ss}, and then calculate the steady-state expectation value of the mode annihilation operator: $\langle a\rangle_{\mathrm{ss}} = \mathrm{Tr}(\rho_{\mathrm{ss}}a)$ via QuTiP [87]. For a device weakly and linearly coupled to a waveguide, the output field can be written as $\alpha_{\mathrm{out}} = \alpha_{\mathrm{in}} + \sqrt{\kappa_e}\langle a\rangle_{\mathrm{ss}}$ [68]. We then calculate the simulated reflection coefficient by $S_{11} = \frac{\alpha_{\mathrm{out}}}{\alpha_{\mathrm{in}}}$.

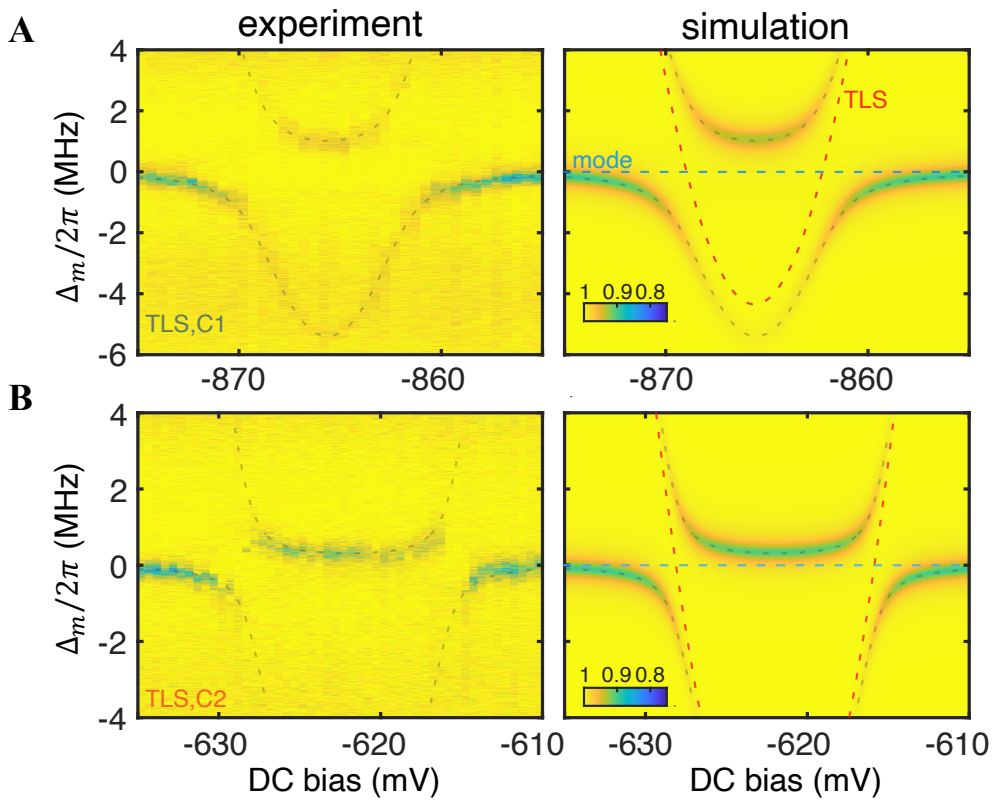

Figure 5.8: **TLS,C1 and TLS,C2.** Fine V_{dc} sweeps near the two double avoided crossings – labeled TLS,C1 **(A)** and TLS,C2 **(B)**– associated with coupling rates $g/2\pi$ of 2.4 and 1.7 MHz, respectively. Experimental results (left) are reproduced with simulations (right). Minima of the simulated $|S_{11}|$ are overlaid on the experimental data as black dashed lines. The TLS and the mechanical mode frequencies are indicated on the simulated spectra as red and blue dashed lines, respectively.

The simulated reflection spectra accurately reproduce the observed avoided crossings in Fig. 5.8, validating the presence of strong coupling. In particular, the measurement featuring TLS,C1 clearly demonstrates the hyperbolic shape of the TLS trajectory ($\omega_{\mathrm{TLS,C1}}(V_{\mathrm{dc}})$), which aligns with the theoretical model in Eq. 5.3 (Fig. 5.5B). This corroborates the linear dependence of ε on V_{dc} and the double-well potential model for a TLS coupled to a mechanical mode. The decay rates of the mode and TLSs are determined from the best-fit estimates of the spectra, with values of $\kappa_i/2\pi \approx 400$ kHz and $\gamma_{\mathrm{TLS}}/2\pi \approx 200$ kHz for TLS,C1. We measured strong coupling to individual TLSs in multiple LN resonators of varying dimensions and using different experimental setups located at both Caltech and Stanford. This highlights the robustness of our device architecture for studying and exploiting strong phonon-TLS interactions for quantum experiments.

5.2 Intrinsic Phononic Dressed States

While strong coupling to an individual TLS defect is evident, the quantum nature of these defects described by the JC model has not been fully established. In this section, we study the response of the strongly coupled TLS-NEMS system at higher excitation numbers. Under strong coupling, such excitations occupy dressed states rather than simple bare states. In the on-resonance case ($\omega_m = \omega_{\mathrm{TLS}}$), each pair of dressed states in level n (for $n \geq 1$) is formed by the symmetric $|n+\rangle \equiv (|n, g\rangle + |n-1, e\rangle)/\sqrt{2}$ and antisymmetric $|n-\rangle \equiv (|n, g\rangle - |n-1, e\rangle)/\sqrt{2}$ combinations, where n enumerates the vibrational quanta of the mode. In a more general case ($\omega_m \neq \omega_{\mathrm{TLS}}$), the dressed state energies are $\hbar[\omega_m n + \frac{1}{2}\delta \pm (\mathrm{g}^2 n + \delta^2/4)^{1/2}]$, where $\delta = \omega_{\mathrm{TLS}} - \omega_m$ [85]. The frequency splitting between dressed states scales as $2\sqrt{n}\mathrm{g}$ (Fig. 5.9), a characteristic of the JC model in the strong coupling regime. Theoretical details of this nonlinear energy scaling is discussed in details in Chapter 3.

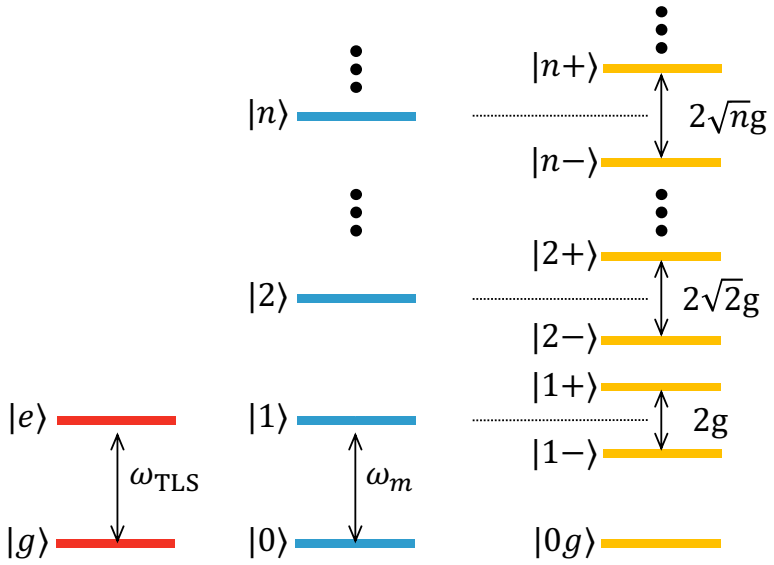

Figure 5.9: **Jaynes-Cummings Ladder.** Jaynes-Cummings energy levels for the on-resonance case ($\omega_m = \omega_{\mathrm{TLS}}$) of the strongly coupled TLS-mechanical mode system.

These dressed states are well-known in quantum optics [88], and have been explored using microwave superconducting qubits [89–91]. In the previous section, we have demonstrated Rabi splitting at $n = 1$, corresponding to the $|0g\rangle \rightarrow |1-\rangle$ and $|0g\rangle \rightarrow |1+\rangle$ transitions. Now, in our phononic TLS-NEMS platform, we provide direct evidence of the Rabi splitting for the transitions between the first and second

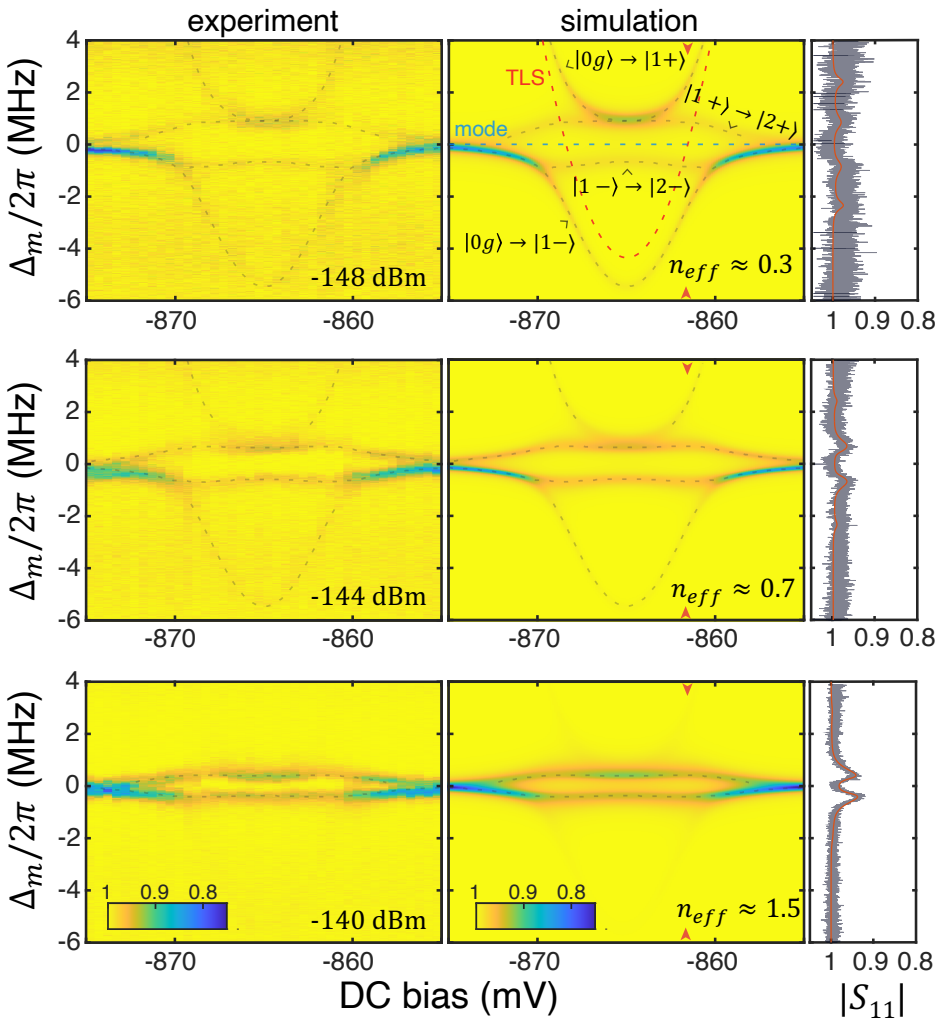

Figure 5.10: **Intrinsic Phononic Dressed States.** Experimental and simulated spectra of $|S_{11}|$ for TLS,C1 at three different input powers at the base temperature (10 mK). The additional fine structures appearing in the spectrum corresponds to the higher order transitions, revealing the TLS induced nonlinearity. Dashed lines on the experimental spectra denote minima extracted from the simulated $|S_{11}|$. On the far right, $|S_{11}|$ data are shown for detunings near resonance ($\omega_m \approx \omega_{TLS}$)—highlighted by red arrows in the simulated spectra—and the simulated response (orange) is overlaid on the experimental data (gray). As the incident microwave power increases (top to bottom), the response transitions from characteristic *avoided crossing* to an *eye-like* crossing.

excited multiplets of the dressed states. We also show that, as the excitation number increases, the response changes to the expected classical behavior [92, 93].

Our studies of the excited dressed states are twofold: we 1) vary the input drive power P at the base temperature (10 mK), and 2) controllably sweep the temperature at a

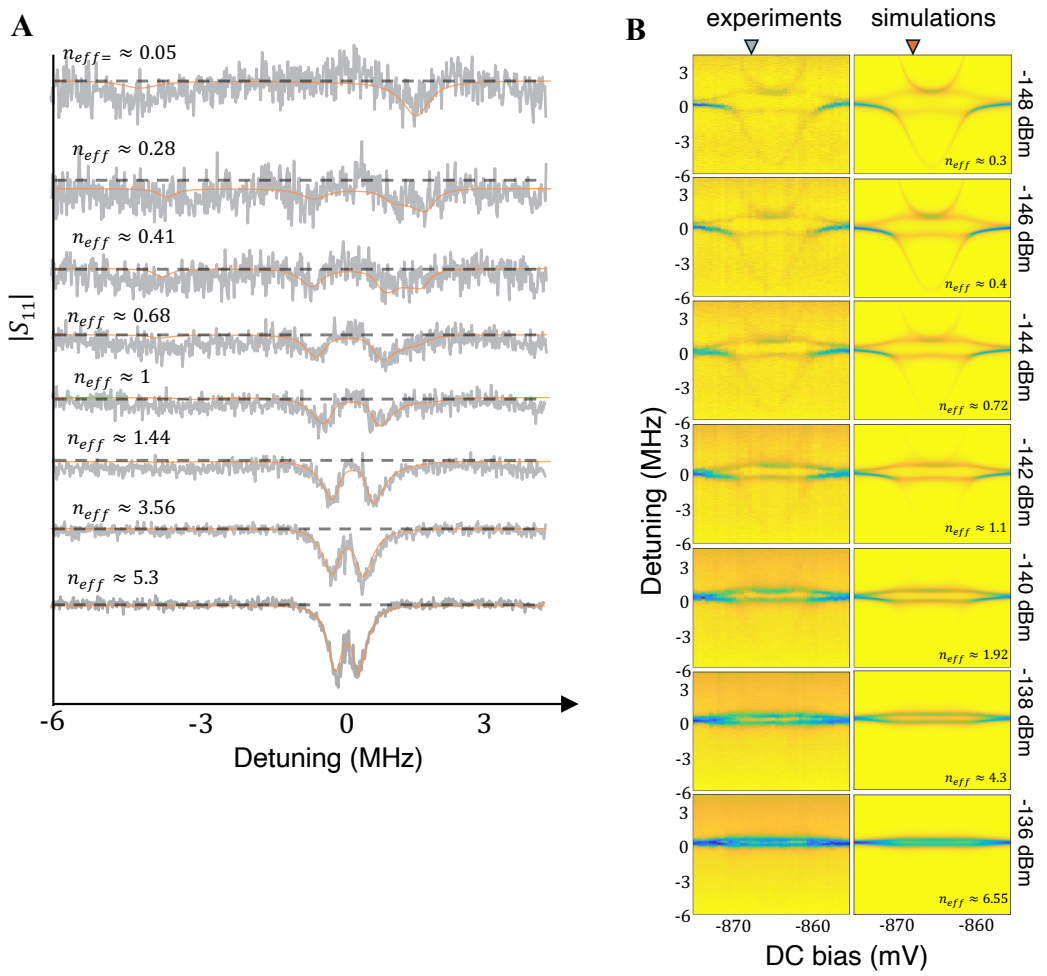

Figure 5.11: **Intrinsic Phononic Dressed States Additional Data.** Experimental and simulated spectra of $|S_{11}|$ for TLS,C1 for increasing input powers at the base temperature (10 mK). **(A)** Line cuts of the reflection spectrum taken at the TLS resonance point. Input drive power increases from top to bottom. While the first trace at top belongs to avoided crossing in Fig. 5.8A, the rest is from **(B)**. **(B)** Full experimental (left column) and simulated (right column) spectra versus DC bias and frequency detuning. The plots show the evolution of the TLS crossings at higher powers, which is accurately captured by our numerical simulations.

fixed P. At each power and temperature, we repeat the TLS crossing measurements, then model the results using simulations with Eq. 5.3 and Eq. 5.5, as we did earlier.

Figure 5.10 illustrates how the spectral features of the TLS,C1 crossing evolve at three different powers. At $P = -148$ dBm, in addition to a doublet response at the avoided crossings, the appearance of quadruplets of lines is a hallmark of higher energy transitions in JC ladder ($n > 1$). New frequencies in the spectrum correspond

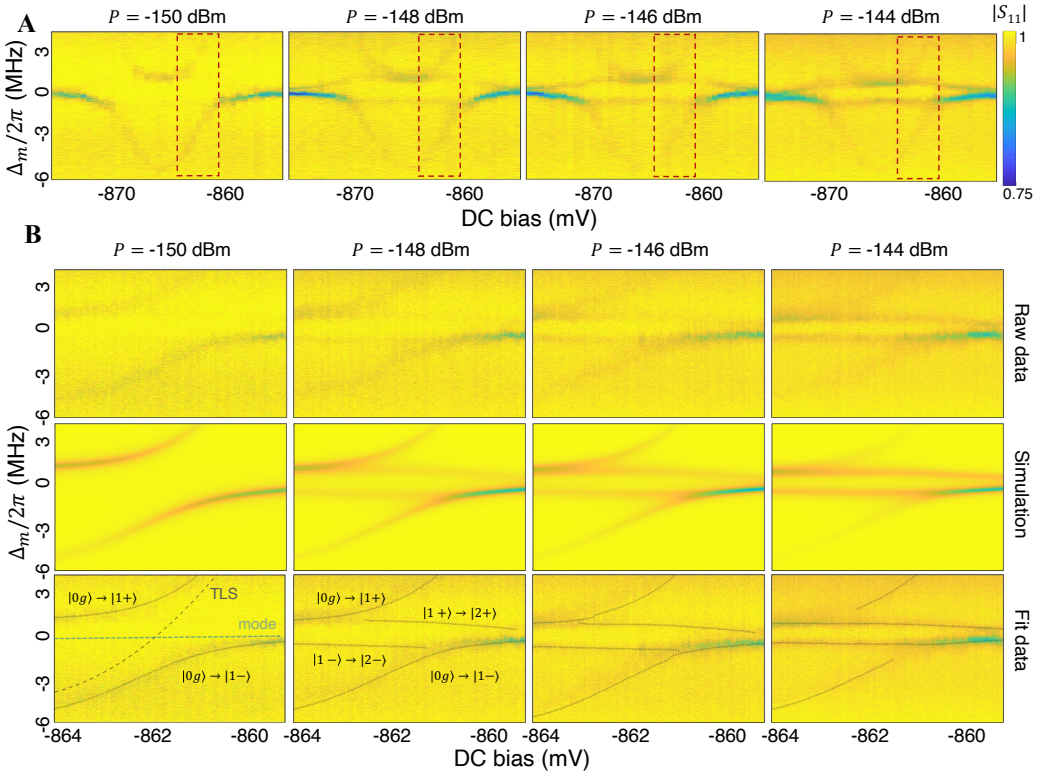

Figure 5.12: **Fine Structure of the Dressed States. (A)** The red square highlights the region where finer sweeps were performed around one of the avoided crossings on TLS,C1. **(B)** A DC sweep in 50 μV increments reveals the fine structure of the crossing and the higher energy transitions as we increase the input power. The stability of the NEMS-TLS system enables continuous and repeatable measurements in the strong coupling regime. Excellent agreement is observed between the experimental results and simulations.

to the transitions $|1-\rangle \rightarrow |2-\rangle$ and $|1+\rangle \rightarrow |2+\rangle$. The corresponding spectral lines are marked in the simulated spectra by black dashed lines. Figure 5.12B shows a DC bias sweep taken with a very fine voltage step size of 50 μV near the single avoided crossing at different incident microwave drive powers P. This is much finer than Fig. 5.10, which were taken with 500 μV steps. In our measurements, we consistently excite higher or lower energy-level transitions by adjusting the input power, demonstrating a means to control the most favored energy transitions of the coupled system.

As the input power increases, so does also the contribution from transitions between higher energy levels, because the transition amplitude increases with the level number. The overall spectrum shifts toward the corresponding transition frequencies.

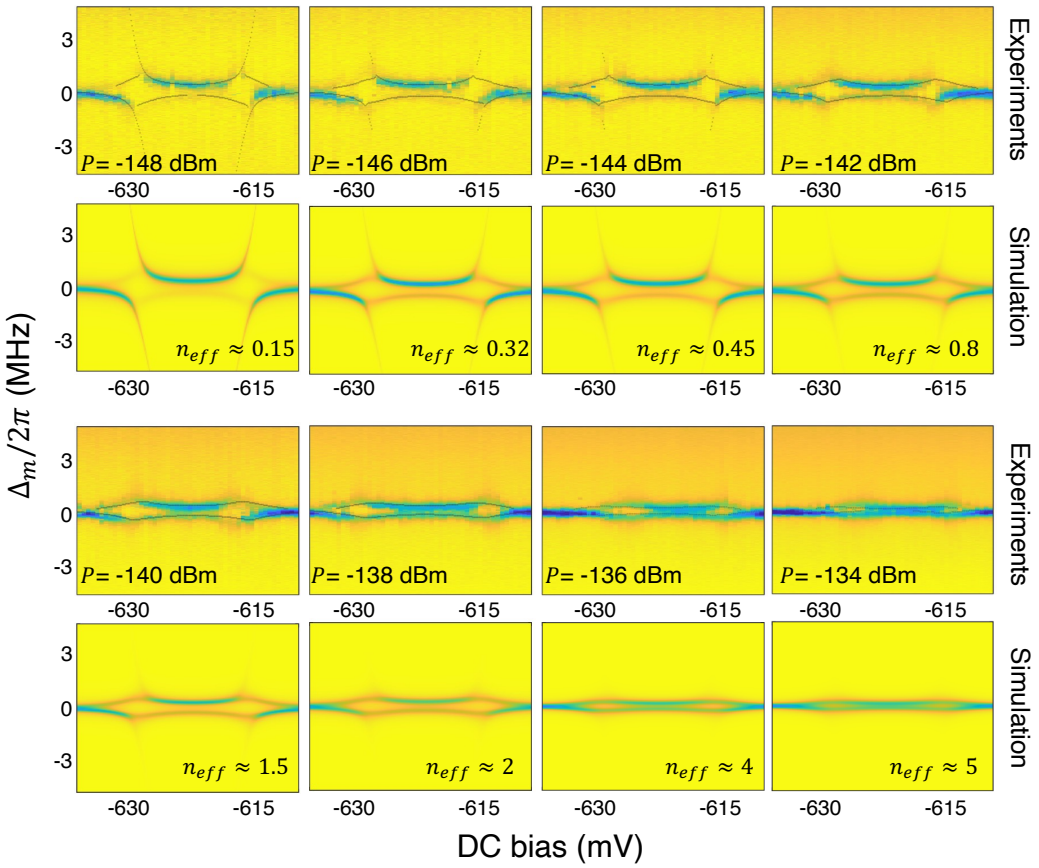

Figure 5.13: **Dressed States of TLS,C2.** Power sweep measurements performed with TLS,C2 demonstrated in Fig. 5.8B. The plot includes experimental data and simulated spectra. The minimas of simulated $|S_{11}|$ are overlaid on the experimental data as black lines to demonstrate agreement with simulations. Compared to TLS,C1, we observe slower increase in n_{eff} with power, possibly due to the lower phonon-TLS coupling strength compared to TLS,C1.

However, the widths of the spectral lines corresponding to individual transitions increases with the level number and ultimately the transitions become unidentifiable [85]. Consequently, the conventional *avoided crossing* pattern gradually transitions to an *eye-like* spectrum as the higher energy level transitions dominate, a phenomenon also observed in spin-circuit quantum electrodynamics (QED) [94]. Eventually, the spectral lines merge together and the system's behavior becomes classical [92, 93]. In our system, this transformation of the spectrum is clearly seen in Fig. 5.10 and Fig. 5.11 for increasing values of the input power.

Associated with the growing population of higher energy levels due to resonant pumping is an overall heating of the resonator. This drive-induced heating effect be-

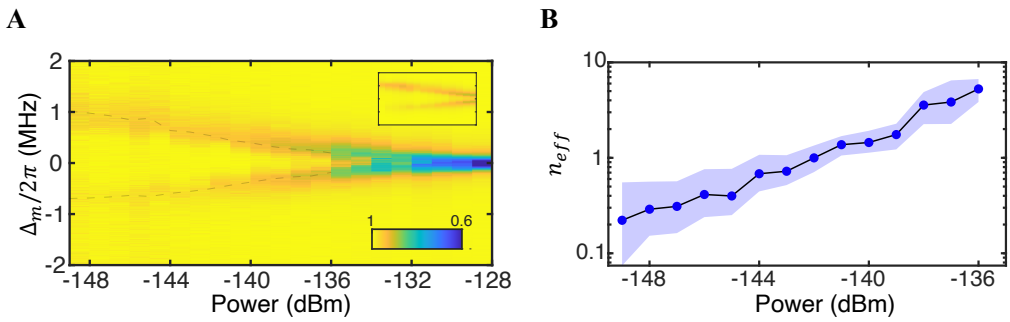

Figure 5.14: **Power Saturation of TLS,C1. (A)** The spectra showing the transition from a frequency-split response to a single resonance response under increased input power acquired at fixed V_{dc}. Dashed lines are the minima of the simulated $|S_{11}|$ spectra shown in the inset. **(B)** Plot of n_{eff} versus input drive power. The shaded region encompasses n_{eff} values that produce simulation results associated with a least-squares error within 5% of the lowest error.

comes evident at high drive powers, where simulations assuming a low, equilibrium phonon number at the stage temperature, n_{th}, no longer match the measured spectra. To properly characterize this drive-induced heating, we must analyze the phonon occupation in the system more carefully. The phonon occupation in our system under a strong microwave drive can be understood by distinguishing between two key populations: the phonons coherently driven in the phonon cavity (mechanical mode) and the thermal phonons in the surrounding bath. A microwave drive with power P is applied to the device, where photons are transduced into mechanical phonons via the piezoelectric effect. The expected number of these coherently-driven phonons, which we term pump phonons (n_{pump}), can be estimated for a resonantly driven cavity:

$$n_{\mathrm{pump}} = \frac{P}{\hbar\omega_d}\frac{4\kappa_e}{\kappa^2}. \tag{5.6}$$

In the absence of other effects, this coherent population would drive multi-phonon transitions from the system's ground state [90]. However, a model that includes only n_{pump} and the base thermal occupancy (n_{th} from the stage temperature) is insufficient to describe our experimental spectra at high drive powers. To achieve agreement with our data, we account for drive-induced heating by introducing an effective thermal phonon number (n_{eff}), which replaces n_{th} in the Lindblad dissipators of our master equation. This parameter along with the dissipation rates $\kappa_i, \gamma_{TLS}, \kappa_e$ is estimated by iteratively minimizing the error between the simulated and experimental spectra,

see Appendix C for details. Figure 5.10 displays the simulated spectra alongside the experimental data, demonstrating excellent agreement with the corresponding n_{eff} values indicated in the plots. Figure 5.11 further illustrates the evolution of the TLS,C1 crossing as the input power is increased from -148 dBm to -136 dBm in 2 dB increments, demonstrating good agreement with the simulated spectra.

While this model is effective, the precise physical mechanism for the heating remains an open question. One possibility is inefficient thermalization at high pump powers; because the mechanical mode occupies a very small volume and is connected to the bath only through narrow tethers and phononic-crystal structures, energy from the drive can accumulate in the mode rather than being quickly dissipated. Other potential causes include off-resonant absorption by a dense background of other TLSs, intrinsic material dissipation, and nonlinear effects under the strong pump field, all of which are known to cause drive-induced effects in similar solid-state quantum systems [95, 96].

We further characterize this power saturation behavior of the strongly coupled TLS in Fig. 5.14A which demonstrates spectrum of $|S_{11}|$ near ω_m as a function of power at a fixed DC ($V_{\mathrm{dc}} = -860$ mV), corresponding to the near-resonance condition ($\omega_m \approx \omega_{\mathrm{TLS}}$). A steady decrease in the frequency splitting with increasing P marks the transition to a classical response. Simulated results, shown in the inset Fig. 5.14A, closely align with the experimental data. Fig. 5.14B plots the n_{eff} used in the simulations for each power.

While we mostly focused on measurements with TLS,C1, we have also performed the same power sweep experiments with TLS,C2 by tuning the bias to near ~ -630 mV. Much like TLS,C1, Fig. 5.13 shows that increasing the incident power induces higher-level transitions, giving rise to an *eye-like* crossing. The extracted n_{eff} values indicate a weaker dependence on power for TLS,C2 compared to TLS,C1, likely due to the smaller phonon-TLS coupling strength of 1.7 MHz, compared to 2.4 MHz for TLS,C1.

In the next set of experiments, we apply a weak drive power ($P = -150$ dBm) while controllably increasing the stage temperature. Figure 5.15A, C, and E display the measured and simulated TLS,C1 crossings for the temperatures of 50 mK, 200 mK, and 500 mK, respectively. As the temperature increases, we observe the emergence of a quadruplet of spectral lines and a gradual transition to the classical response at more elevated temperatures. This behavior closely mirrors that reported in cavity QED systems [97, 98], and aligns with the power sweep measurements demonstrated

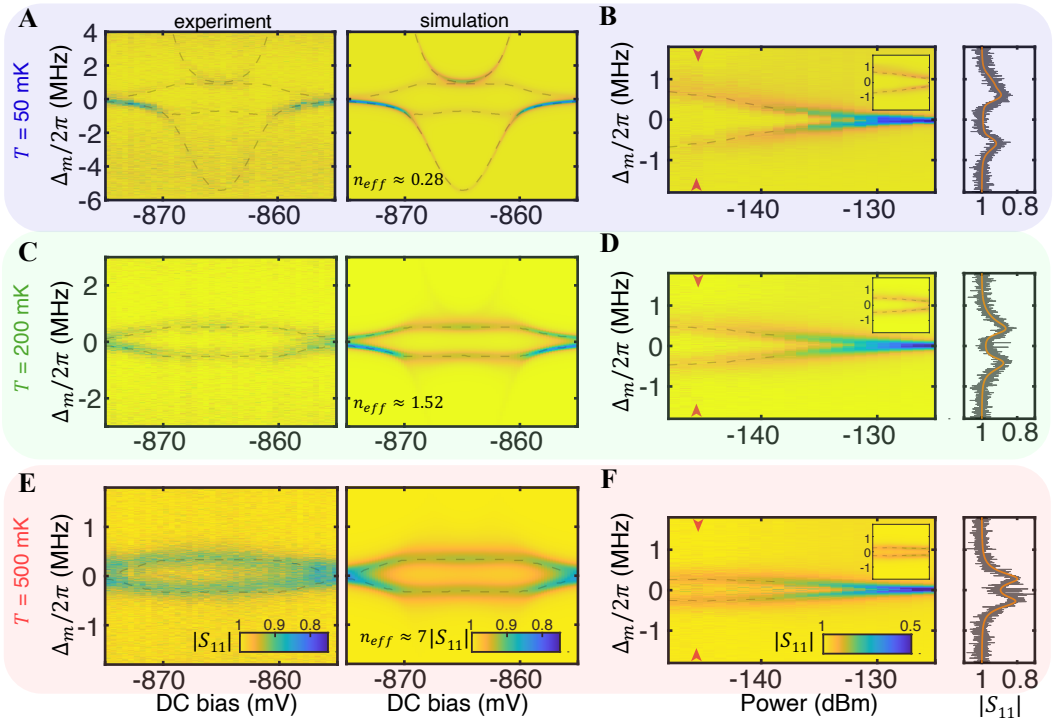

Figure 5.15: **Temperature Effect. (A)** $|S_{11}|$ measurements of TLS,C1 at low input power $P = -150$ dBm and at $T = 50$ mK. The dashed lines are the $|S_{11}|$ minima at each DC bias obtained from simulations. **(B)** Power dependent $|S_{11}|$ response acquired with the fixed DC bias that puts $\omega_m \approx \omega_{TLS}$, demonstrating the transition to a classical response. The inset shows the corresponding simulation results, the minima of which are overlaid as black dashed lines on the measured spectra. In the right panel, the $|S_{11}|$ spectrum for $P = -145$ dBm (marked by red arrows) is plotted with the corresponding fit (orange). Panels (C, D) and (E, F) show the same measurements as (A, B), acquired at 200 mK and 500 mK, respectively.

earlier. Figure 5.16A shows the $|S_{11}|$ spectrum as a function of temperature for a fixed V_{dc}, with simulated results in the inset. The estimated $n_{eff}(T)$ closely follows the expected thermal phonon occupation $n_{\mathrm{th}}(T)$ (Fig. 5.16B) when we take the stage temperature as a reference. This indicates that the hybrid system remains well-thermalized with the stage under weak driving conditions. In Fig. 5.15B, D, and F, we examine the gradual transition from the split to the classical response on-resonance ($\omega_m \approx \omega_{\mathrm{TLS}}$) as we sweep P at the different stage temperatures. On the right side of each panel, we provide a specific $|S_{11}|$ trace at $P = -145$ dBm. Figure 5.17 plots the n_{eff} used to simulate the experimental data for the power sweeps which suggests the coupled system is more sensitive to changes in coherent drive power at low temperatures, whereas at higher temperatures the spectrum shows

constant splitting up to certain power before it gradually decreases (Fig. 5.15F).

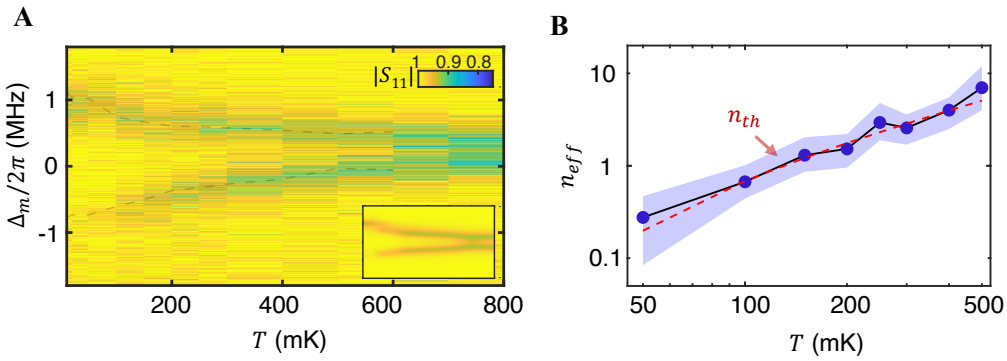

Figure 5.16: **Quantum Thermometry. (A)** $|S_{11}|$ spectra acquired with a fixed DC bias ($\omega_m \approx \omega_{TLS}$) and low power ($P = -150$ dBm) as temperature increases. The dashed line is a fit from the simulations displayed in the inset. The n_{eff} used in the simulations is shown in **(B)**, which overlaps with the Bose-Einstein predicted thermal occupancy (n_{th}), highlighting good thermalization of the device. The blue area indicates the 5% uncertainty range.

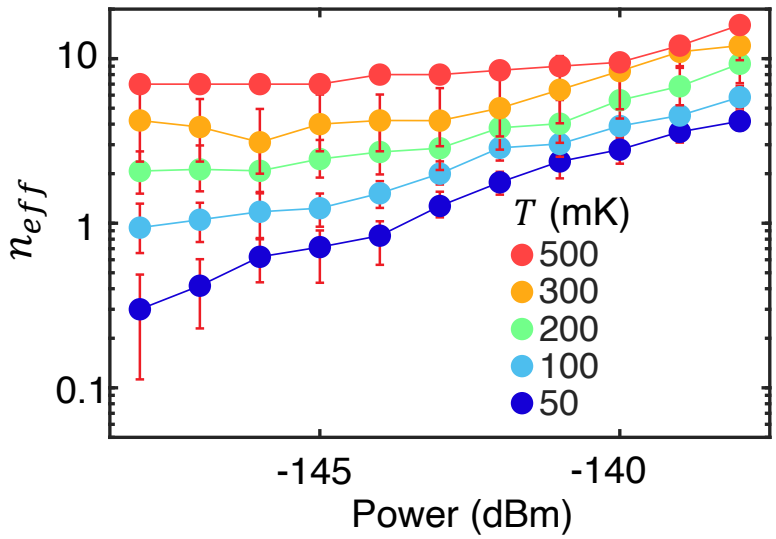

Figure 5.17: **Power Effect at Different Temperatures.** The n_{eff} values used in simulations to reproduce the experimental data at varying power and temperature.

The occupation of higher levels is a combination of both effects, with the dominant contributor depending on the temperature. At low temperature (10 mK): The occupation is primarily driven by the pumping tone (n_{pump}), as supported by our data. At high temperatures: The occupation is dominated by the large initial thermal phonon

population (n_{th}). We observe that the spectral features remain constant until a high power threshold is reached. This indicates that the occupation is determined by the thermal bath ($n_{\text{eff}} \approx n_{\text{th}}$), and the effect of n_{pump} is negligible until very high powers. This behavior is better understood from the analysis presented in Fig. 5.18 where we plot the n_{eff} and n_{pump} as a function of drive power.

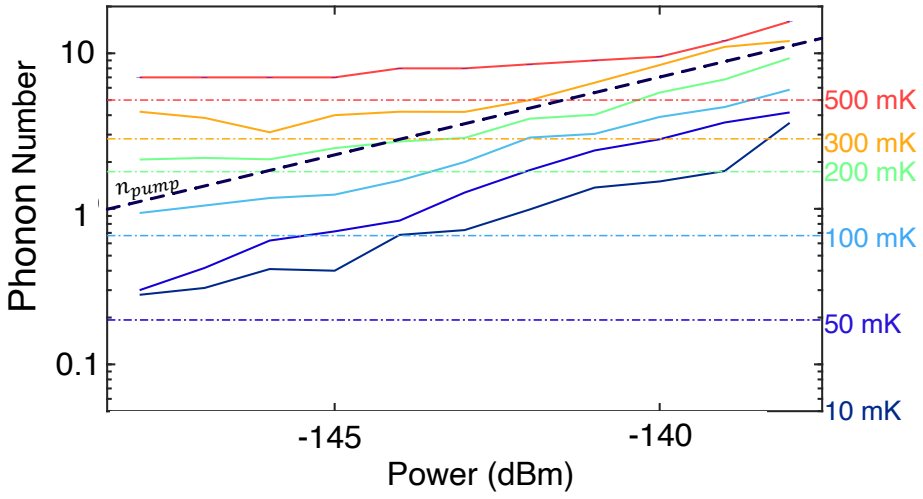

Figure 5.18: **Phonon Occupation.** The estimated effective thermal phonon number, n_{eff} (solid lines), is plotted as a function of drive power for various base temperatures, similar to Fig. 5.17. For comparison, we show the calculated coherent phonon occupation from the input drive, n_{pump} (dashed line), and the theoretical thermal occupations, n_{th} (horizontal dash-dotted lines), for each temperature.

The high sensitivity of the spectrum to temperature suggests a potential application in thermometry. The core idea comes from that strongly coupled TLS–NEMS device exhibits single-phonon sensitivity via its nonlinear (JC ladder) energy spacing: the addition of one phonon shifts the dressed-state frequencies by an amount that far exceeds the linewidth. Since temperature increase populates phonon levels, one can—in principle—map measured spectral shifts (and thus inferred back to an effective temperature). In fact, this system can be utilized for two kinds of thermometry applications:

- Low-Power Environmental Thermometry: At low drive power where heating is negligible, the device's single-phonon sensitivity allows it to function as a standard quantum thermometer. We present preliminary data for this in Fig. 5.16.

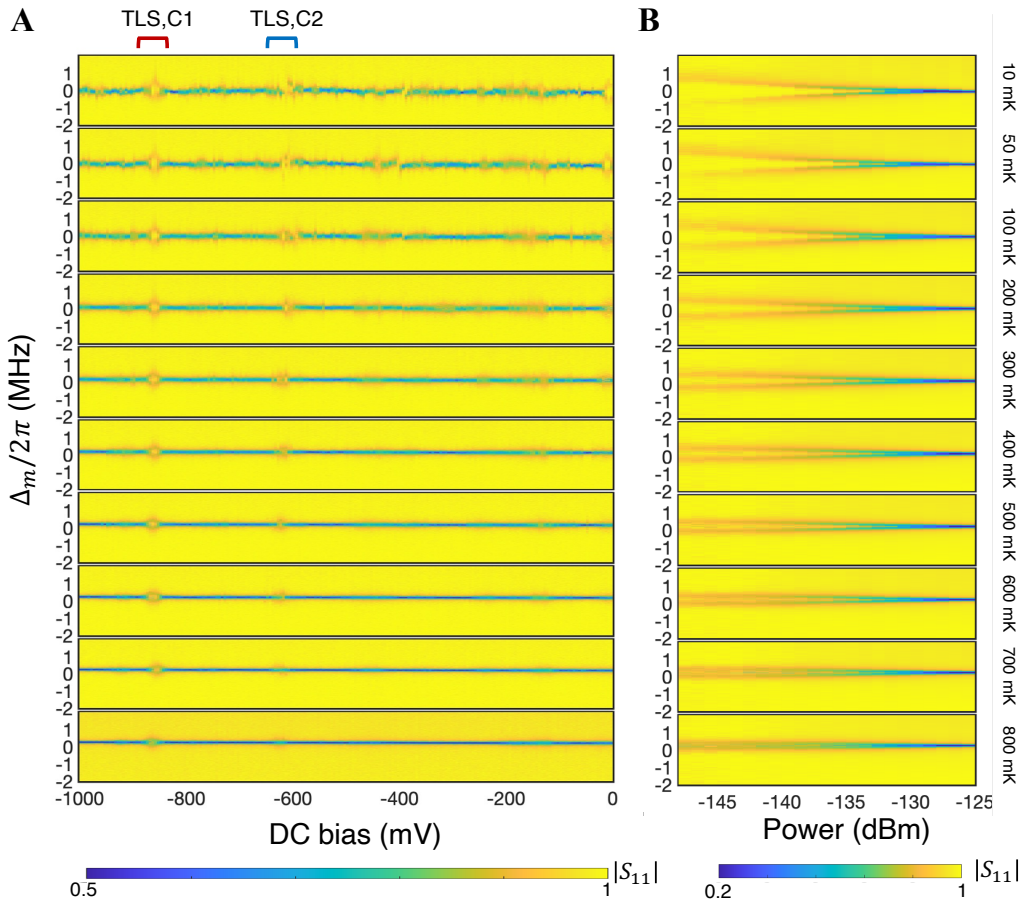

Figure 5.19: **Stability of TLS,C1.** **(A)** A wider DC sweep from -1 to 0 V reveals a variety of spectral features at lower temperatures, most of which saturate at higher temperatures. TLS,C1, the strongest coupled TLS we found, maintains its characteristics even at 800 mK. **(B)** Transition to the classical response of TLS,C1 at different temperatures. This figure complements Fig.5.15B,D,F by presenting the full temperature sweep. As the temperature increases, the splitting is less sensitive to the input power as we observe constant splitting over a wider power range.

- High-Power In-Situ Thermometry: At high powers, the system becomes a sensitive thermometer for its own drive-induced heating. Our ability to extract n_{eff} from the spectra provides a powerful method to characterize non-trivial dissipation and heating physics in a quantum device under operational conditions.

While in this work we focus on the potential of such a system with physical motives, we emphasize that a fully calibrated quantum thermometer will require further engineering.

In addition to its sensitivity, our TLS-NEMS platform exhibits remarkable stability and reproducibility. This is demonstrated in Figure 5.19, which maps the TLS anticrossings over a broad DC bias range as the device temperature is swept from 10 mK to 800 mK at a fixed drive power of −140 dBm. We observe more crossings at lower temperatures, as at high temperatures most TLSs saturate. The most strongly coupled defects (TLS,C1 and TLS,C2) consistently appear at the same DC bias voltage despite us repeatedly sweeping the DC bias over a broad range and changing the temperature for each measurement. This high degree of stability is a key prerequisite for developing practical applications. For example, while a fully calibrated quantum thermometer will require further engineering, the inherent stability we observe is a promising feature for such future devices.

5.3 State Switches of TLS

Along with the frequency splitting discussed in earlier sections, we observe switching of the S_{11} spectrum between a split response and a classical linear resonator response. These fluctuations occur across a range of DC tunings and temperatures and are observed with various resonators. The fluctuations we study here are observed with TLS,C1 when we increase the temperature.

We characterize these slow fluctuations through time-domain reflection measurements, $S_{11}(t)$, taken at a fixed drive frequency ω_d close to $\omega_m \approx \omega_{\mathrm{TLS}}$. Figure 5.20A demonstrates RTS observed at $T = 600$ mK, $P = -135$ dBm, and $\Delta_m = 0$. First, we extract the probability density function (PDF) of $|S_{11}(t)|$ using kernel density estimation (KDE). The presence of RTS yields two distinct peaks. From these peaks, we construct a ladder plot by assigning each data point to its nearest peak value, and then overlay it on the experimental data in Fig. 5.20A (see red line). We then identify the switch instants and calculate the time spent (dwell-time) in the split spectrum (the quantum response) and in the classical single-lorentzian response, denoted as D_q and D_c, respectively. By analyzing numerous switching events, we gather sufficient statistics to study their probability distribution. In Fig. 5.20B, we estimate the PDF of the dwell times by constructing histograms, which fit well to an exponential distribution of the form ($\lambda e^{-\lambda t}$). This indicates that the switching process follows Poisson statistics with a rate λ. From these fits, we extract the switching rates $\lambda_{q\to c}$ and $\lambda_{c\to q}$, corresponding to the transitions from quantum to classical and classical to quantum responses, respectively. We can now examine how these rates and jump amplitudes vary with different experimental parameters.

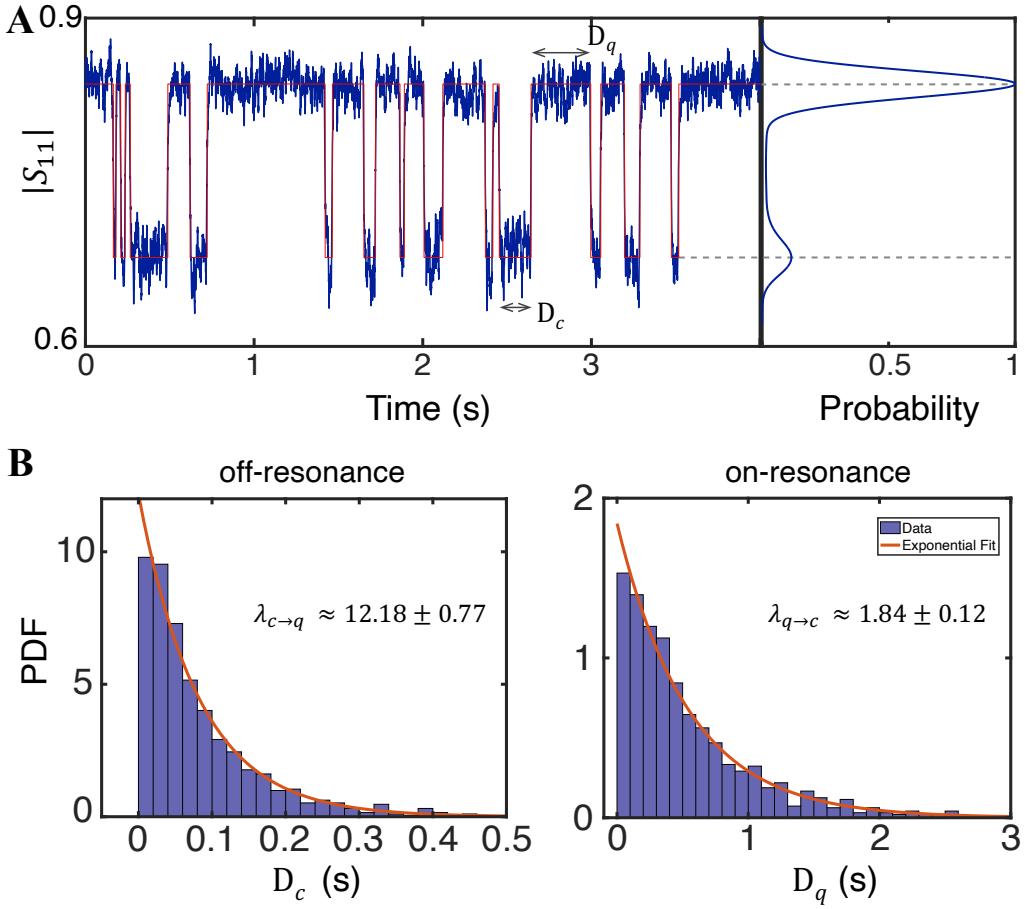

Figure 5.20: **Random Telegraph Switching.** **(A)** Time series data of $|S_{11}|$ recorded at 600 mK with a fixed drive frequency ($\omega_d \approx \omega_m$) reveals clear fluctuations between two stable states. In the right panel, the probability density function (normalized to its maximum value) of the time series data is shown. The two distinct peaks in the density are used to generate the ladder plot (red) superimposed on the raw time series data (blue), highlighting the switching events. **(B)** Histogram of the time durations spent in the lower (D_c) and higher amplitude (D_q) states, extracted from the time series data. An exponential fit (red curve) is applied to determine the switching rates between the states, $\lambda_{c\to q}$ and $\lambda_{q\to c}$.

We collect time-domain traces of $S_{11}(t)$ at different drive frequencies (ω_d) across ω_m. For each frequency, we obtain a probability distribution of $S_{11}(t)$ and extract the values at the peaks. In Fig 5.21, we demonstrate how the probability distribution peaks from $|S_{11}|(t)$ evolve around these frequencies. In Fig. 5.22, each data point represents the peak value obtained at a given detuning Δ_m, with the higher probability peak shown in blue and the lower in gray. Strikingly, the resulting spectra reveal two stable values of $|S_{11}|$ and the phase shift of the reflected signal $\angle S_{11}$, corresponding

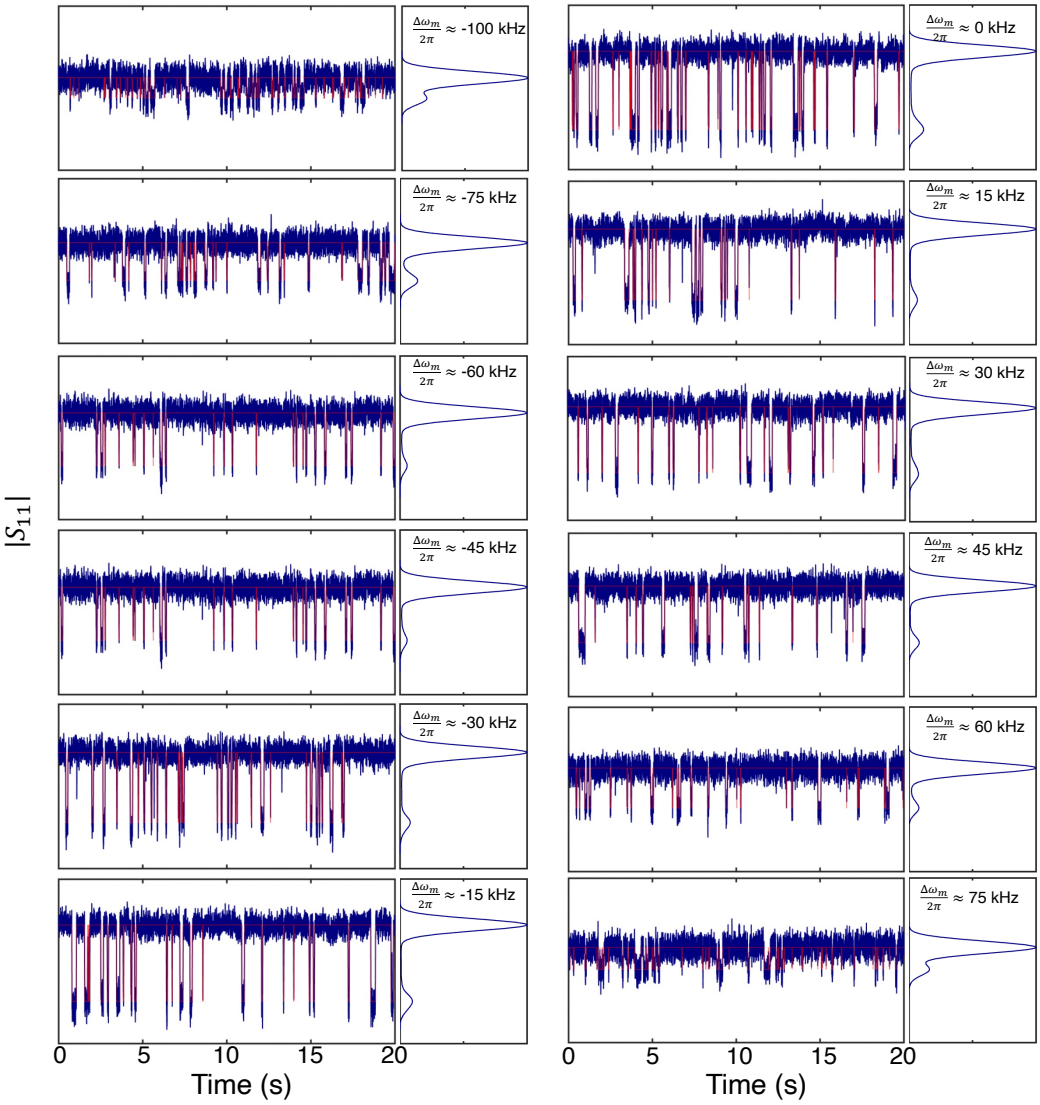

Figure 5.21: **RTS Around Resonance.** **(A)** Time series data collected over 20 seconds while sweeping the drive frequency (ω_d) around resonance, and the corresponding probability density plot is provided on the right for each detuning within the same $|S_{11}|$ interval. The distribution reveals fluctuations between two distinct peaks, which are used to plot the reflection coefficient, $|S_{11}|$.

to the classical linear resonator response (gray) and the split response (blue) of the NEMS-TLS system. This switching behavior remains highly stable over a wide temperature range (Fig. 5.23). We do not observe RTS away from the mode's frequency. Unlike the switch amplitudes, Fig. 5.24A indicates that the switching rates show no significant dependence on frequency detuning. Moreover, $\lambda_{c\to q} > \lambda_{q\to c}$ indicates the system response is predominantly the split response.

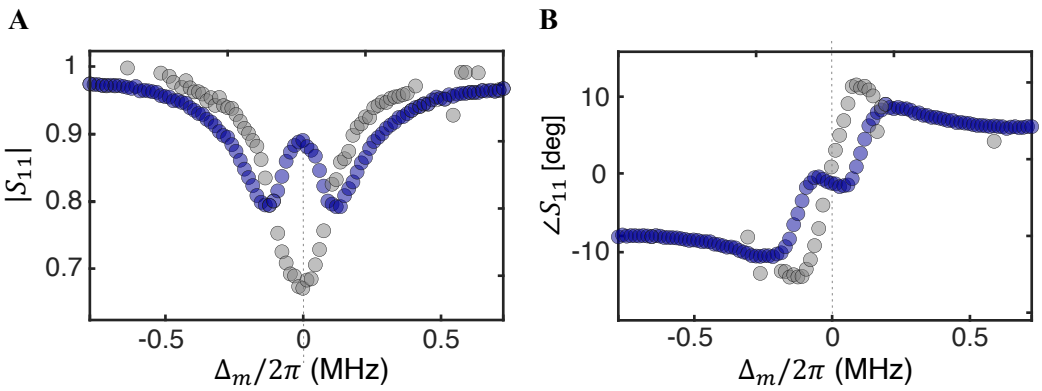

Figure 5.22: **TLS State Switches. (A)** $|S_{11}|$ and **(B)** $\angle S_{11}$ are constructed using the peak values from the probability density of each time series data across different Δ_m, demonstrated in Fig. 5.21. This reveals that the observed fluctuations correspond to the system transitioning between quantum and classical responses.

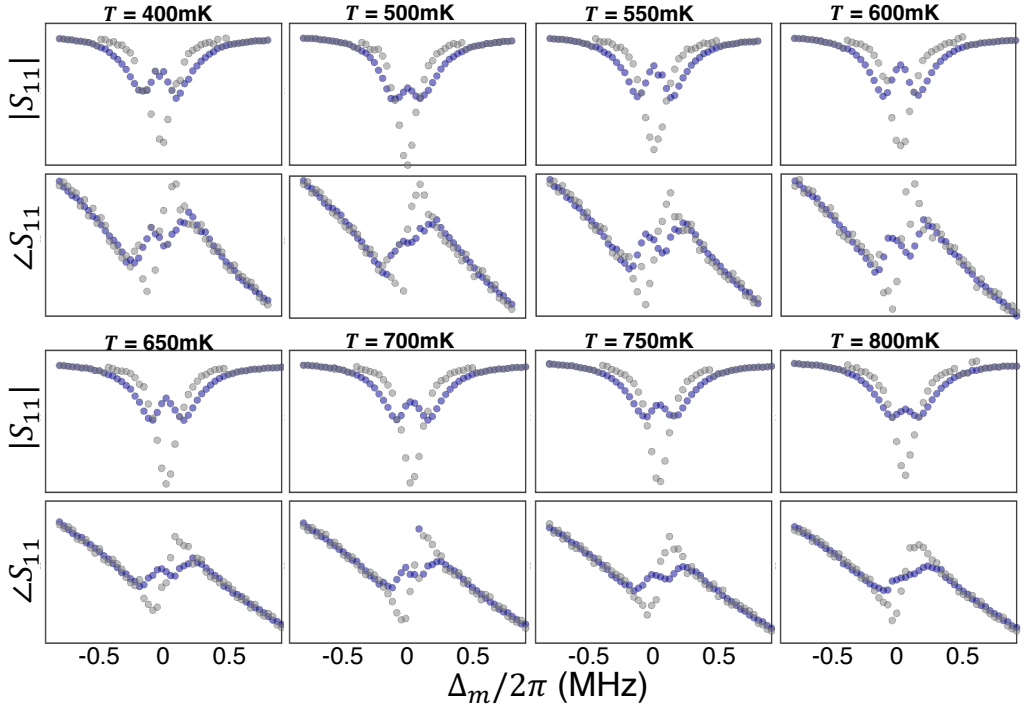

Figure 5.23: **State Switches at Different Temperatures.** Measurements similar to those demonstrated in Fig.5.21 and 5.22 are repeated for varying temperatures. RTS behavior is very stable which allows us to perform more statistical analysis on the data.

In Fig. 5.24B, we fix ω_d on resonance ($\Delta_m = 0$) and vary the coherent drive power P within the range where split-response remains observable. The switching rates

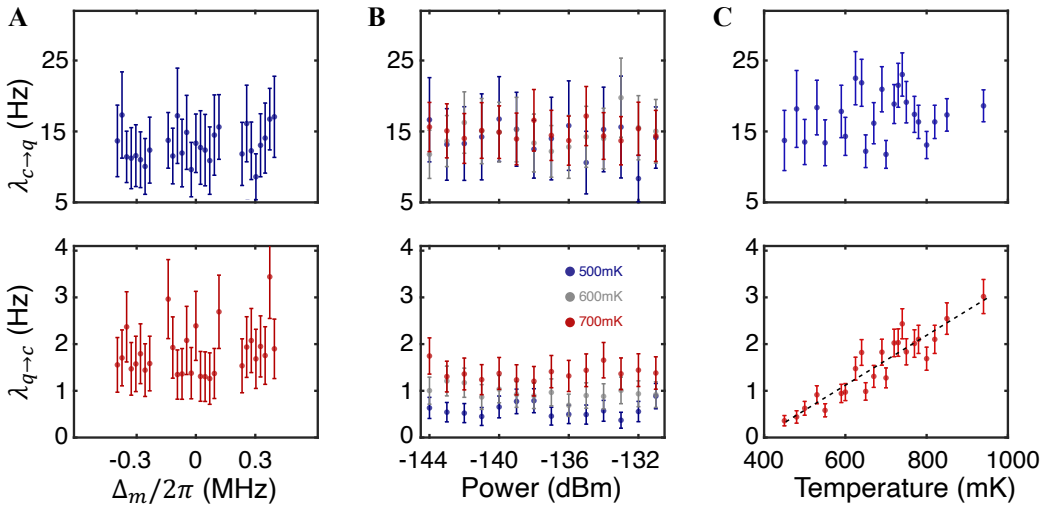

Figure 5.24: **Dependence of Switching Rates.** **(A)** Switching rates as a function of detuning around the mechanical resonance show no significant dependence. **(B)** Dependence of switching rates on input power for three different stage temperatures. **(C)** Temperature dependence of the switching rates.

obtained at three different stage temperatures remain insensitive to power. We note here that since the thermal bath is already at high temperatures, the power effect is minimal for the considered power range, as we demonstrated in the previous section. In Fig. 5.24C, we collect the RTS data at a fixed power while increasing the stage temperature and find that $\lambda_{q\to c}$ increases linearly with temperature, reflecting a higher probability of observing the classical response, while $\lambda_{c\to q}$ remains largely unaffected. This suggests that the $q \to c$ transitions are thermally initiated, while there is a faster and weakly dependent on temperature relaxation process that leads to $c \to q$ transitions.

The RTS can be explained by the TLS frequency fluctuating between on- and off-resonance with the mechanical mode, resulting in a split spectrum (on-resonance) or a classical response (off-resonance). Similar telegraphic switching has been reported in superconducting qubits and microwave devices, where it was attributed to coupling of TLS to an off-resonant two-level fluctuator (TLF), which undergoes thermally driven random transitions between its eigenstates [80, 99–102]. While a similar mechanism may be involved in our system, as the switching shows sensitivity to temperature but not to resonant drive power, the complex dynamics of TLSs at elevated temperatures and the presence of multiple TLSs make it difficult to definitively identify a single fluctuator.

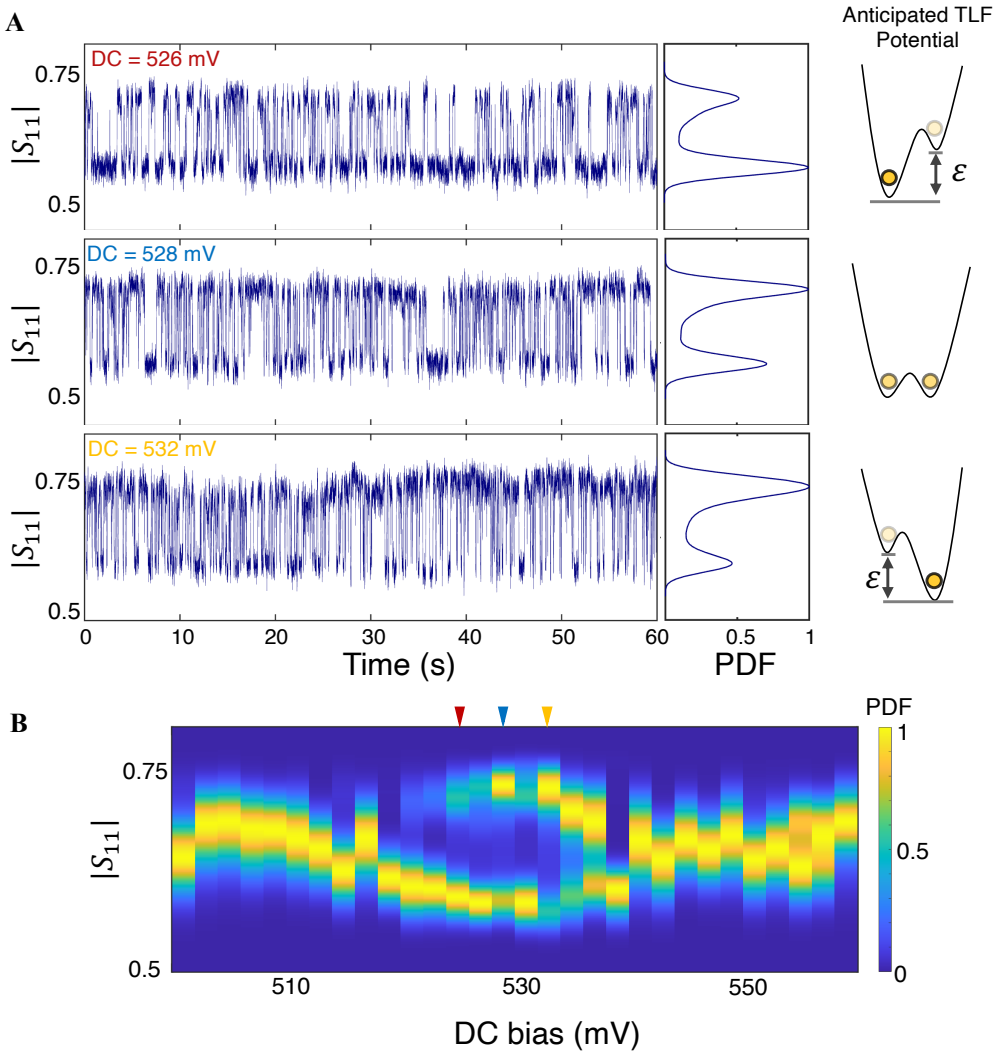

Figure 5.25: **Signatures of Fluctuators.** **(A)** RTS in the reflection amplitude $|S_{11}|$ acquired at 50mK during a different cooldown and using a different resonator from the main text ($\omega_m/2\pi = 1.95$GHz). The RTS in the mechanics is observed as the frequency of the strongly coupled TLS hops between on- and off-resonance. The symmetry of the RTS changes with DC bias, which could be explained by changes in the most probable state in the double-well potential of a TLF strongly coupled to the TLS. **(B)** Heatmap of the normalized probability distributions of the RTS as a function of applied DC bias. The three colored triangles at the top indicate the DC values used in the time series plot in **(A)**. The opening and closing behavior is due to the strongly coupled TLS crossing the mechanics, while changes in the most probable state are likely caused by a fluctuator.

Throughout our study, we could detect RTS at multiple DC voltage settings across various resonators at different stage temperatures. In Fig. 5.25, we demonstrate an example of RTS observed in different resonator ($\omega_m/2\pi = 1.95$ GHz) while

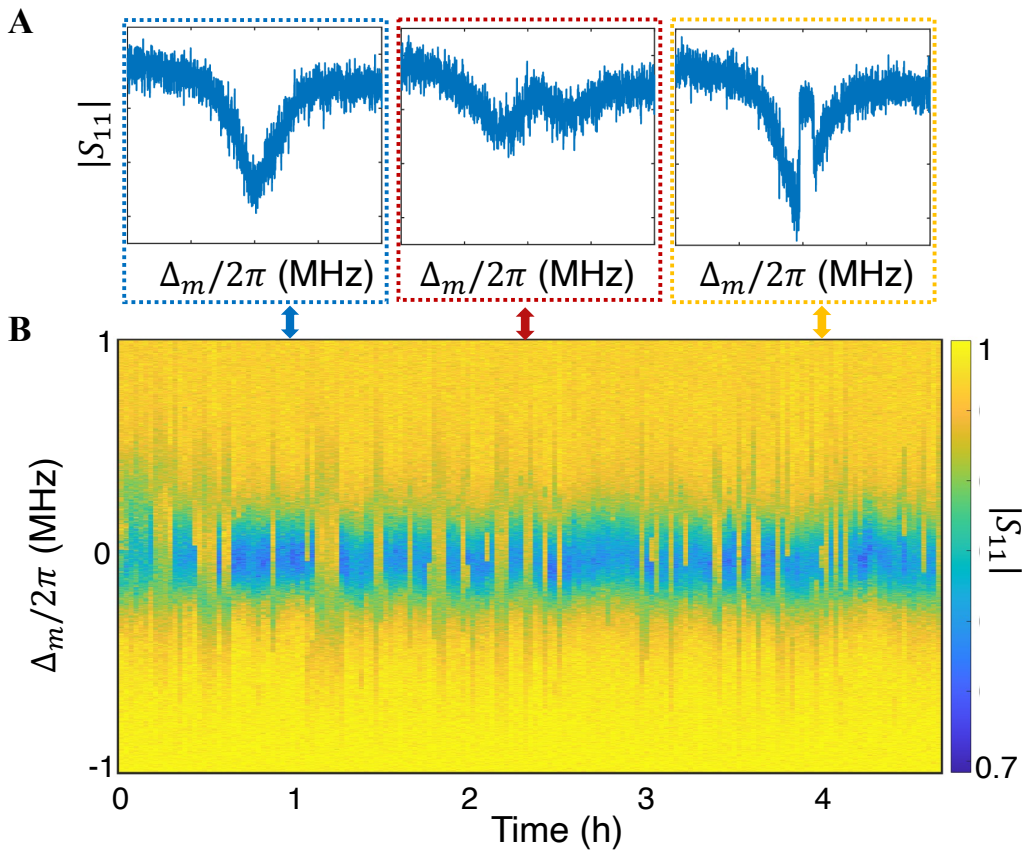

Figure 5.26: **Slow Fluctuators. (A)** S_{11} measurement is repeated at a fixed DC bias, temperature, and drive power over $\sim$ 5 hours. Due to the slow fluctuation process, we observe classical, quantum, and mixed responses at different measurements. **(B)** The spectra from 5 hour repeating measurement of the device response.

at a base stage temperature of 50 mK. In this example, we demonstrate that the probability of occupying either state is directly tunable with the applied DC bias. Figure. 5.25A shows that while near 528 mV, the distribution is mostly symmetric, the reverse asymertry is achieved between the DC biases of 526 mV and 532 mV. Figure. 5.25B emphasizes that by tuning the voltage away from this point, the RTS can be suppressed entirely, forcing the system into a single stable state.

A plausible explanation for this phenomenon is the coupling of our primary TLS to a nearby two-level fluctuator (TLF), which likely originates from another microscopic defect with a double-well potential coupled to the TLS. In this model, the DC bias tunes the energy asymmetry of both TLS's and TLF's double-wells. While strongly coupled TLS crosses the mechanical mode frequency, for TLF it alters which of its two states is energetically favored. Whenever the TLF tunnels between

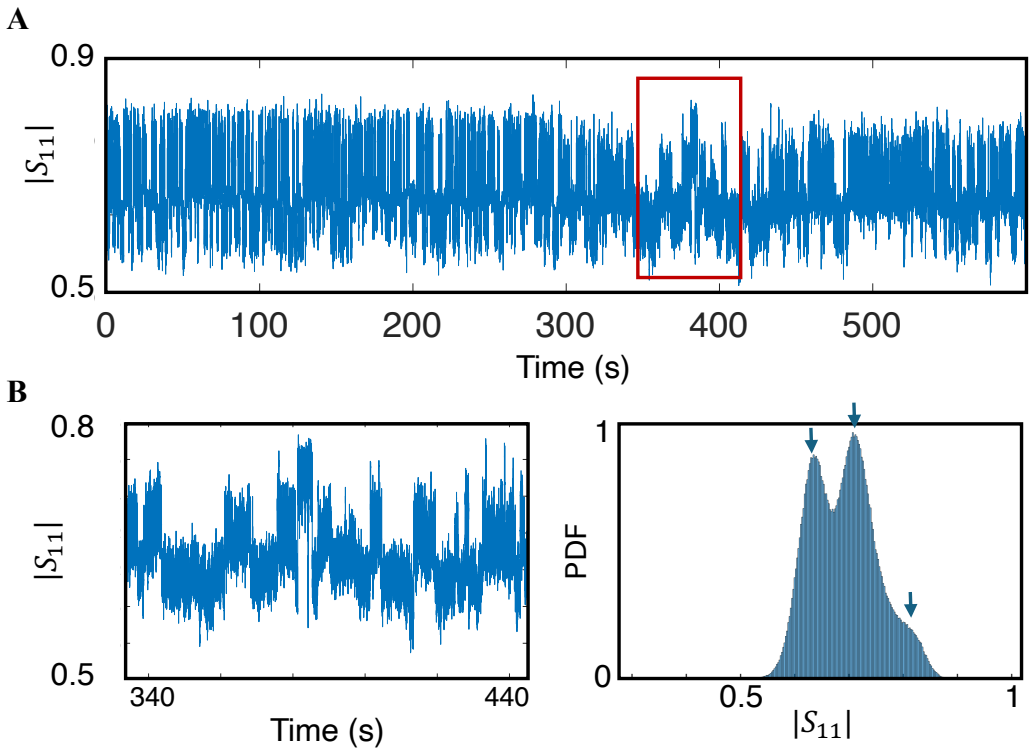

Figure 5.27: **RTS with Three Stages.** **(A)** Time trace of $|S_{11}|$ measured at a fixed DC bias, showing telegraph-like switching. **(B)** A magnified view of the time interval marked in red in **(A)**. The signal exhibits clear, discrete jumps between three stable states. The corresponding histogram of the signal amplitude, plotted on the right, confirms the three-state nature of the dynamics indicated with arrows.

its eigenstates, which are primarily localized in one of the two well minima, it induces a shift in the primary TLS, causing its frequency to jump from on- to off-resonance (or vice versa) and creating the observed RTS. This interpretation suggests we have direct electrical control over the TLF's potential landscape, as depicted schematically in the figure. This ability to tune microscopic fluctuators presents a promising avenue for actively engineering and mitigating quantum noise in solid-state devices.

Beyond simple two-state switching, our platform reveals more complex noise dynamics occurring across various timescales. For instance, Figure 5.26 shows dynamics on a much slower timescale. In this measurement, instead of getting a time series data, we performed continuous frequency sweep measurement across the resonance frequency, while keeping all the parameters fixed (e.g., DC bias, applied power, and temperatue). Here, repeated frequency sweeps taken over five

hours at fixed parameters show the system's frequency response changing over time, intermittently exhibiting quantum (split), classical (unsplit), or mixed responses. This demonstrates that the fluctuations due to TLS defects might have different time-scales. In another example, Figure 5.27 shows a clear random telegraph signal between three distinct stable states of the resonator.

All these observations—spanning different resonators, timescales, temperatures, and drive powers—highlight the complex nature of TLS interactions with mechanical vibrations and within each other. However, these measurements also proves that our platform is an excellent and versatile tool for characterizing these intricate quantum phenomena.

5.4 Discussion and Future Work

The observation of strong coupling in a NEMS resonator with atomic-scale defects marks the first successful observation of phonon-TLS coupling in a solely *mechanical* system. Our findings provide new insights into TLS-phonon interactions, particularly the nature of mechanical decoherence, thermalization and drive-induced heating in the single-phonon regime where quantum applications are realized. The spectroscopic signatures of this strong interaction serve as an unambiguous hallmark of the system's non-classical, quantum nature. This discovery paves the way for future time-domain control and the preparation of specific non-classical states. Our ability to control and populate higher energy states of the hybridized system could enable the preparation and control of more exotic quantum states stored purely within mechanical vibrations. Furthermore, the TLS-induced nonlinear scaling of the energy levels can be engineered as a highly sensitive quantum thermometer.

The robustness, reproducibility, and stability of our platform is validated through repeated measurements across different setups and resonators at both Caltech and Stanford. The discovery that nonlinear quantum behavior can be sourced from a single, naturally occurring microscopic TLS defect within a macroscopic nanomechanical object opens new paths for nanomechanics in quantum regime, with implications for both fundamental research and quantum applications. The observation of these quintessentially quantum effects in such a minimal platform – requiring only a nanostructured piece of lithium niobate – demonstrates that quantum acoustics can arise naturally from the intrinsic couplings within a material, without the need for superconducting or complex electromagnetic circuitry or hybrid quantum integration. Combined with the robustness and reproducibility of our observations,

the simplicity of our setup suggests that other approaches to quantum-engineered acoustic fields for sensing and computing may be worthwhile.

While the TLS defects in this work appeared randomly, a key challenge ahead is the engineering of strongly coupled TLS defects to the mechanical mode. Techniques such as in-situ surface oxidation [103] could be used to introduce TLS defects at high-strain regions of the mode shape, enabling deterministic placement and coupling strength control. Such defect engineering would complement the intrinsic advantages of our minimal platform, potentially allowing tailored nonlinearity, reproducible quantum behavior, and optimized performance for quantum sensing and state-control applications. Another important direction is to increase the signal-to-noise ratio, enabling time-domain measurements. In combination with engineered TLS defects, this capability could pave the way toward the realization of more robust, complex architectures with mechanical qubits.

Chapter 6

FREQUENCY FLUCTUATIONS IN NEMS DUE TO TLS DEFECTS

[1] M. P. Maksymowych*, M. Yuksel*, O. A. Hitchcock, N. R. Lee, F. M. Mayor, W. Jiang, M. L. Roukes, and A. H. Safavi-Naeini, "Frequency fluctuations in nanomechanical resonators due to quantum defects", arXiv preprint arXiv:2501.08289 (2025),

The study of dissipation and noise processes in nanomechanical devices has attracted significant interest from physicists, as it holds great potential for understanding the microscopic nature of these phenomena. Beyond their fundamental importance, these processes impose critical limits on a wide range of applications, including quantum information and sensing [23, 104–108]. While significant progress has been made in understanding noise in NEMS devices at higher temperatures [50], a thorough characterization of their behavior at the ultra-low temperatures required for quantum experiments has remained elusive.

At millikelvin temperatures, where many quantum experiments are conducted, most sources of dissipation and noise such as nonlinear phonon scattering [109, 110], adsorption-desorption [111], defect diffusion [112, 113], and thermomechanical noise [41, 50, 114, 115] become irrelevant. Ultra-low temperatures suppress thermally activated processes, while high vacuum conditions prevent adsorption-desorption events that could perturb the resonator. A remaining source of loss at millikelvin temperatures is attributed to weak interactions with two-level system (TLS) ensembles, often described by the standard tunneling model (STM) [40, 59, 116, 117], much like macroscopic surface acoustic wave [61, 118, 119] and superconducting [6, 7, 59, 120–122] devices. However, when fields are confined to a nanoscale volume, strong interactions with few TLS should dominate over ensemble effects, challenging our understanding of dissipation in cryogenic nanomechanical resonators. Moreover, recent experiments have revealed that significant dephasing persists even in carefully engineered nanomechanical devices at millikelvin temperatures [12, 14, 77, 123]. These large frequency fluctuations have not been studied in detail and their sources are unknown, necessitating a thorough investigation.

In this chapter, we directly address this critical gap in understanding. We will begin by detailing the advanced frequency characterization methods we have applied to measure and analyze these noise processes at cryogenic temperatures with our PnC nanomechanical resonator mentioned in earlier chapters. Following this, we will present the key results from our measurements and provide a comprehensive analysis of the observed frequency fluctuations, offering new insights into their origins.

6.1 Frequency Noise in NEMS

6.1.1 Brief Introduction to Frequency Noise

Precision oscillators have been playing an important role in various applications including timekeeping, high-speed communication, navigation, and a variety of sensing applications. Over the years, a robust set of methods has been developed to characterize the stability of these oscillators [124]. These methods have been successfully implemented for the characterization of NEMS resonators and modern quantum devices, where frequency stability is a critical concern.

Inspired by the quantitative analysis given in [125], an ideal sinusoidal signal from a perfect oscillator can be described as a simple cosine function with a constant amplitude V_0 and a linearly progressing phase:

$$V(t) = V_0 \cos(2\pi f_0 t). \tag{6.1}$$

Here, V_0 is the nominal amplitude and f_0 is the nominal carrier frequency. A more complete model that accounts for perturbations from random, time-dependent fluctuations can be expressed as:

$$V(t) = [V_0 + \epsilon(t)] \cos[2\pi f_0 t + \phi(t)] \tag{6.2}$$

where $\epsilon(t)[V]$ represents the amplitude noise, and $\phi(t)[rad]$ is the phase noise. Assuming small noise fluctuations, it is convenient to express the signal using a linearized phasor representation. In this form, the total signal $V(t)$ is the real part of a complex vector that cleanly separates the ideal carrier from the noise components:

$$V(t) = \mathrm{Re}\{[V_0 + V_0\alpha(t) + iV_0\phi(t)]e^{i2\pi f_0 t}\} \tag{6.3}$$

where $\alpha(t) = \epsilon(t)/V_0$. This expression separates the signal into a rotating vector for the ideal carrier, $e^{i2\pi f_0 t}$, and a stationary complex envelope, $\mathbf{V}(t)$, which contains all the noise information:

$$\mathbf{V}(t) = V_0 + V_0\alpha(t) + iV_0\phi(t) = V_0 + \mathbf{v_n}(t). \tag{6.4}$$

The total phasor $\mathbf{V}(t)$ is the sum of the large, constant carrier vector (V_0) and a small, fluctuating noise vector $\mathbf{v_n}(t)$. This noise vector is composed of two orthogonal parts: an in-phase component, $V_0\alpha(t)$, which is parallel to the carrier and represents the amplitude noise, and a quadrature component, $iV_0\phi(t)$, which is perpendicular to the carrier and represents the phase noise. This representation is sketched in Fig. 6.1, and elegantly shows how amplitude and phase noise are simply the two orthogonal components of a single complex noise process acting on the ideal carrier.

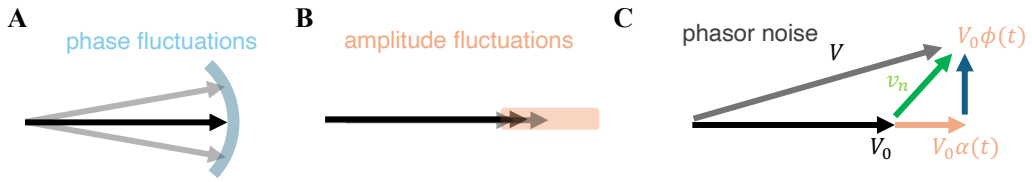

Figure 6.1: **Phasor decomposition of signal noise.** (**A**) Phase fluctuations, $\phi(t)$, correspond to changes in the phasor's angle. (**B**) Amplitude fluctuations, $\alpha(t)$, correspond to changes in the phasor's magnitude. (**C**) The total noise vector, $\mathbf{v_n}$, perturbs the ideal phasor, V_0, resulting in the measured phasor, V. This noise vector can be decomposed into its orthogonal amplitude ($V_0\alpha(t)$) and phase ($V_0\phi(t)$) components.

The phase noise term, $\phi(t)$, is directly related to the instantaneous frequency fluctuations. The instantaneous frequency, $f(t)$, is defined as the time derivative of the total phase, normalized by 2π:

$$f(t) = \frac{1}{2\pi}\frac{d}{dt}[2\pi f_0 t + \phi(t)] = f_0 + \frac{1}{2\pi}\frac{d\phi(t)}{dt}. \tag{6.5}$$

The deviation from the nominal frequency, f_0, is determined by the rate of change of the phase noise. For stability analysis, this is expressed as the fractional frequency deviation, a dimensionless quantity denoted by $y(t)$, which is defined as:

$$y(t) = \frac{f(t) - f_0}{f_0} = \frac{\dot{\phi}(t)}{2\pi f_0} = \dot{x}(t). \tag{6.6}$$

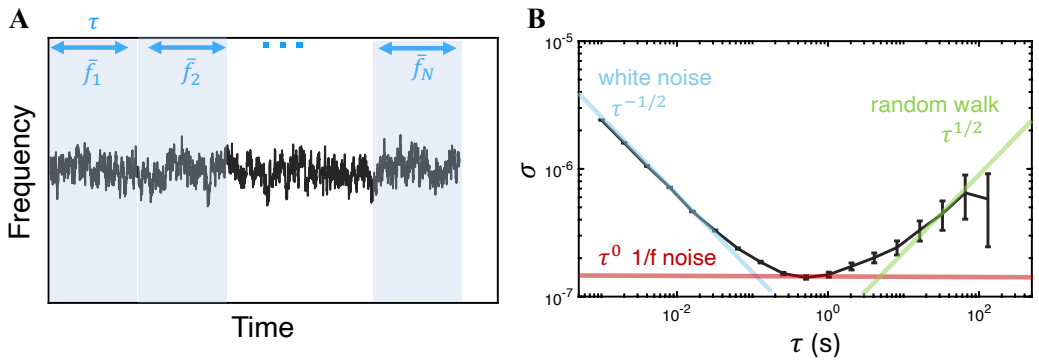

Figure 6.2: **Allan Deviation Analysis of Frequency Noise.** (**A**) Schematic of the measurement process where the frequency time series is divided into intervals of duration τ to compute the average frequency $\bar{f}_k$ for each interval. (**B**) The measured Allan deviation $\sigma(\tau)$ as a function of averaging time. The data reveals distinct noise regimes, indicated by the colored lines corresponding to their theoretical slopes. At short times, the stability is limited by white frequency noise ($\sigma \propto \tau^{-1/2}$). A flicker noise floor ($1/f$ noise, $\sigma \propto \tau^0$) is reached at $\tau \approx 1$ s, indicating a minimum (or best) Allan deviation of $\sigma \approx 1.5 \times 10^{-7}$. At longer times, the stability degrades due to random walk frequency noise ($\sigma \propto \tau^{1/2}$), which is characteristic of slow drifts.

We can separate the characterization of these fluctuation into frequency and time domain. In the frequency domain, a key metric is the Power Spectral Density (PSD), which reveals how the power of the noise fluctuations is distributed across different Fourier frequencies, f as the offset from the main carrier frequency, f_0. PSD of the phase fluctuations $S_\phi(f)$ [rad^2/Hz] is defined as the Fourier transform of the autocorrelation function of the phase noise $\phi(t)$, and $S_\phi(f)$ is related to the PSD of frequency fluctuations $S_y(f)$ [1/Hz] from the definition of $y(t)$, and we can write as:

$$S_y(f) = \left(\frac{f}{f_0}\right)^2 S_\phi(f). \tag{6.7}$$

In the time domain, the Allan deviation, $\sigma_y(\tau)$, provides a measure of the frequency stability of an oscillator over different averaging times, τ, as demonstrated in Fig. 6.2A [126]. It is calculated from a series of discrete measurements of the average fractional frequency deviation, $\bar{y}_k$, where each measurement is averaged over a time interval τ. Given a set of N equally spaced measurements of the average fractional frequency, the Allan variance and the Allan deviation is then simply the square root of the Allan variance, $\sigma_y^2(\tau)$, is defined as:

$$\sigma_y^2(\tau) = \frac{1}{2(N-1)} \sum_{k=1}^{N-1} (\bar{y}_{k+1} - \bar{y}_k)^2. \tag{6.8}$$

By plotting the Allan deviation (Fig. 6.2B) as a function of the averaging time τ, or PSD of frequency fluctuations $S_y(f)$, different noise processes can be identified by the characteristic slopes they produce on the plot. These two methods are used as statistical tools to characterize our NEMS resonator's frequency fluctuations.

The primary strength of using both PSD and Allan deviation is their ability to identify distinct noise processes, which often follow a characteristic power-law dependence. On a log-log plot, these processes manifest as straight lines with specific slopes. For instance, white frequency noise, arising from uncorrelated thermal processes, exhibits a flat power spectrum ($S_y(f) \propto f^0$) and corresponds to a slope of $\tau^{-1/2}$ on the Allan deviation plot. In contrast, flicker frequency noise, also known as $1/f$ noise ($S_y(f) \propto f^{-1}$), is a lower-frequency process ubiquitous in solid-state devices. This noise type produces the characteristic flat floor ($\sigma_y(\tau) \propto \tau^0$) in an Allan deviation plot, which indicates the oscillator's optimal stability. As shown in the example of Fig. 6.2, a typical resonator's stability is limited by white noise at short averaging times before reaching a flicker noise floor at its optimal averaging time, demonstrating how this analysis reveals the underlying physics of the noise.

6.1.2 Frequency Tracking Methods

There are multiple methods to collect a time trace of the resonance frequency $f(t)$ of our NEMS resonators [127], and we have implemented few of them to test our devices. Although these methods fundamentally measure the noise from the same source, they might have advantages over one another for certain applications.

6.1.2.1 Open Loop Method

In the open loop method, first we characterize the resonator's complex transfer function by frequency sweep. This measurement yields the key resonance parameters: the resonance frequency f_0, the quality factor Q, and the phase response curve, $\phi(f)$. We can plot this response in polar coordinates as amplitude (r) and phase, or in phasor diagram as in and out of phase quadratures which reveals the circular resonance locus of the I and Q quadrature components.

After the initial characterization of the resonance, we apply a drive tone at a fixed frequency f_d from a reference signal generator with a low noise close to the resonance

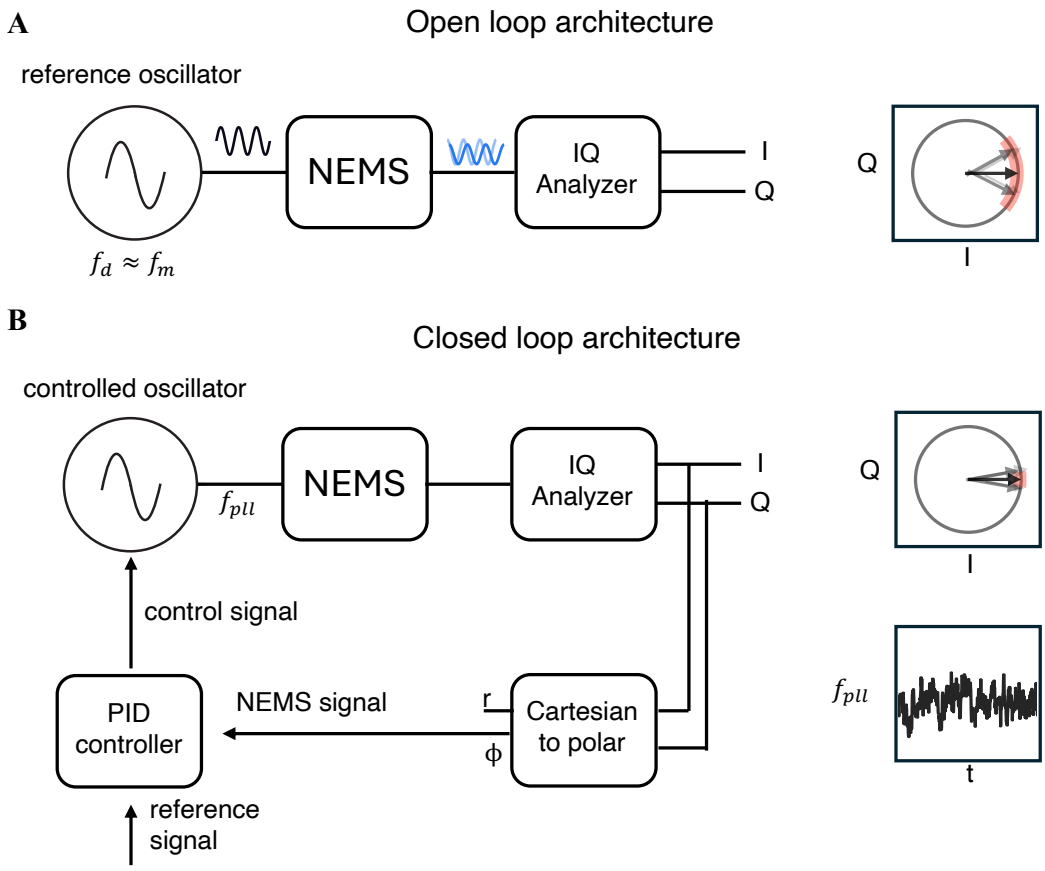

Figure 6.3: **Frequency Tracking Architectures.** (**A**) In the open-loop scheme, the NEMS is driven at a fixed frequency, f_d. The resulting phase fluctuations are measured in the IQ plane (right) and post-processed to determine the frequency noise. (**B**) In the closed-loop scheme, a PID controller forms a phase-locked loop (PLL) that actively adjusts the drive frequency, f_{pll}, to track the NEMS resonance. The feedback suppresses the tangential (phase) noise in the IQ plane, and the time trace of $f_{pll}(t)$ becomes the direct measurement of the resonator's frequency fluctuations.

frequency f_0 and measure the resonator's response. While the drive tone is still on, we record the phase response over time and observe fluctuations around the on-resonance phase value $\delta\phi(t)$. Then, we can infer to the frequency fluctuations from the phase fluctuations:

$$\delta f(t) = \frac{\delta\phi(t)}{\left.\frac{d\phi}{df}\right|_{f=f_d}}. \tag{6.9}$$

In the I/Q plane, these fluctuations are observed as movements of the measurement point around the fixed point on the resonance locus corresponding to the drive

frequency f_d. As established in our noise model in Fig. 6.3, fluctuations tangential to the locus correspond to phase noise, $\delta\phi(t)$, while radial fluctuations correspond to amplitude noise, $\alpha(t)$. The open-loop method essentially measures these tangential deviations and scales them to determine the frequency noise.

In practice, this is achieved by analyzing the complex response $V(t) = I(t) + iQ(t)$ measured in the IQ plane. For a fixed drive, the response fluctuates around a mean point on the resonance circle, V_d. The small, complex fluctuation vector, $\delta V(t) = V(t) - V_d$, contains both amplitude and phase information. To isolate the phase component, the fluctuation vector is normalized by the mean response and its imaginary part is taken. This procedure effectively projects the noise onto the tangential direction:

$$\delta\phi(t) = \mathrm{Im}\left(\frac{\delta V(t)}{V_d}\right) = \mathrm{Im}\left(\frac{V(t) - V_d}{V_d}\right). \tag{6.10}$$

Once this time trace of phase fluctuations, $\delta\phi(t)$, is extracted from the IQ data, it is converted to frequency noise, $\delta f(t)$, using the resonator's measured phase slope, $d\phi/df$. This linear conversion is highly effective but assumes the frequency fluctuations are small compared to the resonator's linewidth. For a more precise characterization, especially in the presence of large frequency fluctuations, a more robust technique, locus projection method [128] can be used. Instead of relying on a local linear approximation, this method directly compares each measured data point, $S_j = I_j + iQ_j$, to the ideal resonator model, $S_{11}(\omega)$. The instantaneous frequency $\omega_{0,j}$ for each sample is determined by finding the frequency on the ideal locus that minimizes the squared geometric distance to the data point:

$$\omega_{0,j} = \mathrm{argmin}_\omega |S_j - S_{11}(\omega, \mathbf{p})|^2. \tag{6.11}$$

While simple and effective for measuring small, fast fluctuations, the open-loop method has limitations. Its primary drawback is a limited dynamic range; if the resonator's frequency drifts by an amount comparable to the resonance linewidth, the operating point moves away from the linear region of the phase slope, or out of the locus and invalidates the conversion to frequency. Furthermore, this method is passive and does not actively track the resonance frequency, therefore, it cannot be used for mass sensing applications.

6.1.2.2 Phase Locked Loop

Phase-locked loop (PLL) method is the most commonly used frequency tracking method by implementing a closed-loop controller. PLL actively adjusts the drive frequency, f_{drive}, to keep the phase of the resonator's response locked to a constant setpoint, ϕ_{ref}. This setpoint is set to the resonance phase ϕ_0, and usually adjusted to 0 value for simplicity. The implementation can be done in analog domain using Voltage-Controlled Oscillator (VCO), however, with the advancements in FPGA based hardware, the controller is mostly done in digital environment with Digitally-Controlled oscillators (DCO). During operation, the demodulator of the lock-in amplifier continuously compares the phase of the resonator's output, ϕ_{out}, with the reference phase, ϕ_{ref}, and calculates the error signal. This error signal is processed by a loop filter, which stabilizes the loop via implementation of Proportional-Integral-Derivative (PID) algorithm. This simple architecture is demonstrated in Fig. 6.3B.

The primary advantage of the PLL is its dynamic range compared to the open-loop method. Because the PLL actively follows the resonance peak, it is not constrained by the resonance linewidth. It can accurately track large and slow frequency drifts, such as those caused by temperature fluctuations or, more critically for us, by mass absorption events in sensing applications. A potential disadvantage of the PLL is that PID controller is an another dynamic system that can influence the intrinsic frequency noise of the resonator. As the drive frequency is continuously changed by the controller, it is important that phase continuity is achieved during these frequency variations. Otherwise, this dynamical controller might result in inaccurate measurements of the phase noise. In a real system, the controller has a finite response time and internal electronic noise. This can prevent it from perfectly tracking very rapid frequency fluctuations and can add its own small timing errors to the drive signal, potentially distorting the measurement of the resonator's true noise.

In our experiments, we have implemented both open-loop and closed-loop frequency tracking methods for various applications. In Fig. 6.4 we present an example comparison of both methods implemented for the same resonator. In these measurements, a lock-in amplifier serves as an IQ detector, and its filter bandwidth (or time constant, TC) is a critical parameter. This setting controls the averaging time for data collection. A long time constant (low bandwidth) yields a smoother, less noisy signal by averaging out rapid fluctuations. However, this comes at the cost of ob-

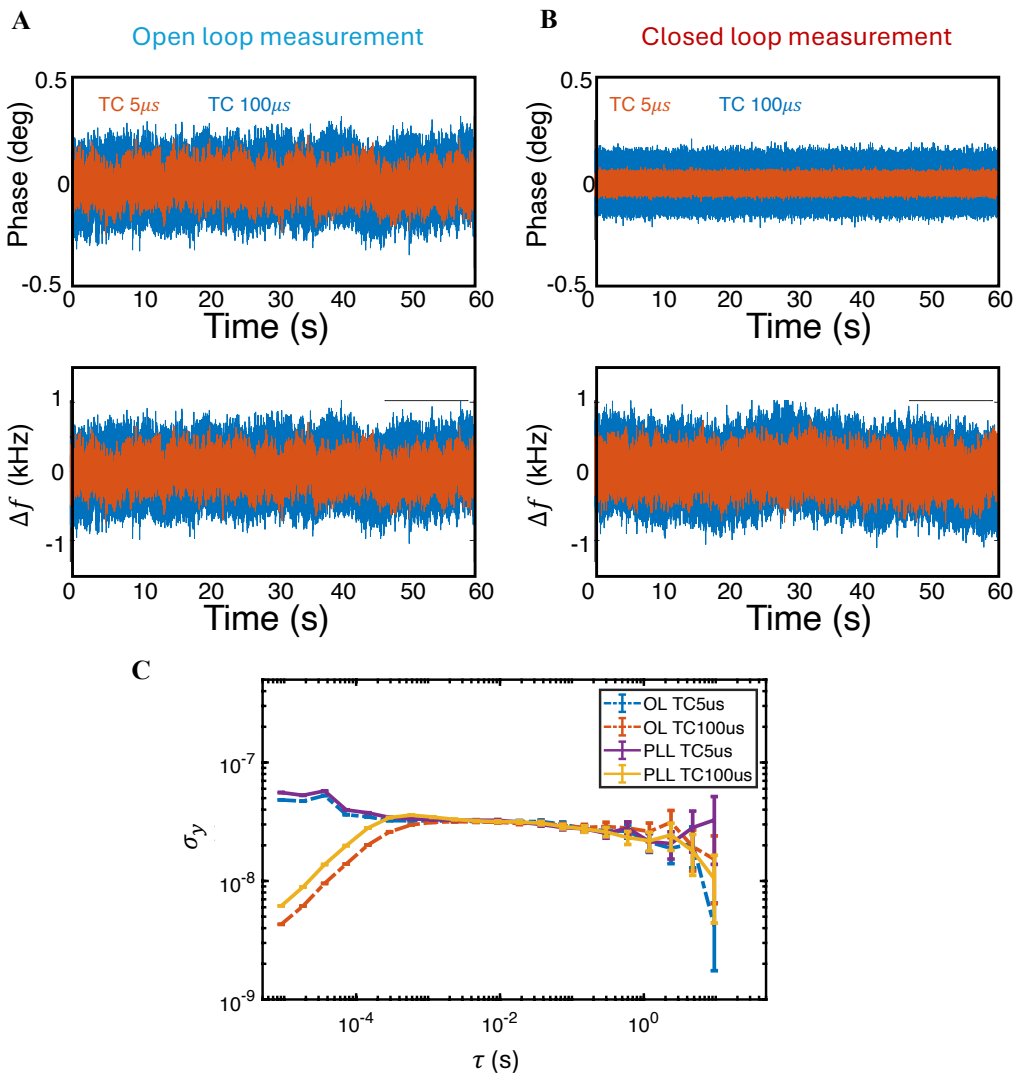

Figure 6.4: **Comparison of Open-loop and Phase-Locked Loop (PLL) Measurement. (A)** Time-domain data showing phase and the inferred frequency fluctuations in the open-loop configuration. **(B)** Time-domain data showing the phase locked on resonance near zero by the PLL and the frequency recorded by PLL. **(C)** The corresponding Allan deviation, σ_y, calculated for both methods using lock-in amplifier time constants (TC) of 5 μs and 100 μs. Both OL and PLL approaches yield nearly identical frequency stability results, while the choice of time constant significantly impacts the measured noise floor at short averaging times.

scuring the true high-frequency noise, an effect that manifests as an artificially low Allan deviation at short averaging times or a rolled-off PSD. As it can be seen from Fig. 6.4, PLL method keeps the phase values near 0, while in open loop measurement it is free to move. But the frequency fluctuations observed with both methods

result in similar Allan deviation as shown in Fig. 6.4C. The effect of the different measurement bandwidts are also demonstrated in Fig. 6.4C.

For low-temperature noise measurements, we primarily use the open-loop method. The goal of these experiments is to characterize the resonator's intrinsic noise limits with the highest possible fidelity. The open-loop approach is preffered here because it is a passive measurement that avoids introducing potential noise or artifacts from the active feedback electronics of a PLL. It is also suitable because we do not observe drift in frequency at these temperatures. This method provides a "purer" view of the device's fundamental performance.

For mass sensing experiments, we exclusively use PLL method. In sensing applications, the resonance frequency is expected to shift, often significantly, in response to an external stimulus (e.g., added mass). A PLL is essential because its feedback mechanism is designed to robustly follow these frequency shifts in real-time. An open-loop system, being fixed at one drive frequency, would quickly become detuned as the resonance peak moves, leading to a loss of signal and sensitivity.

6.1.2.3 Other Methods

While the open-loop method and PLL are the most common methods we have used within this work, we have also explored other measurement schematics.

A powerful technique for characterizing the noise in frequency domain is the direct measurement of its noise spectrum. In this open-loop configuration, the resonator is driven by a stable, low-noise signal generator at a fixed frequency near resonance. The output signal is then analyzed with a spectrum analyzer to measure the noise power in the sidebands that appear around the main drive frequency (the carrier). The result is the single-sideband (SSB) phase noise power spectral density. This method is ideal for revealing the fundamental noise floor of the measurement setup, as it has no active feedback that could introduce additional noise.

Another method we have begun to implement is the Pound-Drever-Hall (PDH) technique, adapted from laser technology. This method is similar to a PLL in that it is a closed-loop system, but it generates its error signal differently. The drive signal is phase-modulated to create sidebands, and by analyzing the signal reflected from the resonator, a highly sensitive error signal is produced. This is an area of ongoing work and further development and experiments are required.

6.2 Characterization of Frequency Noise in LN PnC Resonators

This section characterizes the frequency noise of the Lithium Niobate (LN) Phononic Crystal (PnC) resonator introduced in Fig. 5.1. The primary goal is to identify the fundamental noise sources and optimize the device's performance for high-sensitivity NEMS mass sensing. To achieve this, we systematically measure the resonator's frequency fluctuations under various experimental conditions, focusing on the effects of input power and operating temperature. A key objective is to understand the dominant noise mechanisms at cryogenic temperatures, which is essential for pushing the device toward its ultimate quantum limits.

The properties of the resonator are determined by measuring the reflection coefficient, S_{11} with the measurement setup we have demonstrated in Fig. B.1. The main difference in these measurements from the strong coupling measurements in the previous chapter is that here we will work in high phonon number regime with high drive powers where usually better noise performance is observed due to higher SNR. Figure 6.5 shows a typical resonance measured at 10 mK. The sharp dip in magnitude and corresponding phase response (Fig. 6.5A) translate to the circular trajectory on the IQ plane (Fig. 6.5B). A fit to this data allows for the extraction of the resonator's essential parameters: its resonance frequency (f_0), and its internal (κ_i) and external (κ_e) dissipation rates.

With the basic resonance established, we turn our attention to the resonator's frequency stability. To measure this, we park a drive tone to a frequency on resonance and record the fluctuations in the reflected signal over time (Fig. 6.6A). These fluctuations appear as a noise cloud on the IQ plane (Fig. 6.6B). By converting the phase noise into fractional frequency fluctuations, $y(t) = \delta f(t)/f_0$, we analyze the resonator's stability using two standard metrics: the PSD method, $S_y(f)$, (Fig. 6.6C), and the Allan deviation, $\sigma_y(\tau)$, (Fig. 6.6D).

A critical aspect of any cryogenic device is its performance as a function of temperature. We investigate the frequency noise dependence of our NEMS resonator from 10 mK up to 800 mK. We use a fixed input drive power and apply the methodology we built earlier and collect time series data at different stage temperatures. The results detailed in Fig. 6.7 reveal a counter-intuitive trend: the frequency noise systematically increases as the temperature is lower. This behavior is observed in both the PSD (Fig. 6.7B) and Allan deviation (Fig. 6.7C) analysis. By plotting the minimum Allan deviation achieved at each temperature (Fig. 6.7D), we see the effect clearly that the instability at 10 mK is nearly an order of magnitude worse than that ob-

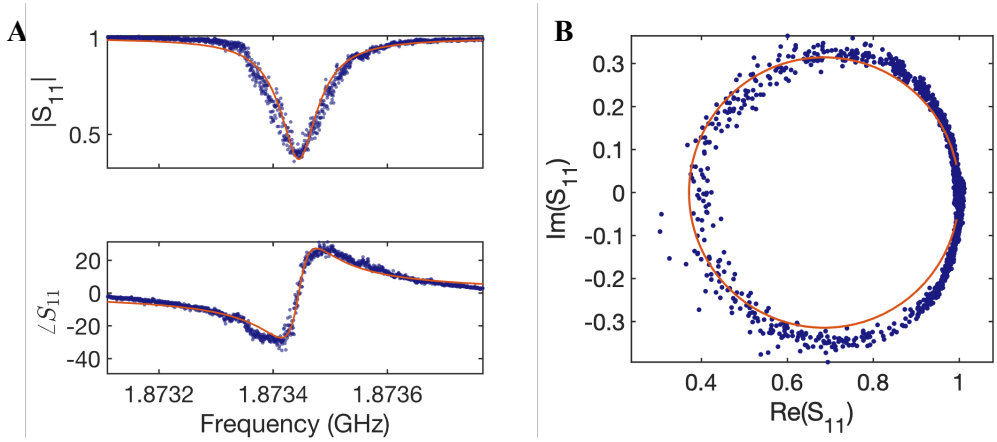

Figure 6.5: **Resonator Reflection Measurement.** Characterization of a microwave resonator at a temperature of 10 mK, showing the complex reflection coefficient (S_{11}). **(A)** The magnitude (top) and phase (bottom) of S_{11} are plotted as a function of frequency, revealing the resonance response of the resonator at approximately 1.8734 GHz. **(B)** The same measurement data is shown in the complex IQ plane, where the resonance forms a characteristic circular trajectory. For both panels, the scattered blue points represent the experimental data, while the solid red line indicates the best fit to a resonator model.

served around 1 K. This outcome is unexpected at first since the conventional noise sources, such as thermomechanical fluctuations and absorption-desorption noise, are expected to "freeze out" and diminish at such low temperatures. The emergence of this excess noise, therefore, strongly suggests that a different, non-standard noise mechanism is at play and becoming dominant in the millikelvin regime, possibly the TLS defects.

Beyond temperature, the input drive power is another tunable parameter. While higher power can improve the measurement's signal-to-noise ratio, it can also introduce nonlinear effects. In the measurements we perform at 10 mK, demonstrated in Fig. 6.8, while we observe improvement in the frequency noise at higher input powers, the overall noise still remains higher than room temperature. This indicates that the fluctuations are most likely due to far-resonance TLS interactions. We have observed in the previous chapter that on-resonance TLS saturates with high drive power, however, off-resonance TLSs are rather unaffected by this pump power.

To investigate this behavior further, we analyzed the resonator's internal κ_i and external κ_e dissipation rates which are extracted from resonance fits at various powers and temperatures (Fig. 6.9).The external dissipation remains stable across all conditions. This is expected, as κ_e is determined by the device's geometry and

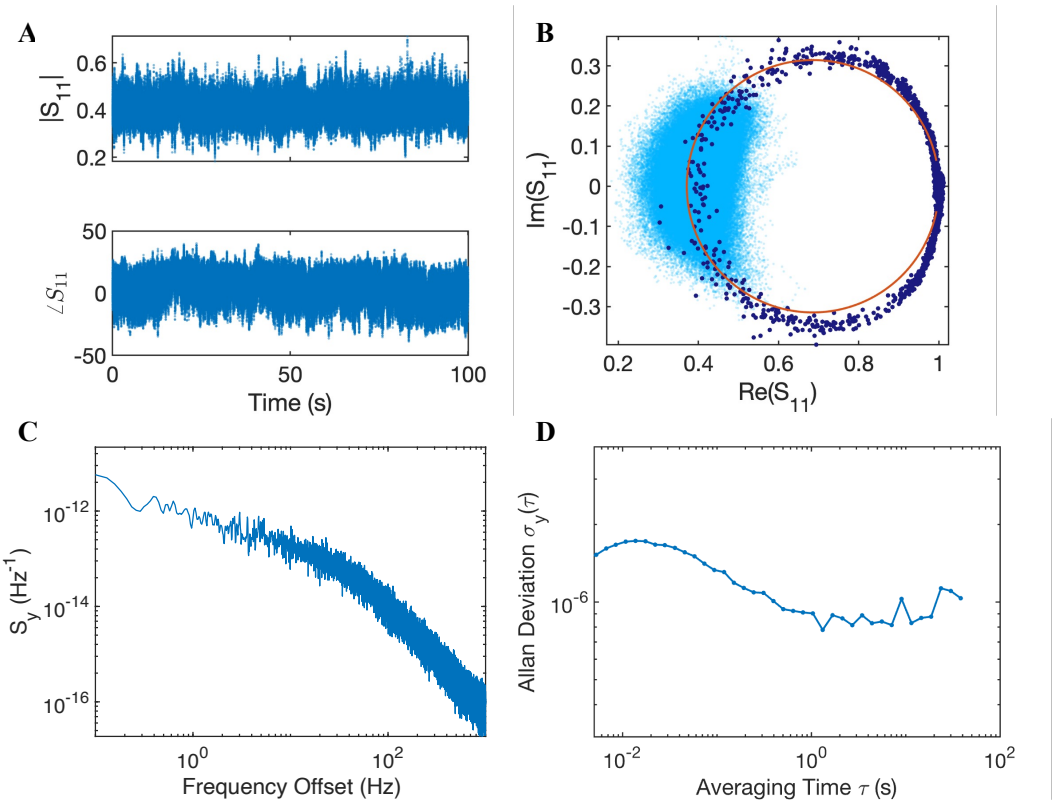

Figure 6.6: **Open-Loop Noise Characterization of LN Resonator.** The resonator is driven at its resonance frequency $\omega_d = \omega_m$ to measure its noise properties. (A) Time-domain data collected at a fixed drive showing fluctuations in the reflected signal's amplitude ($|S_{11}|$, top) and phase ($\angle S_{11}$, bottom). **(B)** The same noise data visualized on the complex IQ plane, showing the distribution of points around the driven point on the resonance circle. **(C)** The single-sided power spectral density (PSD) of the fractional frequency noise ($S_y(f)$), calculated from the noise data. **(D)** The corresponding Allan deviation ($\sigma_y(\tau)$) quantifies the resonator's frequency stability as a function of averaging time τ.

the material's intrinsic piezoelectric coupling. The internal dissipation, however, shows a distinct trend: it increases at low temperatures and low powers. This power-dependent reduction in internal loss is interpreted as a classic signature of TLS defects. At high drive powers, TLS become saturated and can no longer effectively dissipate energy, leading to a lower dissipation rates. However, in the presence of strong frequency noise, a phenomenon known as spectral diffusion can artificially broaden the measured resonance line shape. This can lead to an overestimation of the true dissipation rates. We must consider this effect carefully, as we will explore in the next section.

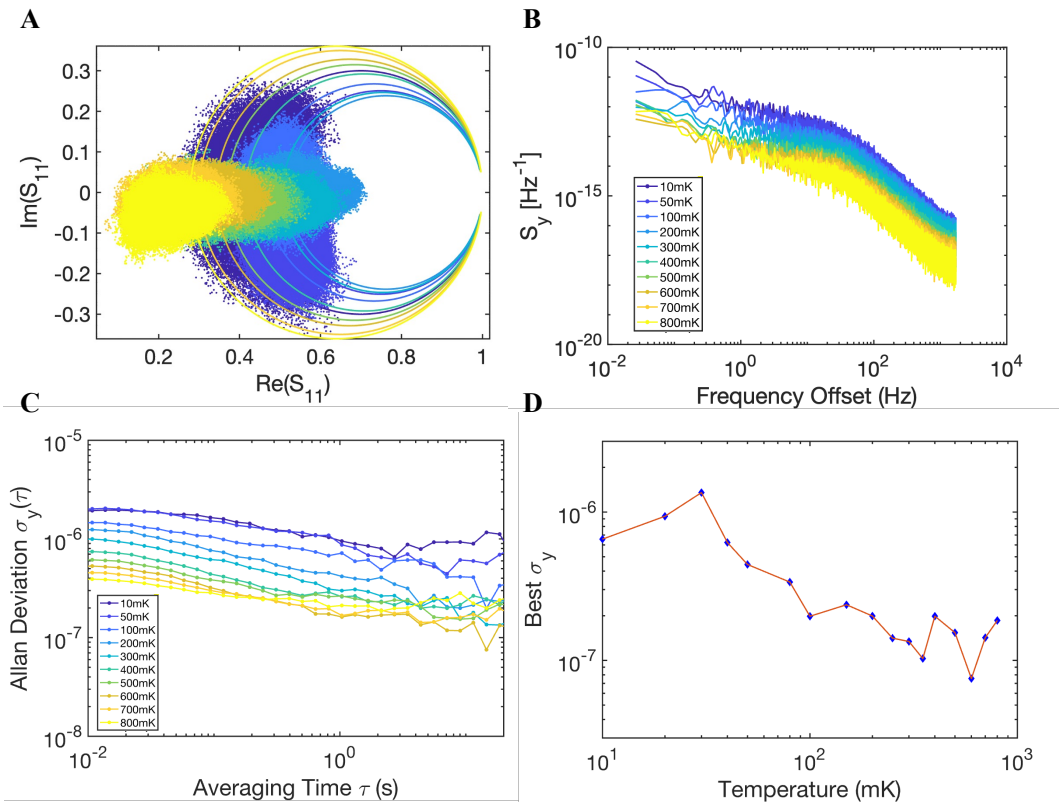

Figure 6.7: **Temperature Dependence of Frequency Noise.** Noise measurements were performed across a range of temperatures from 10 mK to 800 mK to characterize the impact on frequency stability. **(A)** Open-loop noise data on the IQ plane, where the color, from blue to yellow, indicates increasing temperature. The noise cloud visibly expands as the temperature decreases. **(B)** Power spectral density (PSD) of fractional frequency noise, $S_y(f)$, showing a clear increase in the noise with decreasing temperature. **(C)** Allan deviation, $\sigma_y(\tau)$, for each temperature, illustrating the frequency stability over different averaging times. **(D)** The optimal frequency stability, determined by the minimum of each Allan deviation curve from panel **(C)**, is plotted as a function of temperature.

In the next analysis, we model the temperature-dependent noise data with a power-law relationship (Fig. 6.10). This analysis shows that the low-frequency PSD scales as $S_y \propto T^{-1.10}$, while the best Allan deviation scales as $\sigma_y \propto T^{-0.54}$. These exponents provide quantitative benchmarks consistent with theoretical models of TLS-induced noise [99], reinforcing our physical picture.

While we have presented the measurements done from a single resonator here, we have performed measurements with various resonators and observed the similar frequency noise trend. In Fig. 6.11, we demonstrate another example of noise measurement as a function of temperature taken with a device with much higher

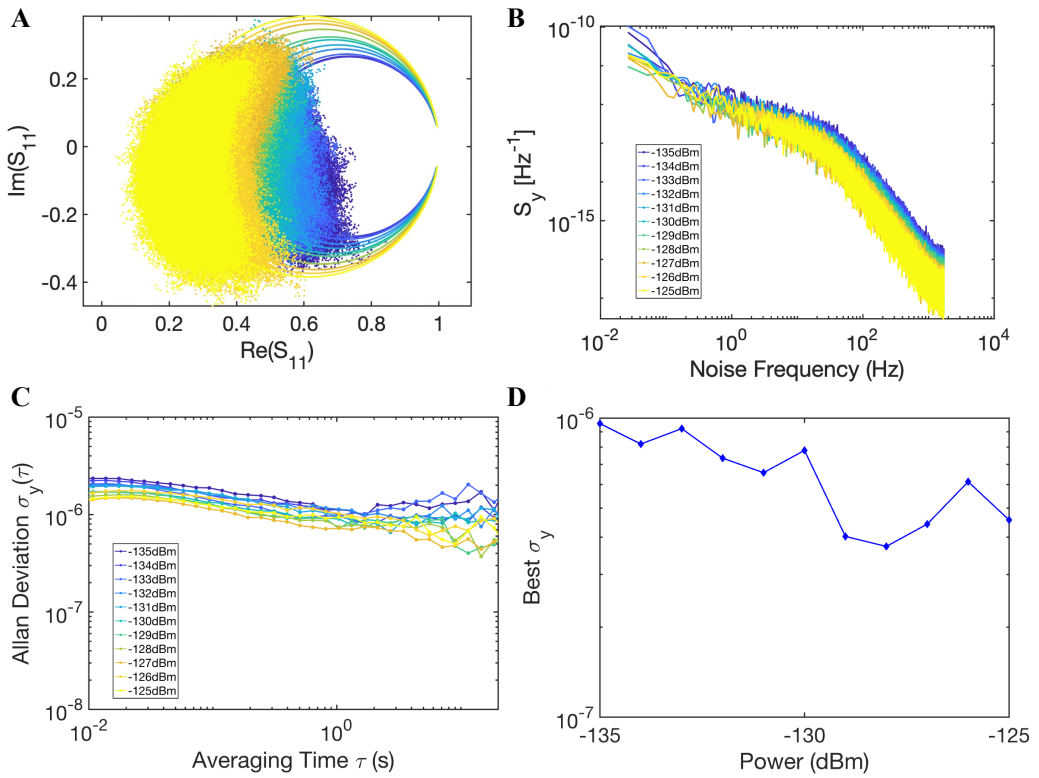

Figure 6.8: **Power Dependence of Frequency Noise.** The resonator's frequency noise was characterized while sweeping the input drive power from -135 dBm to -125 dBm. **(A)** Open-loop noise data on the IQ plane, where color indicates the drive power, from low (blue) to high (yellow). **(B)** Power spectral density (PSD) of the fractional frequency noise, $S_y(f)$, for each power level. **(C)** The corresponding Allan deviation, $\sigma_y(\tau)$, versus averaging time. **(D)** The optimal frequency stability, determined by the minimum of each Allan deviation curve from panel **(C)**, is plotted as a function of input power.

electromechanical coupling ($\kappa_e \approx 100$ kHz). This has allowed us to perform measurements with higher measurement bandwidth to capture fast time scale fluctuations. The PSD analysis of this device reveals a key feature at low temperatures as the emergence of random telegraph signal noise observed identified by a characteristic "knee" in the spectrum, followed by $\sim 1/f^2$ roll-off at high frequency offset. Such distinct noise signature at low temperatures widely interpreted as the action of fast-fluctuating TLS defects. This observation provides further evidence that TLS are the dominant noise source in the millikelvin regime.

Since the ultimate goal in this section is to optimize our LN PnC resonator for mass sensing, we convert the frequency stability data into mass resolution using the formulation described previously. Plotting this final performance metric across

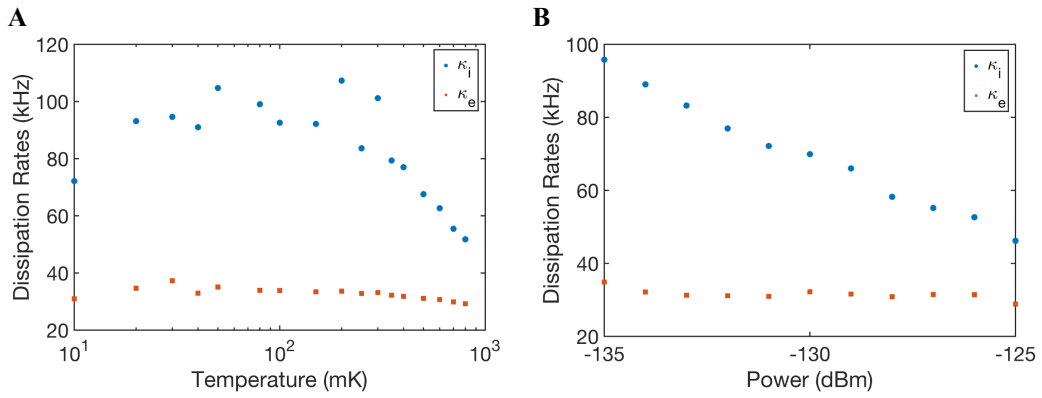

Figure 6.9: **Dissipation Rates at Varying Power and Temperature.** The internal (κ_i) and external (κ_e) dissipation rates extracted from fits to the reflection measurements. **(A)** Temperature Dependence: The dissipation rates are plotted as a function of temperature. The external coupling rate, κ_e (orange squares), remains nearly constant, while the internal loss rate, κ_i (blue dots), exhibits a non-monotonic dependence. **(B)** Power Dependence: The dissipation rates are plotted as a function of input power. While κ_e is independent of power, κ_i decreases significantly as power increases, a behavior characteristic of loss arising from saturable two-level systems (TLS).

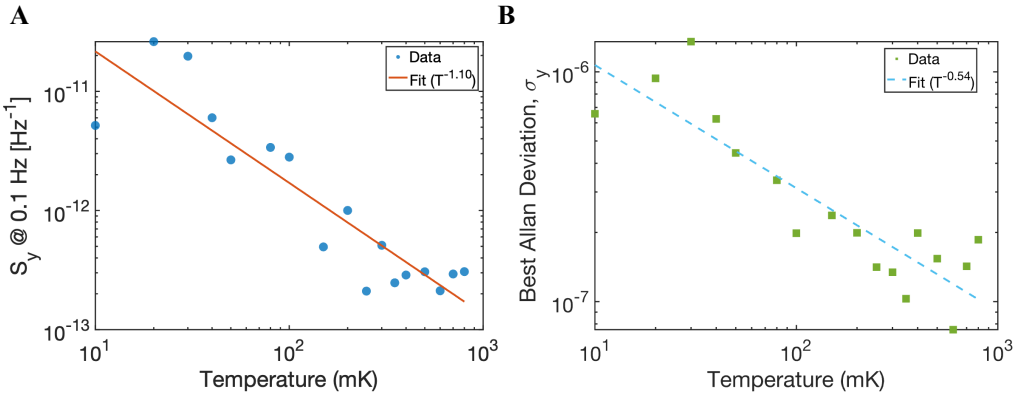

Figure 6.10: **Power-Law Temperature Dependence of Frequency Noise.** A quantitative analysis of the resonator's frequency noise as a function of temperature, with the data fitted to a power-law model to extract the scaling exponent. **(A)** The power spectral density (PSD) of fractional frequency noise, S_y, taken at a low-frequency offset of 0.1 Hz. The data (blue dots) is well-described by a power-law fit (red line) showing a dependence of $S_y \propto T^{-1.10}$. **(B)** The best (minimum) Allan deviation, σ_y, as a function of temperature. The fit (dashed blue line) indicates that the frequency stability improves with a scaling of approximately $\sigma_y \propto T^{-0.54}$.

the full temperature range (Fig. 6.12) reveals the optimal operating temperature window. The best mass resolution of 10–20 kDa is achieved not at the lowest

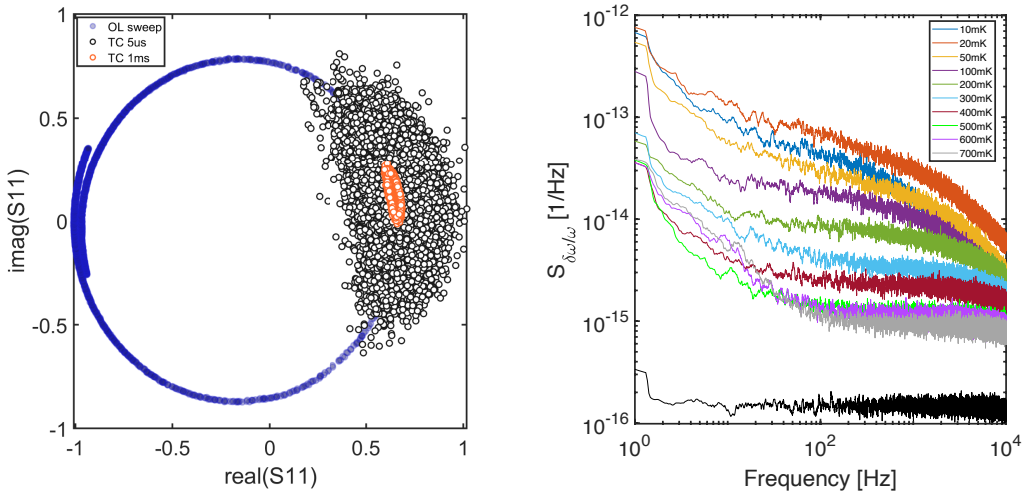

Figure 6.11: **Temperature Dependence of Frequency Boise in Another LN Resonator.** **(A)** IQ plane representation showing the resonator's response. The blue data shows a clean resonance circle from a frequency sweep. The noise clouds are measurements taken on resonance, illustrating how a short time constant (TC = 5 μs) captures significant fluctuations, while a long time constant (TC = 1 ms) averages them out. **(B)** PSD of the fractional frequency noise measured at various temperatures from 10 mK to 700 mK. The data reveals the trend that the noise is highest at the lowest temperature and systematically decreases as the device warms up.

temperature, but within a range between 2 K and 30 K. This result is a crucial guide for future mass sensing experiments, proving that simply cooling a device to its limit is not the optimal strategy for achieving maximum sensitivity. The counter-intuitive degradation in performance below 2 K strongly suggests that TLS become the dominant source of frequency fluctuations at millikelvin temperatures. However, understanding how TLS can induce such excess noise needs further analysis. In the next section, we provide more insight on to the TLS-induced random telegraph noise and spectral diffusion.

6.3 Spectral Diffusion due to TLS Defects

The characterization of the frequency fluctuations in this section is performed by Matthew Maksymowych at Stanford and we have simultaneously observed the increasing noise behavior with decreasing temperature in our devices. Our collaborative work regarding the frequency fluctuations is presented in the manuscript [128]. While the characterization in the previous section was performed with the same LN devices with resonance frequency around 2 GHz, in this work another device

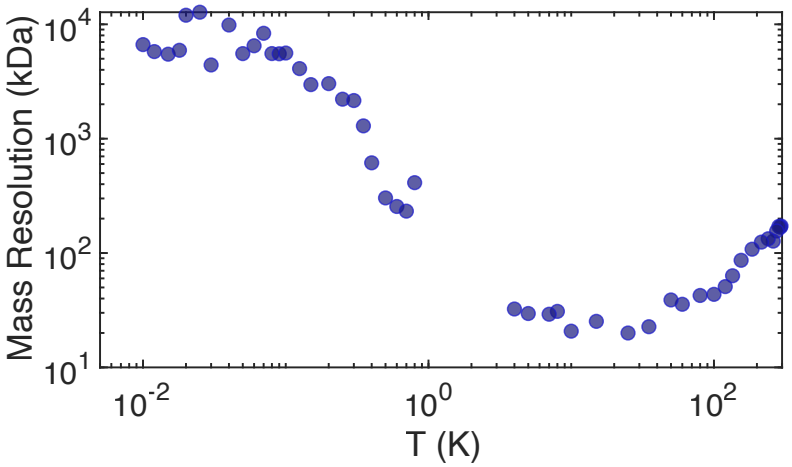

Figure 6.12: **Temperature Dependence of Mass Resolution.** The resonator's mass resolution, in kilodaltons (kDa), is calculated from its measured frequency noise and plotted over a wide temperature range from 10 mK to room temperature. The resolution exhibits a strong, non-monotonic dependence on temperature. It improves significantly as the device is cooled from room temperature, reaching an optimal value of approximately 20-30 kDa in the temperature range of 2-30 K. Below this optimal range, at cryogenic temperatures below 1 K, the resolution degrades substantially. This characterization identifies an ideal operating temperature window for high-sensitivity mass spectrometry experiments.

with the resonance frequency of 750MHZ is used. Advantage of this device is that with the achievement of high SNR and electromechanical coupling, it was possible to perform a lot shorter integration time measurements, in the order of μs. This allowed us to characterize and observe the fast fluctuations in the frequency noise.

The device, shown in Fig. 6.13(a-c), is fabricated from a 250 nm thick X-cut LN wafer and features an array of 31 resonators with frequencies spanning 450 MHz to 1 GHz. Characterization was performed using an open-loop microwave reflectometry measurement. Unlike the lock-in based setup described previously, this measurement uses a vector network analyzer (VNA) to measure the complex reflection coefficient, S_{11}. The data is obtained by open-loop method, an input transmission line power P at the PCR drives the mode into a coherent state and we obtain samples of S_{11} with an integration time of 10 ms at drive frequencies ω near resonance. Next, we take 100,000 samples of S_{11} with an integration time of 20 μs at fixed on- and off-resonance detunings, plotted as blue and orange dots, respectively. We attribute the spread in the samples of S_{11} taken with the off-resonant drive to detection noise. For clarity, we shift this data to the right side of the locus corresponding to small Δ

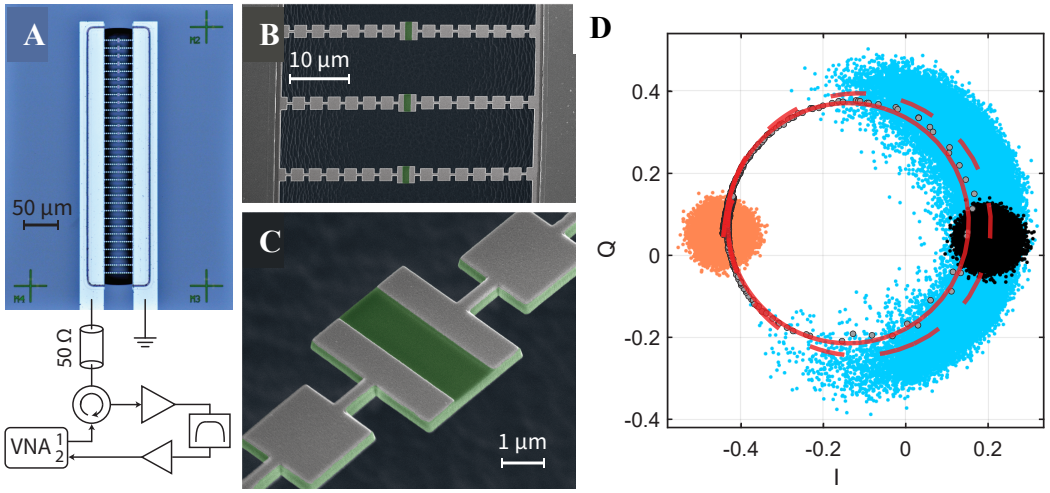

Figure 6.13: **Stanford Device. (A)** Optical microscope image of a phononic crystal resonator array with aluminum contact pads connected to a 50 Ω transmission line and a vector network analyzer (VNA) via a cryogenic circulator. **(B)** Colorized scanning electron micrograph (SEM) of frequency multiplexed resonators (Green: $LiNbO_3$, Grey: Al). **(C)** A 45 degree colorized SEM of a single resonator. **(D)** An IQ space plot of S_{11} data sampled at different drive frequencies (grey dots) near a 751 MHz mode at 10 mK and fitted to resonance circle (solid red line) assuming no fluctuations. The S_{11} fluctuations acquired off-resonance (orange), on-resonance (blue), and the inferred on-resonance detection noise (black) are shown. The resonator locus with the dephasing-corrected relaxation rate κ_i' is shown as a red dashed line.

(black dots) to more easily compare it to the samples from on-resonant driving. This makes it clear that the on-resonance noise is significantly larger, with fluctuations occurring primarily tangent to the resonance circle, a characteristic signature of frequency noise.

The locus obtained from a drive frequency sweep (Fig. 6.13D; solid red) consistently has smaller diameter than the locus that the S_{11} fluctuations (blue) appear to follow. This arises because the integration time of the drive frequency sweep (10 ms) is larger than the characteristic timescale of the frequency fluctuations. The solid red locus can therefore be thought of as an average over many loci with slightly different resonant frequencies. From the averaged locus we would infer a linewidth κ_i larger than the true intrinsic linewidth κ_i', leading to a smaller locus diameter. The samples (blue points) are acquired with a fixed frequency tone and a shorter integration time which leads to less averaging. We therefore use this data to infer κ_i' and the spectral linewidth broadening $\kappa_\phi \equiv \kappa_i - \kappa_i' \geq 0$ due to frequency fluctuations.

Using the locus correction method (LCM) [129], we can infer to these values as $\kappa_\phi/2\pi \equiv (\kappa_i - \kappa_i')/2\pi \approx 1.1$ kHz and resize the locus (dashed red line in Fig. 6.13D for more accurate fit to the dissipation rates, $\kappa_i'/2\pi \approx 3.5$ kHz.

This measurement highlights a critical concept: a standard spectroscopic measurement can be misleading if its integration time is longer than the characteristic timescale of an underlying noise process. This is precisely the case for the low-temperature frequency noise in these devices. Fortunately, this noise-induced spectral broadening can be accurately measured and corrected with fast time-domain techniques, provided the device's intrinsic noise is greater than the detection noise floor.

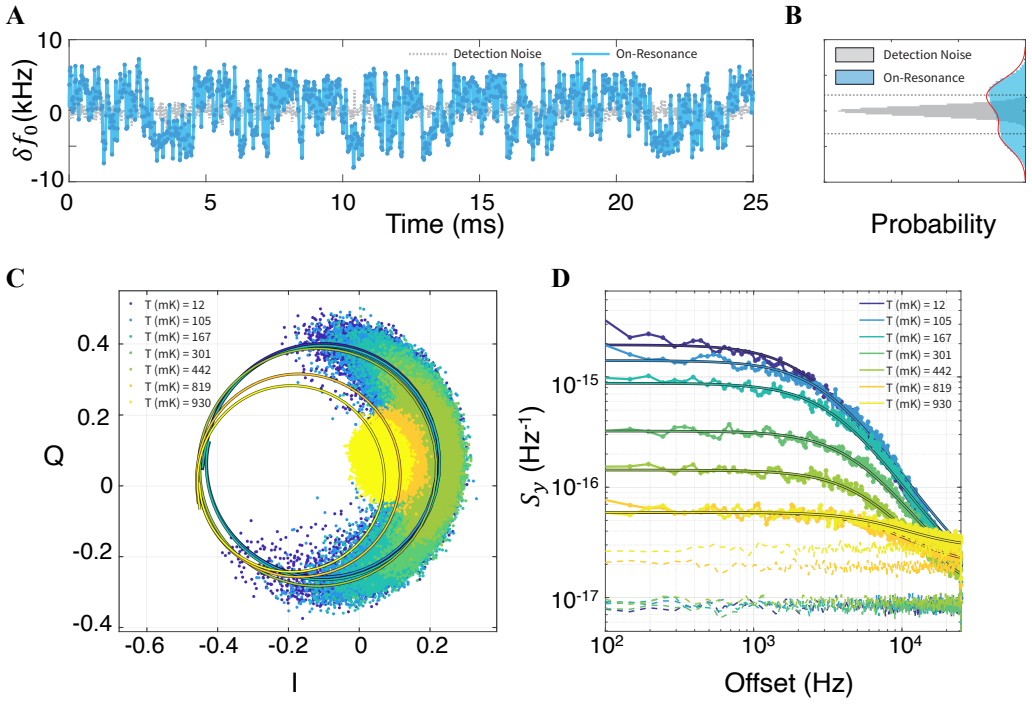

Figure 6.14: **Telegraph Frequency Jumps at Millikelvin Temperatures.** **(A)** The frequency fluctuations observed at Stanford while probed on resonance $\delta\omega_0(t)/2\pi$ (blue), and the associated detection noise (grey) versus time ($n \approx 5 \times 10^3, T \approx 50$ mK). The corresponding probability distributions are shown in **(B)**, where the on-resonance data is fitted to a two-mean Gaussian (red). **(C)** The raw $S_{11}(t)$ fluctuation data plotted at different temperatures with fixed $n \approx 1 \times 10^4$ for the resonator and the corresponding dephasing-corrected loci (lines). **(D)** The power spectral density (PSD) of the fractional frequency fluctuations $S_y(\nu)$ for the data in **(C)**.

Figure 6.14A demonstrates the frequency fluctuations $\delta\omega_0(t)$ inferred from on-resonance and the detection noise data as blue and grey, respectively. The on-resonance fluctuations are dominated by jumps between two frequency-distinct states, demonstrating a random telegraph signal (RTS). The probability distributions of the frequency are in Fig. 6.14B, where the on-resonance data is fit to a two-mean Gaussian function yielding a jump amplitude of $2 \times A/2\pi = 6.0 \pm 1.0$ kHz. To more thoroughly investigate the RTS, we repeat the measurements at different stage temperatures. Figure 6.14C depicts the on-resonance S_{11} fluctuations and LCM re-sized loci versus temperature measured with fixed $n \approx 1 \times 10^4$. The PSD of the fractional frequency fluctuations, $S_y(\nu)$, can be computed from the time series data, $y(t) = \delta\omega_0(t)/\bar{\omega}_0$, via the Welch method. The PSDs corresponding to the data in Fig. 6.14C are plotted in Fig. 6.14D and fit to a Lorentzian model (solid lines):

$$S_y(\nu) = \frac{\mathcal{A}^2}{2\Gamma} \frac{1}{1 + (\pi\nu/\Gamma)^2} + S_0(\nu) \tag{6.12}$$

which includes a frequency-independent detection noise contribution $S_0(\nu)$, shown as a dashed line for each temperature. The frequency fluctuations shown in Fig. 6.14 appear to decrease dramatically with temperature, showing more than 10 dB reduction from 10 mK to 1 K, with an apparent maximum stability between 1- K. This observation is consistent with what we have observed with different device covered in the previous section.

The observed switching behavior suggests a role for TLS in explaining the measured frequency noise [40, 116, 117]. Our experiments show consistent dependencies of frequency noise on temperature, mean phonon number, and band structure across multiple devices, and allow us to assess specific models of dephasing. They point to the role of a far-detuned TLS in generating the observed RTS noise. The persistence of frequency noise at high phonon numbers ($n \gg 100$), well above the saturation limit for resonant TLS [23] suggests that the responsible TLS are significantly detuned from the mechanical mode. This off-resonant configuration can explain why the switching characteristics remain stable even at high drive powers where resonant TLS effects are suppressed. In this far-detuned setting, the interaction between the mode and the TLS are governed by the dispersive Jaynes-Cummings Hamiltonian [13, 77, 130]:

$$\frac{H}{\hbar} = \left(\bar{\omega}_0 + \frac{g_x^2}{\Delta_{\epsilon,m}}\sigma_z\right)\left(a^\dagger a + \frac{1}{2}\right) + \frac{\omega_\epsilon}{2}\sigma_z \tag{6.13}$$

where $\Delta_{\epsilon,m} = \omega_\epsilon - \bar{\omega}_0$, ω_ϵ is the TLS frequency, σ_z is the TLS psuedo-spin operator, and a ($a^\dagger$) is the phonon annihilation (creation) operator. This model could by itself predict the switching behavior if thermal excitation of the TLS is sufficiently large, i.e., the TLS transition frequency is sufficiently small ($\hbar\omega_\epsilon \ll k_\mathrm{B}T$), to cause the TLS to spend roughly half its time in each state. Alternatively, strong coupling between a more nearly resonant TLS primarily in its ground state and a much lower frequency two-level fluctuator (TLF), can cause TLS frequency to fluctuate and lead to mechanical frequency noise. Our observations suggest a simpler scenario: a single far-detuned TLS strongly coupled to a TLF via $H_{\text{TLS-TLF}}/\hbar = (J_z/4)\sigma_z\sigma_z^{th}$, where σ_z^{th} is the thermal fluctuator spin operator. However, further experiments are needed to understand this mechanism fully.

6.4 Discussion

This chapter has presented a comprehensive investigation of the frequency noise characteristics of LN PnC resonators at millikelvin temperatures. The central finding of this work is the identification of an excess noise mechanism that emerges and dominates as temperatures are lowered below 1 K. This result is counterintuitive, as conventional thermomechanical noise sources are expected to be "frozen out" in this regime. Our measurements establish an optimal operating temperature for these resonators for frequency stability at approximately 4 K, below which the frequency noise starts to increase.

The experimental evidence strongly indicates that this low-temperature noise is attributable to the dynamics of intrinsic TLS defects within the device material. We have shown that the noise power spectrum and statistical behavior are consistent with a telegraph switching noise model, which reinforces the conclusion that discrete, thermally-activated fluctuators—a hallmark of TLS defects—are the dominant source of frequency instability.

The implications of this study are significant for the field of quantum acoustics and nanomechanics. It establishes that TLS-induced noise is a fundamental performance limitation for high Q resonators operating deep in the cryogenic regime. Therefore, achieving the ultimate coherence required for quantum sensing and information processing applications will necessitate strategies to mitigate this noise source. Our work provides insights into the performance limits of nanomechanical devices and points to promising avenues toward noise mitigation for application in quantum science. In quantum information processing, the highly unequal rates for decay

and dephasing that we have measured suggest that future work on error correction and dynamical decoupling taking into account the biased nature of the noise may be able to achieve improved performance. In the context of sensing, in particular mass spectrometry, for which these resonators are particularly well suited, our characterization of the frequency stability provides insights on what strategies may enhance mass resolution.

Chapter 7

NEMS MASS SENSING EXPERIMENTS AND TOWARDS QUANTUM SENSING

The main results of this thesis, presented in the previous chapters, have been improving our understanding of nanomechanical systems in quantum regime, while also bringing us closer to realization of NEMS sensing applications within quantum regime. The lithium niobate (LN) phononic crystal (PnC) resonators central to this work are especially promising for such applications due to their performances in quantum regime. As these resonators have been proven itself extraordinarily efficient tool as "macroscopic probes to listen the microscopic defects," analogously they can as well be utilized for "listening molecules." This application holds a great potential particularly in proteomics to identify as yet undiscovered elements with the proteome [131] and understand the structures and their functioning mechanisms. NEMS in quantum regime and integration of protein delivery system together, this approach can provide molecular fingerprints that identify individual, intact proteins and protein complexes, one-by one, with high throughput—and, thereby, can permit mapping the proteome.

While there are still many challenges to perform NEMS-MS sensing experiments in quantum regime, for example, having a platform that is capable of delivering proteins into a dilution refrigerator while attaining the base temperature, our initial efforts and preliminary results presented in this chapter aims to contribute to the future efforts.

7.1 Orbitrap - NEMS Hybrid Mass Spectrometer

Our initial mass sensing experiments are performed in a hybrid mass spectrometer (Fig. 7.1) that combines two distinct mass spectrometers : orbitrap mass analyzer and NEMS resonator [132]. The Orbitrap, produced by Thermo Fisher Scientific, provides high-resolution analysis of the mass-to-charge ratio (m/z) for large ensembles of ions. In contrast, the NEMS mass spectrometer operates at the single-molecule level, providing a direct measurement of mass for individual particles, such as small proteins.

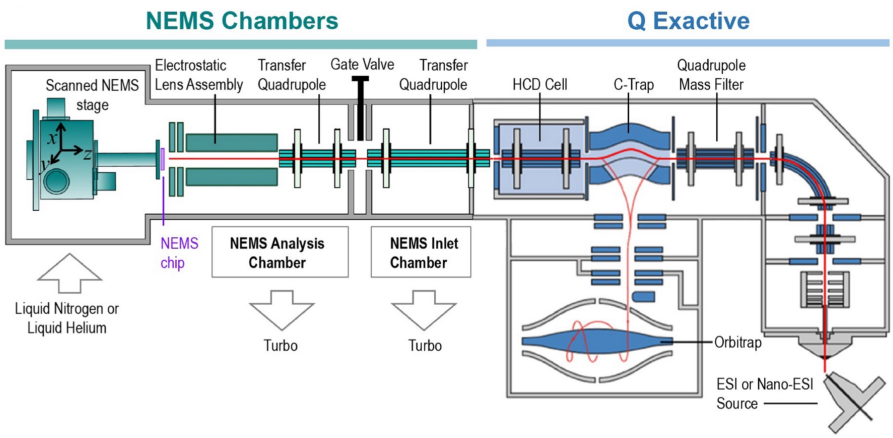

Figure 7.1: **Hybrid Orbitrap-NEMS Mass Spectrometer [133].** The architecture of a hybrid instrument that combines a commercial Q-Exactive Orbitrap mass spectrometer with a custom-built NEMS mass analyzer for the analysis of intact proteins and complexes. Delivery to the NEMS is accomplished with the additional vacuum chambers with transfer quadrupoles and ion lenses for single-molecule mass analyssis. NEMS chamber can be cooled with a cold finger cryostat.

The operation of this hybrid system can briefly be explained as follows. The experimental process begins with the introduction of the protein sample, which is held in a solution within an electrospray ionization (ESI) emitter tip. The application of a high voltage to this tip initiates the spray of droplets. As the solvent evaporates, the individual charged proteins are formed. These ions are then guided through a series of ion guides and filters. These stages use carefully controlled electromagnetic fields to collimate the ion beam and filter out undesired neutral species or contaminants, which is crucial for maximizing the signal-to-noise ratio in the subsequent detection stages. Ionized proteins then enters the Orbitrap mass analyzer. Here, ions are trapped in an electrostatic field and induced into stable trajectories where their frequency of axial oscillation is inversely proportional to the square root of their mass-to-charge ratio (m/z). The collective motion of the trapped ion packet induces a faint image current on a set of detector plates. A Fourier Transform (FT) of this time-domain signal yields a frequency spectrum, which is then converted into a high-resolution m/z spectrum.

After orbitrap, ion population is guided via a transfer quadrupole into the separate NEMS chamber, where the second mass spectrometry takes place with a NEMS resonator under ultra-high vacuum. This final NEMS stage is cryogenically cooled using the continuous flow cryostat described in Chapter 4. For the experiments we

performed, liquid nitrogen is used to reach a base temperature of 77 K, while liquid helium allows for cooling to approximately 13 K, with the temperature limited by the persistent thermal load of the experimental setup.

7.2 NEMS-MS with Silicon Doubly-Clamped Beam Resonators

The first-generation NEMS devices tested in our hybrid system are doubly-clamped beam resonators fabricated from silicon. Silicon is one of the most used materials for these resonators, due to its general accepted use in standard nanofabrication processes, relatively low mass, and suitability for various actuation and detection schemes. While carbon nanotube resonators can achieve single-Dalton resolution [134], such 1D nanostructures have a very small cross-section. This limits their practical use for analyzing intact macromolecules like proteins and viruses, which are often several nanometers in size. Pushing the limits of sensitivity with beam and membrane like devices is a more practical path towards achieving fully scalable NEMS-MS systems that can be used for intact molecular analysis. Therefore, advancing NEMS technology with beam and membrane-like geometries represents a more practical path toward creating scalable mass spectrometry systems for analyzing large, intact molecules. Specifically, the doubly-clamped beam is highly effective because its vibrational mode shapes are well-defined, which is crucial for accurately determining both the mass and landing position of an analyte.

7.2.1 Device Characterization

Devices are fabricated starting with silicon-on-insulator wafers, where the top, heavily doped p-type silicon (10^{20}cm^3) is thinned down to 50 nm. Contact to the silicon is made using standard electron beam lithography (EBL) and lift off gold contacts. This is followed by patterning ZEP resist with EBL to be used as a mask for an anisotropic pseudo-Bosch silicon etch. Finally buffered HF is used to undercut the devices by removing the sacrificial oxide layer. During this release step, a photoresist mask is used to cover the metal contact from being exposed to HF. Exposing Au contacts to HF without protection leads to porous silicon formation at the metal-Si interface, degrading device performance. The process is concluded with critical point drying to prevent stiction of the suspended structure, followed by a gentle oxygen plasma ash to remove any residual resist.

For this device demonstrated in Fig. 7.2, we utilize side-gate electrostatic actuation and a piezoresistive strain nanogauge readout technique. For actuation, a drive voltage (V_g) is applied to a side-gate, generating a force (F_g) described by:

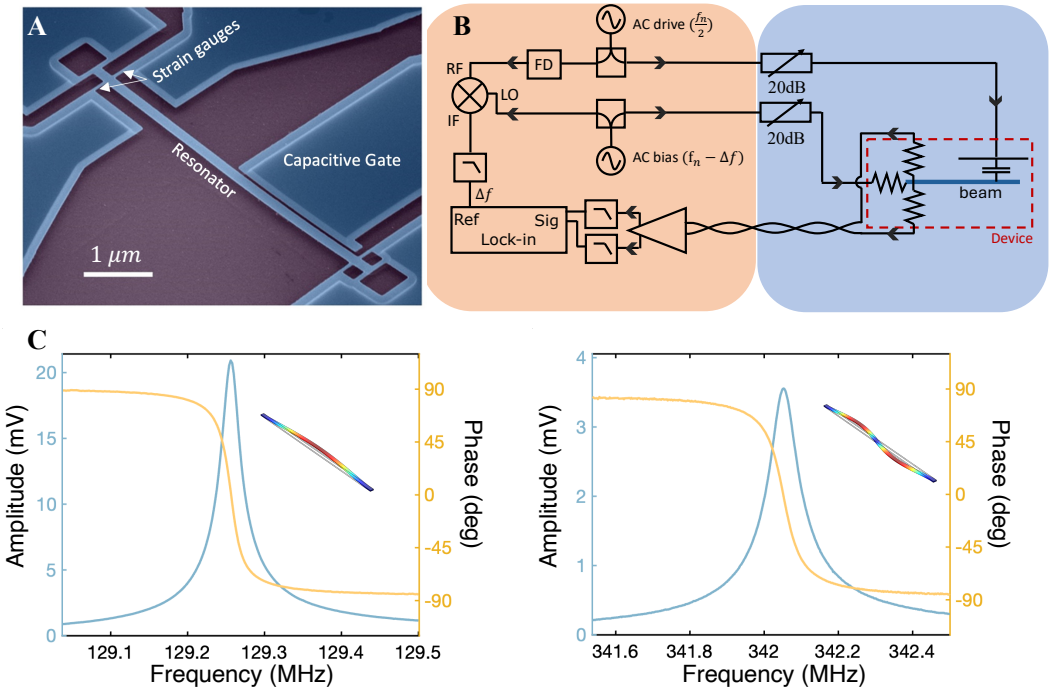

Figure 7.2: **Silicon Nanobeam Resonators and Measurement Setup.** **(A)** A scanning electron micrograph (SEM) of the doubly-clamped silicon nanobeam resonator. The image highlights the suspended beam, the side capacitive gate used for electrostatic actuation, and the piezoresistive strain gauges located at the high-strain clamping points. **(B)** Schematic of the electronic actuation and detection setup. The components in the orange box are at room temperature, while the device itself (blue) is cryogenically cooled. The setup shows the side-gate electrostatic actuation (drive at $f_m/2$) and the piezoresistive, downmixed readout scheme. **(C)** Measured frequency response of the fundamental (left, at 129.2 MHz) and second (right, at 342.0 MHz) in-plane modes of the resonator at approximately 80 K. The blue curve shows the amplitude, and the orange curve shows the phase. Insets display the simulated mode shape for each resonance.

$$F_g = \frac{1}{2}\frac{\partial C_g}{\partial x}V_g^2 \tag{7.1}$$

where $\frac{\partial C_g}{\partial x}$ is the gradient of the gate capacitance with respect to the beam's displacement. Since the force is proportional to V_g^2, applying an AC drive voltage at half the mechanical resonance frequency ($\omega_n/2$) produces a force component at ω_n that excites the vibrations of in-plane vibrations of mode n.

For the readout, the resistive change in the nanogauges placed at the high strain locations of the beam, which are close to the clamping points, is used to read the

mechanical vibrations. Two nanogauges placed symmetrically are exposed to strain due to the mechanical motion of the beam; as one experiences tensile strain, the other experiences compression. To briefly explain the idea behind piezoresistive detection, the resistance of a material with length L, cross-section A, and resistivity ρ can be written as:

$$R = \frac{\rho L}{A}. \tag{7.2}$$

A change in either the length or the resistivity of the material causes a change in the resistance. This strain-dependent change is a material property quantified by the Gauge Factor (GF), which relates the fractional change in resistance to the applied strain, ϵ:

$$\text{GF} = \frac{\Delta R/R_0}{\epsilon}. \tag{7.3}$$

While metals have a low Gauge Factor (typically 2) arising primarily from geometric changes, semiconductors like silicon have a much larger GF (often >100) due to the strong dependence of their resistivity on strain. In our resonator, when the nanobeam is vibrating at its resonance frequency, ω_n, the silicon nanogauges experience a high, oscillating strain. This dynamic strain induces a proportional resistance change. Therefore, the total resistance of the gauge becomes time-dependent, $R(t)$, and can be expressed as the sum of its static (or initial) resistance, R_0, and a dynamic component that oscillates in sync with the mechanical motion:

$$R(t) = R_0 + \Delta R \cos(\omega_n t + \phi) \tag{7.4}$$

where ΔR is the amplitude of the resistance change and ϕ is a phase factor.

The fabricated nanogauges have a typical resistance (R_0) of approximately 4 kΩ. To transduce the mechanical motion, this high-frequency resistance change must be converted into a measurable voltage or current. While applying a DC bias is straightforward method, it is ineffective for this application. The combination of the high device resistance and parasitic capacitances from wiring and circuitry creates a low-pass filter with cut-off frequency $\sim 1/\sqrt{RC}$ that attenuates the high-frequency (ω_n) signal, which carries the information about the mechanical resonance.

To overcome this challenge, we employ an electrical downmixing scheme [135], as shown in Fig. 7.2B. In this method, instead of a DC bias, we apply an AC bias

voltage at a frequency ω_c, which is intentionally set near the mechanical resonance frequency, typically with a small offset $\delta\omega$:

$$V_{\text{bias}}(t) = V_c \cos(\omega_c t) = V_c \cos((\omega_n + \delta\omega)t). \tag{7.5}$$

This carrier voltage multiplies with the time-varying resistance of the gauge, $R(t) = R_0 + \Delta R \cos(\omega_n t)$. The resulting output signal contains components at the sum and difference frequencies. The critical downmixed component appears at the low offset frequency $\delta\omega$:

$$V_{\text{out}} \propto \Delta R \cos(\delta\omega t). \tag{7.6}$$

This low-frequency signal, which now carries the amplitude and phase information of the high-frequency mechanical resonance, is well below the circuit's cutoff frequency and can be accurately measured with a lock-in amplifier. By employing two nanogauges that experience opposite strain (one in tension, one in compression), we implement a differential readout scheme with differential amplifier (Fig. 7.2B), which significantly increases the Signal-to-Noise Ratio (SNR). To further optimize the readout, an impedance matching circuit is often employed between the device and the amplifier. This circuit is crucial for maximizing signal power transfer by transforming the high output impedance of the nanogauges (several kΩ) to match the standard 50 Ω input impedance of the measurement electronics, thereby preventing significant signal reflection and loss.

Figure 7.2C demonstrates the measurements of a $4\ \mu m \times 150\ nm\ \times 50\ nm\ (L \times w \times t)$ taken with this method. The data was acquired under cryogenic conditions, with the device stage cooled to approximately 80 K using a continuous-flow liquid nitrogen cooling (as detailed in Chapter 4). For this device, the fundamental in-plane mode was measured at 129 MHz, and the second mode observed at 341 MHz, with the quality factors around 10000.

Before mass sensing experiments, we characterize the frequency stability of the resonators using the methods detailed in the previous chapter. Figure 7.3 plots the minimum Allan deviation as a function of temperature for two Si devices. Both devices exhibit a similar trend: the frequency stability improves by an order of magnitude as the temperature is reduced from room temperature down to approximately 70 K. However, no significant further improvement is observed when cooling from

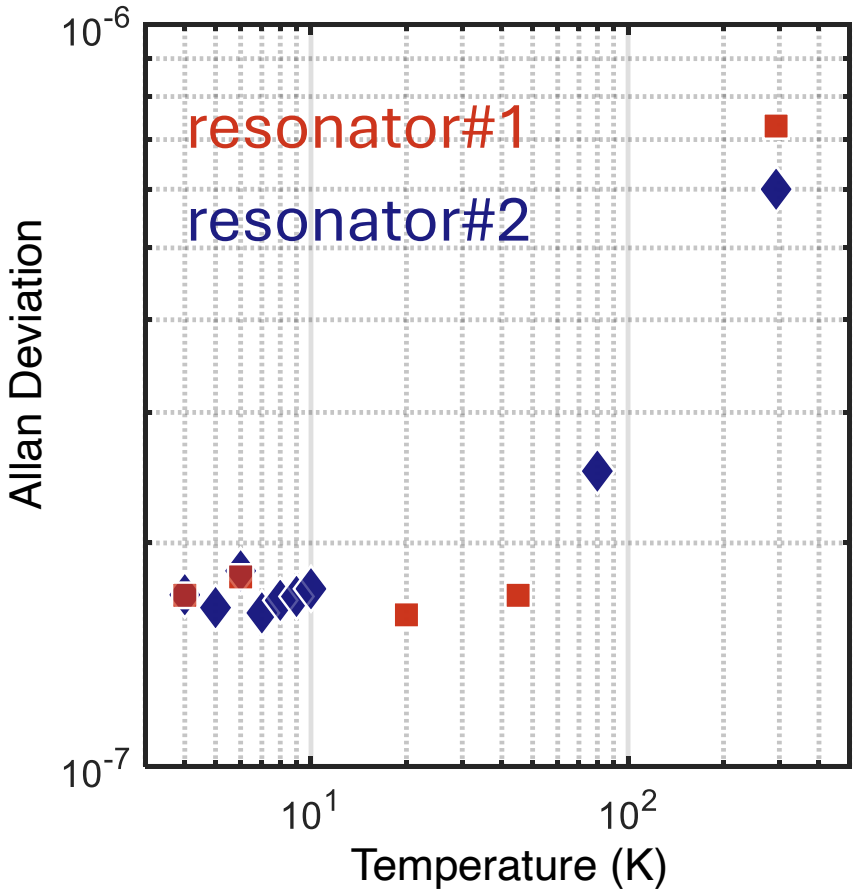

Figure 7.3: **Allan Deviation of Si NEMS.** Minimum Allan deviation plotted as a function of temperature for two different silicon nanobeam resonators. For both devices, the frequency stability improves significantly (Allan deviation decreases) as the temperature is reduced from room temperature, reaching an optimum value of $\sim 1 \times 10^{-7}$ around 70-80 K. No further improvement is observed at lower temperatures, indicating that liquid nitrogen cooling is sufficient for achieving the best performance.

70 K to 4 K with liquid helium. Consequently, liquid nitrogen temperatures ($\sim$ 77 K) were identified as the optimal regime for these experiments, offering the best balance of performance and practicality. At this operating temperature, the 4-μm-long beam achieves a minimum Allan deviation of approximately 1×10^{-7}, which corresponds to a mass resolution of about 10 kDa. However, during simultaneous two-mode PLL operation, the mass resolution is closer to 40 kDa due to additional input power and possibly increase in device temperature.

7.2.2 Hybrid Mass Sensing with Si Nanobeams

Mass sensing experiments were performed using two protein analytes: Immunoglobulin G (IgG), with a mass of 150 kDa, and Apoferritin, with a mass of approximately 480 kDa. These proteins are ideal candidates for initial characterization as they are intact and exhibit minimal variation in mass and conformation. Since these two proteins are in different size and mass, the ion optics and mass filtering settings of the hybrid mass spectrometer were adjusted for each species to ensure proper transfer. For the NEMS-MS experiments, the silicon chip was mounted in the NEMS chamber of the hybrid mass spectrometer and cooled to 77 K. This temperature not only helps reduce the frequency fluctuations, but also allow better absorption of analytes on the surface of the resonator compared to room temperature.

We simultaneously track the resonance frequencies of the two in-plane modes using phase-locked loops (PLLs). The adsorption of individual molecules onto the resonator surface is observed as discrete, downward jumps in resonance frequencies, with each jump corresponding to a single binding event. Long time-series data were collected in Fig. 7.4B, capturing approximately 600 individual binding events at an average rate of 0.5 particles per second.

The mass of each adsorbed particle (δm) and its landing position (a) are calculated from the simultaneous frequency jumps (δf_1 and δf_2) of the two tracked modes. For the simplicity, we model the adsorbed analyte as a point mass, where its contribution to the system's kinetic energy causes a shift in the resonance frequency. The frequency shift (δf_n) of a given mode n is related to the added mass (δm) and its landing position on the resonator (a) by:

$$\delta f_n = -\frac{f_n}{2M_{\text{eff}}}\delta m \cdot \phi_n(a)^2 \tag{7.7}$$

where f_n is the initial resonance frequency of mode n, M_{eff} is the effective mass of the mode, and $\phi_n(a)$ is the mode shape at the landing position, which describes the amplitude of the vibration at that point.

To solve for the two unknowns (mass and position), we use the data from two distinct modes. By taking the ratio of the frequency shifts from Equation 7.7 for two modes (n=1 and n=2), the unknown mass term Δm cancels out, leaving an expression that depends only on the landing position:

$$\frac{\delta f_1/f_1}{\delta f_2/f_2} = \frac{\phi_1(a)^2}{\phi_2(a)^2}. \tag{7.8}$$

Since the mode shapes $\phi_1(a)$ and $\phi_2(a)$ are known properties of the resonator, their ratio is uniquely determined by the position a. Therefore, by measuring the normalized frequency shifts, the landing position can be calculated. Once the position is known, it can be substituted back into Equation 7.7 for either mode to solve for the mass, δm.

The statistical uncertainty of the measurement, as characterized by the Allan deviation, is incorporated directly into the mass calculation for each mass absorption event. Rather than treating each pair of frequency jumps $(\Delta f_1, \Delta f_2)$ as a single, definite point, we model it as a Joint Probability Density Function (JPDF) [45]. This function describes the probability of observing a particular pair of frequency shifts, given the frequency noise.

Assuming the frequency noise in each mode follows a Gaussian distribution, this JPDF is a bivariate Gaussian centered on the true frequency shifts (μ_1, μ_2):

$$\text{JPDF}(\Delta f_1, \Delta f_2) = \frac{1}{2\pi\sigma_1\sigma_2\sqrt{1-\rho^2}} \exp\left(-\frac{z}{2(1-\rho^2)}\right) \tag{7.9}$$

where the exponent term z is given by:

$$z = \frac{(\Delta f_1 - \mu_1)^2}{\sigma_1^2} - \frac{2\rho(\Delta f_1 - \mu_1)(\Delta f_2 - \mu_2)}{\sigma_1\sigma_2} + \frac{(\Delta f_2 - \mu_2)^2}{\sigma_2^2}. \tag{7.10}$$

The parameter ρ is the correlation coefficient, which quantifies the statistical relationship between the noise in mode 1 and mode 2. The key parameters, σ_1 and σ_2, are the standard deviations of the frequency noise for mode 1 and mode 2, respectively. These values are directly determined from the Allan deviation measurements. Specifically, the minimum Allan deviation for each mode provides the value for σ, thus rigorously connecting the resonator's long-term stability to the uncertainty of a single absorption event. By using this JPDF, we transform each discrete measurement event into a statistical distribution that fully accounts for the measurement noise. Repeating this for each event and adding the distributions give the mass spectrum obtained by the NEMS device over many events. While we briefly described the analysis here, more details can be found in [45, 133].

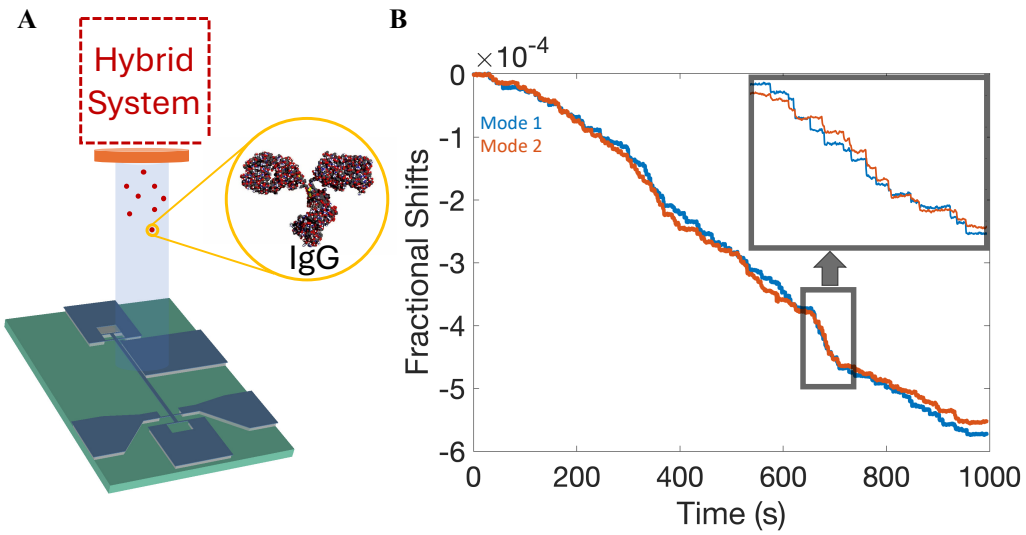

Figure 7.4: **NEMS-MS with Si NEMS. (A)** A schematic of the experimental setup. Molecules from the hybrid mass spectrometer system are deposited onto the surface of the silicon nanobeam resonator. The inset shows the molecular structure of IgG, one of the analytes used in this experiment. **(B)** A real-time plot of the fractional frequency shifts for two different resonant modes (Mode 1 in blue, Mode 2 in red) as proteins land on the device over time. The inset shows a magnified view of the data, where the discrete, step-like downward jumps caused by individual molecule absorption events are clearly visible.

The results from the mass sensing experiments with IgG and Apoferritin are presented in Fig. 7.5, which compares the mass spectra obtained from the Orbitrap mass analyzer with those from the NEMS-MS. For IgG, the Orbitrap mass-to-charge (m/z) spectrum (Fig. 7.5A, left) clearly resolves a series of charge states, with the highest abundance observed from +22 to +26. The mass calculated from these distinct charge states is 148 kDa, consistent with the expected mass of IgG. The corresponding NEMS-MS spectrum, constructed from 240 individual binding events (Fig. 7.5A, right), shows a distinct peak at 150 kDa, in excellent agreement with the conventional mass spectrometry measurement. In contrast, the Orbitrap m/z spectrum for Apoferritin (Fig. 7.5B, left) does not clearly resolve individual charge states. While a moving average filter applied to estimate a mass of 488 kDa from this complex spectrum, the result carries some ambiguity. The NEMS-MS, however, directly measures the mass of each individual molecule, bypassing the need for charge state deconvolution. The resulting NEMS-MS spectrum (Fig. 7.5B, right) unambiguously shows a clear peak at 480 kDa, demonstrating the advantage of direct mass measurement for large, complex analytes.

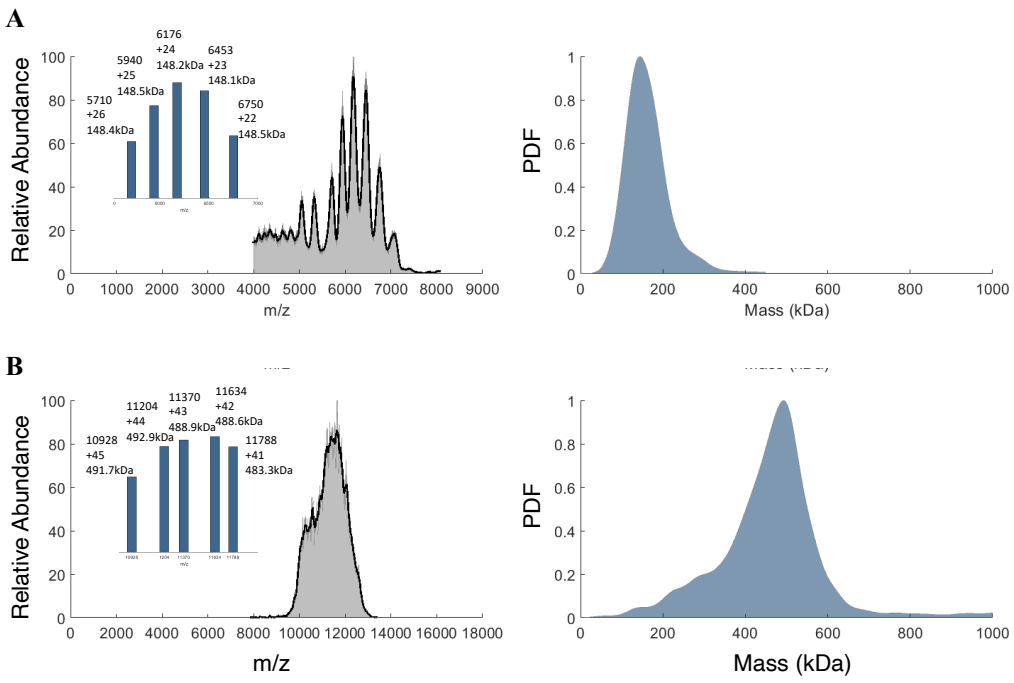

Figure 7.5: **Mass Spectrometry Results. (A)** Hybrid mass spectrometry for IgG. On the left mass to charge ratio obtained from the Orbitrap masss spectrometer in hybrid system. Individual charged states are demonstrated in the inset with the m/z values, charge, and the inferred mass from top to bottom. The spectra correctly estimates the mass of IgG. On the right, mass spectra obtained from 240 individual absorption events on Si NEMS resonator. **(B)** The mass spectra for Apoferritin. While the Orbitrap measurement is noisy, where individual charge states are not clearly resolved and it is hard to infer to mass. The NEMS-MS spectrum on the right, which directly measures the mass of individual molecules, showing a clear, unambiguous peak.

7.2.3 Conclusion

In summary, we have shown the successful implementation of a hybrid NEMS-mass spectrometry system for the analysis of intact proteins at the single-molecule level. Using silicon doubly-clamped beam resonators, we demonstrated direct mass measurements of IgG and Apoferritin, achieving results that are in excellent agreement with conventional mass spectrometry. The attainment of a mass resolution in the tens of kilodaltons represents a significant benchmark for this resonator design and piezoresistive transduction scheme.

However, these silicon resonators have fundamental limitations that hinder further improvements. Pushing for higher mass resolution by shrinking the resonator dimensions to increase the operating frequency presents multiple challenges. First,

piezoresistive readout becomes increasingly inefficient at very high frequencies due to parasitic capacitance and the reduced strain with the reduced mechanical displacements in the modes. Second, as the device becomes smaller, clamping losses and surface effects become more dominant, leading to a degradation of the mechanical quality factor Q, which is essential for high performance. More critically, the piezoresistive detection method is fundamentally incompatible with the ultimate goal of quantum-limited sensing. The method's reliance on applying a bias current across the nanogauge inevitably leads to Joule heating. This localized heat source raises the effective temperature of the resonator, causing thermal decoherence that prevents the device from being cooled to its quantum ground state. This makes it challenging to observe or manipulate the quantized energy states required for quantum-level measurements.

Therefore, while this work successfully validates the power of the hybrid spectrometer platform and demonstrates the benefits of single-molecule analysis, it also highlights the need for a new resonator paradigm to transcend these classical limits. To reach the quantum regime, we require a different type of resonator. As we have seen in this work, PnC resonators offer a compelling solution, providing an architecture specifically designed to overcome these challenges and enable the next generation of quantum NEMS mass sensing.

7.3 NEMS-MS in GHz Regime

To date, the majority of NEMS-MS experiments have been conducted using resonators in the shape of doubly-clamped beams or cantilevers, as we have covered one of the example in the previous section. This is advantageous because the mode shapes of these geometries are well-understood and for advanced NEMS-MS operation with multiple modes is highly desirable. Because each mode has a distinct spatial shape, and a single analyte landing on the device will shift each mode's frequency by a different amount depending on its position. However, operation of these NEMS devices is typically confined to resonance frequencies in the MHz range. Pushing NEMS-MS into the GHz regime is a first step towards quantum sensing to achieve low phonon number in the mechanical mode. Moreover, GHz resonators begin to approach the vibrational frequencies of molecules themselves (high-GHz to THz), which can open the possibility of not only weighing a molecule but also performing mechanical spectroscopy of its internal modes.

The LN PnC resonators utilized in the preceding chapters of this thesis were intentionally designed to isolate a single, high-quality mechanical mode. To realize the goal of multi-mode NEMS-MS, it is necessary to engineer a new generation of PnC devices supporting multiple mechanical modes. This engineering task has two important features. First, the frequency of each desired mode must be carefully placed within the crystal's acoustic bandgap to ensure high mechanical quality factors. Second, each mode must also exhibit strong piezoelectric coupling, which is essential for efficient actuation and detection, and for precisely tracking its resonance frequency. The solution to meeting these concurrent demands lies in the integrated design of the phononic crystal structure and the metal electrodes used for transduction.

7.3.1 Design of Multi-Mode LN PnC Resonator

The primary goal is to engineer a LN PnC resonator that supports multiple, distinct mechanical modes. To be effective for NEMS-MS, this design must satisfy two critical conditions simultaneously:

1. Transduction Efficiency: Each confined mode must also exhibit strong electromechanical coupling, allowing it to be efficiently actuated and detected piezoelectrically.

2. Acoustic Confinement: Each mode's frequency must be carefully positioned within a phononic bandgap to ensure the mechanical motion is tightly confined at the resonator, leading to a high quality factor.

Achieving this dual objective requires an integrated approach that addresses two interconnected challenges: the design of a multi-mode defect cell with optimized electrodes and the engineering of a phononic bandgap to provide acoustic isolation.

The geometry of a PnC resonator consists of two main parts: periodic unit cell –called the "mirror cell"–to produce a phononic bandgap at the desired GHz frequencies and the central "defect cell" which hosts the mechanical vibrations. The design is controlled by tuning their dimensional parameters, such as their width (w_d, w_m), height(h_d, h_m) of the cells, and and the size of the tether connecting them(w_t, h_t) along with their uniform thickness t. The placement of the electrodes on the defect cell, defined by the gap (w_g), is also a critical design parameter. These parameters are summarized in Fig. 7.7A.

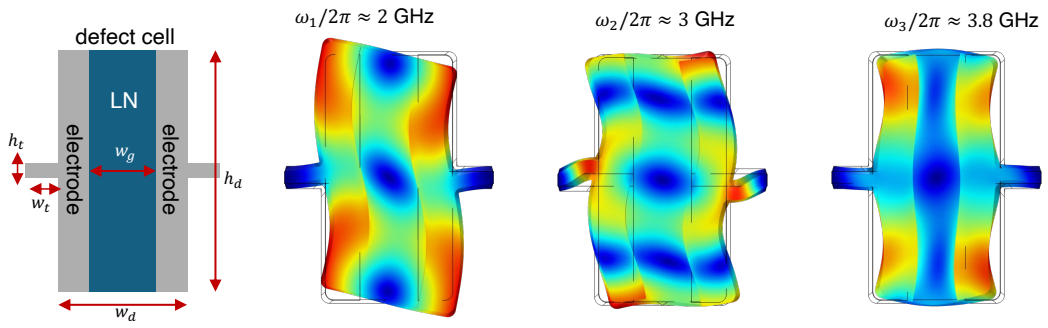

Figure 7.6: **Multimode LN NEMS Resonator Design for Mass Sensing.** Engineering a multi-mode Lithium Niobate (LN) NEMS resonator for advanced mass sensing applications. The design process involves tuning the defect cell geometry and electrode configuration (schematic, left) to optimize performance. Finite Element Method (FEM) eigenfrequency analysis, performed in software like COMSOL, reveals the distinct mode shapes and resonant frequencies of the piezoelectric device (simulation results, right). This analysis is crucial for ensuring that each mode possesses strong electromechanical coupling for efficient actuation and detection for multi-mode sensing.

The defect cell has a set of discrete resonant modes, which can be obtained by performing an eigenfrequency analysis using the Finite Element Method (FEM). This simulation solves for the eigenvalues of the defect cell's geometry, providing a catalog of its natural vibrational frequencies and the corresponding mode shapes. For a mode to be useful for the experiments, it must achieve high electromechanical coupling when electrodes are introduced.

The strength of this coupling is fundamentally governed by the anisotropic nature of the Lithium Niobate crystal. The crystal orientation (or "cut") determines which strain components will generate an electric field and vice-versa. The engineering task is therefore to align an optimized electrode geometry with the crystal axes in a way that maximizes the interaction with a desired mechanical mode. This involves carefully designing the shape, position, and gap (w_g) of the electrodes.

The electromechanical coupling is quantified by the coupling coefficient, k^2_{eff}. It is defined as the ratio of the stored mechanical energy to the stored electrical energy, therefore, this metric is a figure of merit that quantifies how efficiently a piezoelectric resonator converts energy between its electrical and mechanical forms [136]. This can be calculated by performing a piezoelectric simulation in FEM, which generates an admittance plot for each mode.

In a piezoelectric resonator, we observe two key resonant frequencies in the admittance or reactance plot: series resonance (f_s) and parallel resonance (f_p). These arise from the interaction between the material's mechanical properties and its electrical behavior [137]. Series resonance is associated with the natural resonance frequency of the mechanical mode, as the mechanical vibrations provide the minimum electrical impedance (if we think as L and C in series, on-resonance they cancel out). Parallel resonance, also known as anti-resonance, is due to the interactions between the mechanical resonator and its electrical connections (capacitor due to electrodes). These two frequencies are related to the k^2_{eff} as

$$k^2_{eff} = \frac{f_p^2 - f_s^2}{f_p^2}. \tag{7.11}$$

Therefore, the frequency seperation between these two resonances serves as a direct proxy for the resonator's energy conversion efficiency. In Fig. 7.7B, we demonstrate simulated admittance plot for the two modes at frequencies of 1.76 and 4.06 GHz, with the simulated k^2_{eff} of $\approx 25\%$ and 20%, respectively.

The bandgap engineering and mode isolation requires careful determination of the acoustic properties of the crystal and the defect cell. This involves designing the PnC's mirror cell. The different mechanical modes will naturally have separated frequencies. Therefore, the device requires either an exceptionally wide bandgap that can accommodate all the modes, or potentially multiple, distinct bandgaps. The design process relies heavily on the FEM, typically using software like COMSOL Multiphysics. The band structure is calculated by modeling a single unit cell of the PnC and applying Bloch-Floquet periodic boundary conditions. The simulation solves the underlying wave equation for elastodynamics:

$$\nabla \cdot (\mathbf{c} : \nabla \mathbf{u}) = -\rho\omega^2 \mathbf{u} \tag{7.12}$$

where $\mathbf{u}$ is the displacement vector, ρ is the material density, $\mathbf{c}$ is the elastic stiffness tensor, and ω is the angular frequency. By solving for ω across a range of wave vectors ($\mathbf{k}$), we can generate a dispersion diagram (frequency vs. wave vector). The bandgaps are the frequency ranges on this diagram where there are no solutions.

For the two-modes we have studied the electromechanical coupling, since the frequencies are well-separated (1 GHz and 4 GHz), having a single bandgap is not feasible, therefore, we need to have multiple bandgaps to have the two modes within

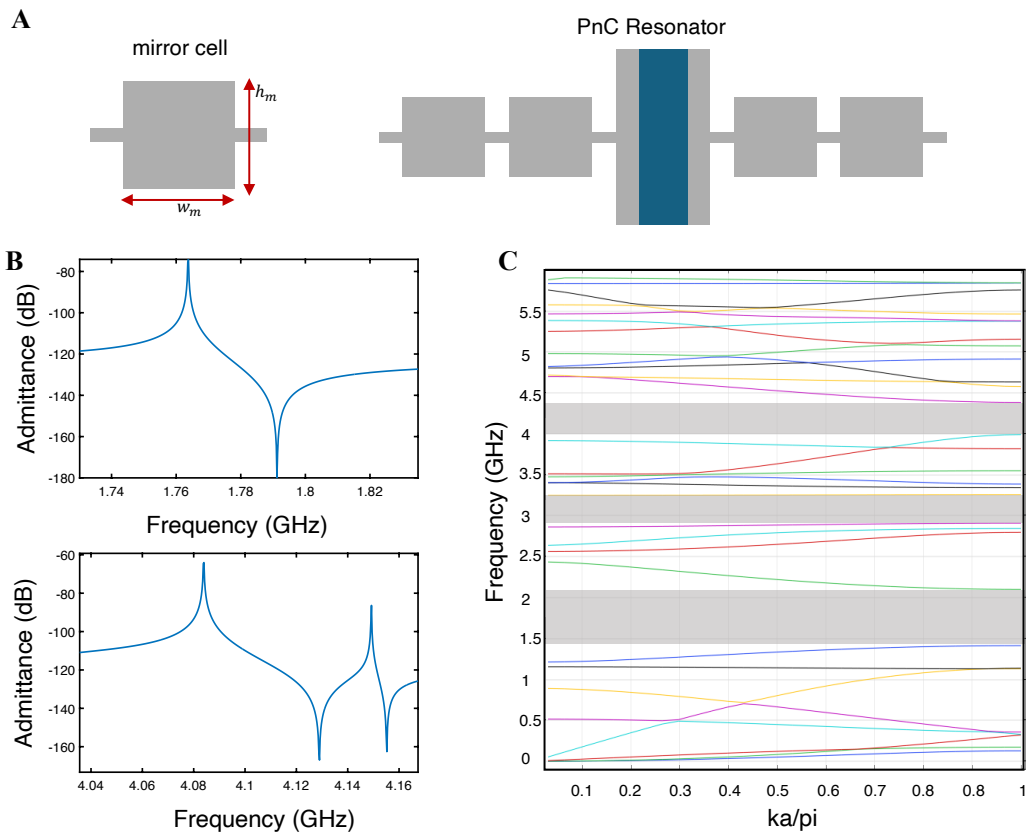

Figure 7.7: **Multimode LN Resonator Design 2.** **(A)** Schematic of the PnC resonator, constructed from a central defect cell and periodic mirror cells. The mirror cell geometry (w_m, h_m) defines the phononic crystal. **(B)** Simulated electrical admittance of the PnC resonator. Sharp, high-quality factor resonant peaks appear at frequencies (~1.78 GHz and ~4.1 GHz) designed to fall within the bandgaps in **(C)** , confirming that the PnC mirrors provide strong acoustic confinement for the modes within the defect cell. **(C)** The simulated band structure for the mirror cell array, revealing seperate phononic bandgaps at different frequencies (shaded gray).

those bandgaps. The key to designing these bandgaps lies in understanding the mirro cell's geometry as a local resonant system. The mirror cell can be conceptualized as a primary mass (the main body) connected by springs (the tethers). The geometry of these elements determines the local resonant frequency. This local resonance is what opens the bandgap. By carefully tuning these geometric parameters, we can position the bandgaps to overlap with our target operating frequencies, thereby isolating the resonators. While this process can be automated, a conceptual understanding of this mass-spring relationship is crucial for an effective initial design. In Fig. 7.7C, we demonstrate the simulated bandgap diagram for the engineered mirror cell design which delivers acoustic bandgaps at the two-mode frequencies.

While this section outlines the foundational principles of the PnC design at the surface level, the final device parameters are achieved through an iterative process that combines simulation with fabrication. The LN PnC devices used for the mass sensing experiments in this thesis were fabricated at Stanford University by the LINQS research group as part of this collaborative research effort.

7.3.2 Preliminary Results on NEMS-MS Experiments with PnC Resonators

Initial experiments with PnC resonators were performed on a single-mode device to observe its piezoelectric behavior under charged molecule loading within our hybrid system. The device has a fundamental shear mode, studied in the previous chapters, with smaller in size ($\sim$ 500 nm $\times$ 500 nm) and thickness (150 nm) resulting in the fundamental shear frequency of $\omega_m/2\pi \approx 3.6$ GHz. The microwave measurement setup in the Hybrid platform is redesigned to operate at the GHz regime for the reflection measurement characterization, significantly higher than the Si devices previously measured. The measurement setup was similar to that shown in Fig. B.1, but with the addition of PLL using the built-in function of the lock-in amplifier.

Using this platform, we have preformed mass sensing measurements with Apoferritin protein on LN PnC resonators at 80K temperature with liquid nitrogen cooling. The experimental results demonstrating the individual frequency shifts due to protein absorption on the PnC is shown in Fig. 7.8. While these experiments mark the first NEMS-MS performed in the GHz regime and open the door for future work, estimating the analyte's mass from a single mode alone is tricky. One could potentially collect numerous data points and use statistical tools, assuming a uniform distribution of events on the surface, to extract the mass. Our initial estimate, from calculating the expected shift from a single Apoferritin landing on the anti-node of the mode shape, yields a value of approximately [10 kHz]. This calculated maximum shift aligns with the larger frequency jumps observed in our experimental data.

As a next step, we have worked on characterization of the multi-mode PnC resonators. The experimental setup has been modified for the simultaneous readout of the two-modes, as shown in Figure. The allan deviation measured by simultaneous PLL for the two-modes is shown. A primary challenge in this work remains the difficulty in achieving high electromechanical coupling across all available modes at 80 K temperatures, as the Hybrid setup is mainly optimized for this cooling.

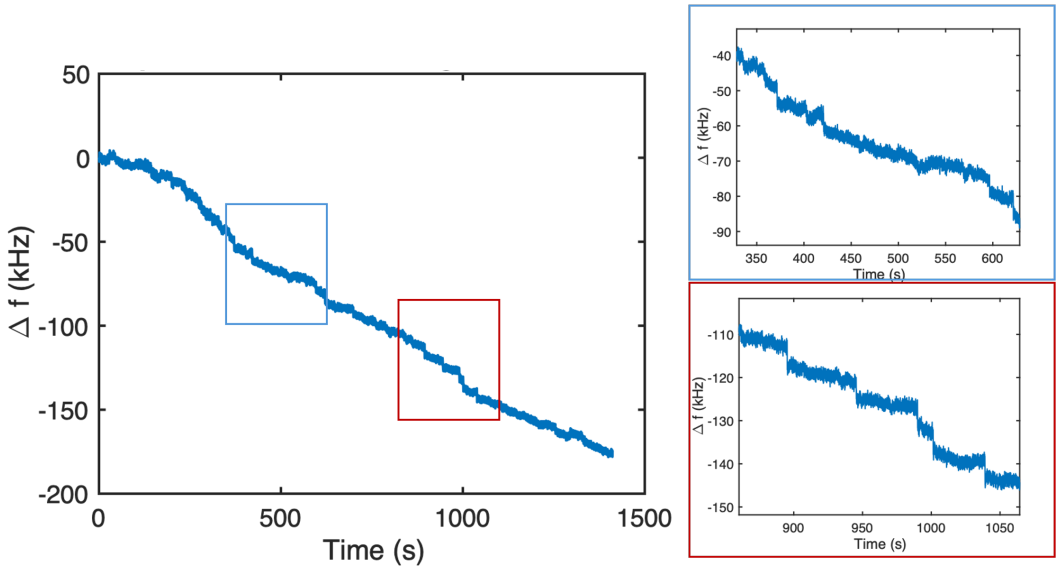

Figure 7.8: **GHz NEMS Mass Sensing.** Time series data of mass sensing experiments with single Apoferritin molecules using a single-mode LN device. A PLL tracks the resonator's frequency shift (Δf) over time. The discrete downward jumps in frequency, shown magnified in the insets, correspond to the absorption of individual molecules to the resonator surface. This proof-of-concept experiment marks the first demonstration of NEMS mass spectrometry in the GHz regime within our hybrid mass spectrometer.

Compared to the silicon doubly-clamped beam resonators discussed in the previous section, the mode shapes of phononic crystal (PnC) resonators differ dramatically. While the first critical challenge was to the design and fabrication of multi-mode PnC resonators, calculating the mass of a single analyte also cannot be done with traditional methods applied to nanobeams. The measurement method remains the same in terms of measuring frequency shifts induced by a single molecule; however, the 2D architecture of the mode shapes in PnC devices makes mass calculation from these shifts more complex. Moreover, these higher-order shear mode shapes are not as well-characterized as those of a simple nanobeam and small deviations due to fabrication imperfections can lead to drastic changes in the mode shape.

To overcome this challenge, our group has developed a data-driven approach that circumvents these limitations by eliminating the requirement of knowing the mode shape in advance [49]. This method uses a calibration-based algorithm—termed the "learning phase"—which utilizes a frequency-shift "fingerprint" from several modes to perform the mass measurement and is well-suited for our hybrid system with proteins, since proteins exhibit small variations in mass and size.

7.4 Towards NEMS-MS in Quantum Regime

Building upon successful NEMS-MS experiments with Si doubly-clamped beam resonators as well as preliminary results with multimode PnC resonators operating in the GHz regime, the ultimate goal for this technology is to achieve quantum sensitivities. While the initial experiments with LN PnC devices in quantum regime have demonstrated that the conventional mass sensing, which relies on resolving frequency shifts, may be fundamentally limited by noise introduced by TLS defects, it promises another type of quantum sensing by exchanging energy quanta with the mechanical resonator mode through strong coupling. The feasibility of this approach is evidenced by our direct observation of strong coupling between the mechanical mode and individual TLS defects. This principle can be extended to an extrinsic particle, enabling a similarly strong, observable interaction between the resonator and a single protein. Such a technique would transcend simple mass detection combined with the conventional mass sensing, quantum sensing promises to unlock structural and compositional information about native proteins with unprecedented detail.

When a protein lands on the resonator, its internal degrees of freedom (e.g., a dipolar or vibrational mode) can interact strongly with the mechanical mode of the NEMS device. Instead of a simple frequency shift, this interaction can create new hybrid mechanical-protein states, visible as an "avoided crossing" in the system's energy spectrum. The magnitude of this coupling, g, provides a direct probe into the protein's intrinsic properties, offering a path to sensing its structure and conformation, not just its mass. Since the most functionally relevant protein vibrations occur in the terahertz (THz) range, developing NEMS resonators that operate in the gigahertz (GHz) regime is the critical first step. This provides the high-energy mechanical quanta necessary to interact with these THz modes, paving the way for a new form of single-molecule quantum spectroscopy.

Reaching this goal requires an advanced hybrid platform—essentially a mass spectrometer unit integrated with a dilution refrigerator—capable of operating at 10 mK. Our initial efforts involve designing of such unit. This involves great engineering challenges to maintain such cryogenic temperatures while controllably delivering proteins from room temperature to the millikelvin stage.

BIBLIOGRAPHY

[1] R. Zeller and R. Pohl, "Thermal conductivity and specific heat of noncrystalline solids", Physical Review B **4**, 2029 (1971).

[2] P. W. Anderson, B. I. Halperin, and C. M. Varma, "Anomalous low-temperature thermal properties of glasses and spin glasses", Philosophical Magazine **25**, 1–9 (1972).

[3] W. A. Phillips, "Tunneling states in amorphous solids", Journal of low temperature physics **7**, 351–360 (1972).

[4] P. Esquinazi, *Tunneling systems in amorphous and crystalline solids* (Springer Science & Business Media, 2013).

[5] R. W. Simmonds, K. Lang, D. A. Hite, S. Nam, D. P. Pappas, and J. M. Martinis, "Decoherence in josephson phase qubits from junction resonators", Physical Review Letters **93**, 077003 (2004).

[6] J. M. Martinis, K. B. Cooper, R. McDermott, M. Steffen, M. Ansmann, K. Osborn, K. Cicak, S. Oh, D. P. Pappas, R. W. Simmonds, et al., "Decoherence in josephson qubits from dielectric loss", Physical review letters **95**, 210503 (2005).

[7] J. Gao, M. Daal, A. Vayonakis, S. Kumar, J. Zmuidzinas, B. Sadoulet, B. A. Mazin, P. K. Day, and H. G. Leduc, "Experimental evidence for a surface distribution of two-level systems in superconducting lithographed microwave resonators", Applied Physics Letters **92** (2008).

[8] G. J. Grabovskij, T. Peichl, J. Lisenfeld, G. Weiss, and A. V. Ustinov, "Strain tuning of individual atomic tunneling systems detected by a superconducting qubit", Science **338**, 232–234 (2012).

[9] K. Ekinci and M. Roukes, "Nanoelectromechanical systems", Review of scientific instruments **76** (2005).

[10] A. Bachtold, J. Moser, and M. Dykman, "Mesoscopic physics of nanomechanical systems", Reviews of Modern Physics **94**, 045005 (2022).

[11] K. C. Schwab and M. L. Roukes, "Putting mechanics into quantum mechanics", Physics Today **58**, 36–42 (2005).

[12] G. S. MacCabe, H. Ren, J. Luo, J. D. Cohen, H. Zhou, A. Sipahigil, M. Mirhosseini, and O. Painter, "Nano-acoustic resonator with ultralong phonon lifetime", Science **370**, 840–843 (2020).

[13] P. Arrangoiz-Arriola, E. A. Wollack, Z. Wang, M. Pechal, W. Jiang, T. P. McKenna, J. D. Witmer, R. Van Laer, and A. H. Safavi-Naeini, "Resolving the energy levels of a nanomechanical oscillator", Nature **571**, 537–540 (2019).

[14] A. Bozkurt, H. Zhao, C. Joshi, H. G. LeDuc, P. K. Day, and M. Mirhosseini, "A quantum electromechanical interface for long-lived phonons", Nature Physics **19**, 1326–1332 (2023).

[15] A. D. O'Connell, M. Hofheinz, M. Ansmann, R. C. Bialczak, M. Lenander, E. Lucero, M. Neeley, D. Sank, H. Wang, M. Weides, et al., "Quantum ground state and single-phonon control of a mechanical resonator", Nature **464**, 697–703 (2010).

[16] Y. Chu, P. Kharel, W. H. Renninger, L. D. Burkhart, L. Frunzio, P. T. Rakich, and R. J. Schoelkopf, "Quantum acoustics with superconducting qubits", Science **358**, 199–202 (2017).

[17] Y. Chu, P. Kharel, T. Yoon, L. Frunzio, P. T. Rakich, and R. J. Schoelkopf, "Creation and control of multi-phonon fock states in a bulk acoustic-wave resonator", Nature **563**, 666–670 (2018).

[18] K. J. Satzinger, Y. Zhong, H.-S. Chang, G. A. Peairs, A. Bienfait, M.-H. Chou, A. Cleland, C. R. Conner, É. Dumur, J. Grebel, et al., "Quantum control of surface acoustic-wave phonons", Nature **563**, 661–665 (2018).

[19] L. R. Sletten, B. A. Moores, J. J. Viennot, and K. W. Lehnert, "Resolving phonon fock states in a multimode cavity with a double-slit qubit", Physical Review X **9**, 021056 (2019).

[20] D. Mason, J. Chen, M. Rossi, Y. Tsaturyan, and A. Schliesser, "Continuous force and displacement measurement below the standard quantum limit", Nature Physics **15**, 745–749 (2019).

[21] C. T. Hann, C.-L. Zou, Y. Zhang, Y. Chu, R. J. Schoelkopf, S. M. Girvin, and L. Jiang, "Hardware-efficient quantum random access memory with hybrid quantum acoustic systems", Physical review letters **123**, 250501 (2019).

[22] A. H. Safavi-Naeini and O. Painter, "Proposal for an optomechanical traveling wave phonon–photon translator", New Journal of Physics **13**, 013017 (2011).

[23] E. A. Wollack, A. Y. Cleland, P. Arrangoiz-Arriola, T. P. McKenna, R. G. Gruenke, R. N. Patel, W. Jiang, C. J. Sarabalis, and A. H. Safavi-Naeini, "Loss channels affecting lithium niobate phononic crystal resonators at cryogenic temperature", Applied Physics Letters **118** (2021).

[24] J. Travis, "Building bridges to the nanoworld", Science **263**, 1702–1703 (1994).

[25] A. N. Cleland and M. L. Roukes, "Fabrication of high frequency nanometer scale mechanical resonators from bulk si crystals", Applied Physics Letters **69**, 2653–2655 (1996).

[26] T. Kouh, M. S. Hanay, and K. L. Ekinci, "Nanomechanical motion transducers for miniaturized mechanical systems", Micromachines **8**, 108 (2017).

[27] C. Meyer, H. Lorenz, and K. Karrai, "Optical detection of quasi-static actuation of nanoelectromechanical systems", Applied Physics Letters **83**, 2420–2422 (2003).

[28] T. Kouh, D. Karabacak, D. Kim, and K. Ekinci, "Diffraction effects in optical interferometric displacement detection in nanoelectromechanical systems", Applied Physics Letters **86** (2005).

[29] S. C. Masmanidis, R. B. Karabalin, I. De Vlaminck, G. Borghs, M. R. Freeman, and M. L. Roukes, "Multifunctional nanomechanical systems via tunably coupled piezoelectric actuation", Science **317**, 780–783 (2007).

[30] R. Karabalin, S. Masmanidis, and M. Roukes, "Efficient parametric amplification in high and very high frequency piezoelectric nanoelectromechanical systems", Applied Physics Letters **97** (2010).

[31] M. Li, H. X. Tang, and M. L. Roukes, "Ultra-sensitive nems-based cantilevers for sensing, scanned probe and very high-frequency applications", Nature nanotechnology **2**, 114–120 (2007).

[32] I. Bargatin, I. Kozinsky, and M. Roukes, "Efficient electrothermal actuation of multiple modes of high-frequency nanoelectromechanical resonators", Applied Physics Letters **90** (2007).

[33] P. A. Truitt, J. B. Hertzberg, C. Huang, K. L. Ekinci, and K. C. Schwab, "Efficient and sensitive capacitive readout of nanomechanical resonator arrays", Nano letters **7**, 120–126 (2007).

[34] M. S. Kushwaha, P. Halevi, L. Dobrzynski, and B. Djafari-Rouhani, "Acoustic band structure of periodic elastic composites", Physical review letters **71**, 2022 (1993).

[35] A. Khelif, B. Djafari-Rouhani, J. O. Vasseur, and P. Deymier, "Transmission and dispersion relations of perfect and defect-containing waveguide structures in phononic band gap materials", Physical Review B **68**, 024302 (2003).

[36] M. Eichenfield, J. Chan, R. M. Camacho, K. J. Vahala, and O. Painter, "Optomechanical crystals", nature **462**, 78–82 (2009).

[37] P. Arrangoiz-Arriola and A. H. Safavi-Naeini, "Engineering interactions between superconducting qubits and phononic nanostructures", Physical Review A **94**, 063864 (2016).

[38] J. Chan, A. H. Safavi-Naeini, J. T. Hill, S. Meenehan, and O. Painter, "Optimized optomechanical crystal cavity with acoustic radiation shield", Applied Physics Letters **101** (2012).

[39] S. Sonar, U. Hatipoglu, S. Meesala, D. P. Lake, H. Ren, and O. Painter, "High-efficiency low-noise optomechanical crystal photon-phonon transducers", Optica **12**, 99–104 (2025).

[40] A. L. Emser, C. Metzger, B. C. Rose, and K. W. Lehnert, "Thin-film quartz for high-coherence piezoelectric phononic crystal resonators", Physical Review Applied **22**, 064032 (2024).

[41] K. Ekinci, Y. T. Yang, and M. Roukes, "Ultimate limits to inertial mass sensing based upon nanoelectromechanical systems", Journal of applied physics **95**, 2682–2689 (2004).

[42] K. Jensen, K. Kim, and A. Zettl, "An atomic-resolution nanomechanical mass sensor", Nature nanotechnology **3**, 533–537 (2008).

[43] Y.-T. Yang, C. Callegari, X. Feng, K. L. Ekinci, and M. L. Roukes, "Zeptogram-scale nanomechanical mass sensing", Nano letters **6**, 583–586 (2006).

[44] B. Lassagne, D. Garcia-Sanchez, A. Aguasca, and A. Bachtold, "Ultrasensitive mass sensing with a nanotube electromechanical resonator", Nano letters **8**, 3735–3738 (2008).

[45] M. S. Hanay, S. Kelber, A. Naik, D. Chi, S. Hentz, E. Bullard, E. Colinet, L. Duraffourg, and M. Roukes, "Single-protein nanomechanical mass spectrometry in real time", Nature nanotechnology **7**, 602–608 (2012).

[46] M. S. Hanay, S. I. Kelber, C. D. O'Connell, P. Mulvaney, J. E. Sader, and M. L. Roukes, "Inertial imaging with nanomechanical systems", Nature nanotechnology **10**, 339–344 (2015).

[47] M. Yuksel, E. Orhan, C. Yanik, A. B. Ari, A. Demir, and M. S. Hanay, "Nonlinear nanomechanical mass spectrometry at the single-nanoparticle level", Nano letters **19**, 3583–3589 (2019).

[48] B. E. Kaynak, M. Alkhaled, E. Kartal, C. Yanik, and M. S. Hanay, "Atmospheric-pressure mass spectrometry by single-mode nanoelectromechanical systems", Nano Letters **23**, 8553–8559 (2023).

[49] J. E. Sader, A. Gomez, A. P. Neumann, A. Nunn, and M. L. Roukes, "Data-driven fingerprint nanoelectromechanical mass spectrometry", Nature Communications **15**, 8800 (2024).

[50] M. Sansa, E. Sage, E. C. Bullard, M. Gély, T. Alava, E. Colinet, A. K. Naik, L. G. Villanueva, L. Duraffourg, M. L. Roukes, et al., "Frequency fluctuations in silicon nanoresonators", Nature nanotechnology **11**, 552–558 (2016).

[51] A. Demir and M. S. Hanay, "Fundamental sensitivity limitations of nanomechanical resonant sensors due to thermomechanical noise", IEEE Sensors Journal **20**, 1947–1961 (2019).

[52] A. H. Safavi-Naeini, J. Chan, J. T. Hill, T. P. M. Alegre, A. Krause, and O. Painter, "Observation of quantum motion of a nanomechanical resonator", Physical Review Letters **108**, 033602 (2012).

[53] I. Mahboob, K. Nishiguchi, H. Okamoto, and H. Yamaguchi, "Phonon-cavity electromechanics", Nature Physics **8**, 387–392 (2012).

[54] E. E. Wollman, C. Lei, A. Weinstein, J. Suh, A. Kronwald, F. Marquardt, A. A. Clerk, and K. Schwab, "Quantum squeezing of motion in a mechanical resonator", Science **349**, 952–955 (2015).

[55] A. Wallucks, I. Marinković, B. Hensen, R. Stockill, and S. Gröblacher, "A quantum memory at telecom wavelengths", Nature Physics **16**, 772–777 (2020).

[56] N. J. Lambert, A. Rueda, F. Sedlmeir, and H. G. Schwefel, "Coherent conversion between microwave and optical photons—an overview of physical implementations", Advanced Quantum Technologies **3**, 1900077 (2020).

[57] R. Katsumi, K. Takada, K. Kawai, D. Sato, and T. Yatsui, "High-sensitivity nanoscale quantum sensors based on a diamond micro-resonator", Communications Materials **6**, 1–8 (2025).

[58] L. M. Smith and N. L. Kelleher, "Proteoform: a single term describing protein complexity", Nature methods **10**, 186–187 (2013).

[59] C. Müller, J. H. Cole, and J. Lisenfeld, "Towards understanding two-level-systems in amorphous solids: insights from quantum circuits", Reports on Progress in Physics **82**, 124501 (2019).

[60] J. Black and B. Halperin, "Spectral diffusion, phonon echoes, and saturation recovery in glasses at low temperatures", Physical Review B **16**, 2879 (1977).

[61] R. G. Gruenke, O. A. Hitchcock, E. A. Wollack, C. J. Sarabalis, M. Jankowski, T. P. McKenna, N. R. Lee, and A. H. Safavi-Naeini, "Surface modification and coherence in lithium niobate saw resonators", Scientific Reports **14**, 6663 (2024).

[62] R. G. Gruenke-Freudenstein, E. Szakiel, G. P. Multani, T. Makihara, A. G. Hayden, A. Khalatpour, E. A. Wollack, A. Akoto-Yeboah, S. Salmani-Rezaie, and A. H. Safavi-Naeini, "Surface and bulk two-level system losses in lithium niobate acoustic resonators", arXiv preprint arXiv:2501.08291 (2025).

[63] J. Gao, M. Daal, J. M. Martinis, A. Vayonakis, J. Zmuidzinas, B. Sadoulet, B. A. Mazin, P. K. Day, and H. G. Leduc, "A semiempirical model for two-level system noise in superconducting microresonators", Applied Physics Letters **92** (2008).

[64] G. Lindblad, "On the generators of quantum dynamical semigroups", Communications in mathematical physics **48**, 119–130 (1976).

[65] S. Haroche and J.-M. Raimond, *Exploring the quantum: atoms, cavities, and photons* (Oxford university press, 2006).

[66] H.-P. Breuer and F. Petruccione, *The theory of open quantum systems* (Oxford University Press, USA, 2002).

[67] A. Rivas and S. F. Huelga, *Open quantum systems*, Vol. 10 (Springer, 2012).

[68] C. W. Gardiner and M. J. Collett, "Input and output in damped quantum systems: quantum stochastic differential equations and the master equation", Physical Review A **31**, 3761 (1985).

[69] F. Pobell, *Matter and methods at low temperatures*, Vol. 2 (Springer, 2007).

[70] S. Krinner, S. Storz, P. Kurpiers, P. Magnard, J. Heinsoo, R. Keller, J. Luetolf, C. Eichler, and A. Wallraff, "Engineering cryogenic setups for 100-qubit scale superconducting circuit systems", EPJ Quantum Technology **6**, 2 (2019).

[71] C. Gardiner and P. Zoller, *Quantum noise: a handbook of markovian and non-markovian quantum stochastic methods with applications to quantum optics* (Springer Science & Business Media, 2004).

[72] A. A. Abrikosov, *Fundamentals of the theory of metals* (Courier Dover Publications, 2017).

[73] K. DeBry and G. Lafyatis, "Note: electroplating process for connectorizing superconducting nbti cables", Review of Scientific Instruments **89** (2018).

[74] M. Yuksel, M. Maksymowych, O. Hitchcock, F. Mayor, N. Lee, M. Dykman, A. Safavi-Naeini, and M. Roukes, "Intrinsic phononic dressed states in a nanomechanical system", arXiv preprint arXiv:2502.18587 (2025).

[75] P. Arrangoiz-Arriola, E. A. Wollack, M. Pechal, J. D. Witmer, J. T. Hill, and A. H. Safavi-Naeini, "Coupling a superconducting quantum circuit to a phononic crystal defect cavity", Physical Review X **8**, 031007 (2018).

[76] A. N. Cleland, *Foundations of nanomechanics: from solid-state theory to device applications* (Springer Science & Business Media, 2013).

[77] A. Y. Cleland, E. A. Wollack, and A. H. Safavi-Naeini, "Studying phonon coherence with a quantum sensor", Nature Communications **15**, 4979 (2024).

[78] J. Lisenfeld, G. J. Grabovskij, C. Müller, J. H. Cole, G. Weiss, and A. V. Ustinov, "Observation of directly interacting coherent two-level systems in an amorphous material", Nature communications **6**, 6182 (2015).

[79] A. Bilmes, S. Volosheniuk, A. V. Ustinov, and J. Lisenfeld, "Probing defect densities at the edges and inside josephson junctions of superconducting qubits", npj Quantum Information **8**, 24 (2022).

[80] S. M. Meißner, A. Seiler, J. Lisenfeld, A. V. Ustinov, and G. Weiss, "Probing individual tunneling fluctuators with coherently controlled tunneling systems", Physical Review B **97**, 180505 (2018).

[81] M. Kristen, J. Voss, M. Wildermuth, A. Bilmes, J. Lisenfeld, H. Rotzinger, and A. Ustinov, "Giant two-level systems in a granular superconductor", Physical Review Letters **132**, 217002 (2024).

[82] J. Lisenfeld, A. Bilmes, A. Megrant, R. Barends, J. Kelly, P. Klimov, G. Weiss, J. M. Martinis, and A. V. Ustinov, "Electric field spectroscopy of material defects in transmon qubits", npj Quantum Information **5**, 105 (2019).

[83] E. T. Jaynes and F. W. Cummings, "Comparison of quantum and semiclassical radiation theories with application to the beam maser", Proceedings of the IEEE **51**, 89–109 (1963).

[84] B. Sarabi, A. N. Ramanayaka, A. L. Burin, F. C. Wellstood, and K. D. Osborn, "Cavity quantum electrodynamics using a near-resonance two-level system: emergence of the glauber state", Applied Physics Letters **106** (2015).

[85] M. I. Dykman and M. A. Ivanov, "Spectral distribution of resonant localized impurity vibrations at finite temperatures", Fiz. Tverd. Tela **18**, Translated as *Soviet Physics - Solid State*, 18, 415–420 (1976), 720–729 (1976).

[86] A. Blais, A. L. Grimsmo, S. M. Girvin, and A. Wallraff, "Circuit quantum electrodynamics", Reviews of Modern Physics **93**, 025005 (2021).

[87] J. R. Johansson, P. D. Nation, and F. Nori, "Qutip: an open-source python framework for the dynamics of open quantum systems", Computer physics communications **183**, 1760–1772 (2012).

[88] M. Brune, F. Schmidt-Kaler, A. Maali, J. Dreyer, E. Hagley, J. Raimond, and S. Haroche, "Quantum rabi oscillation: a direct test of field quantization in a cavity", Physical review letters **76**, 1800 (1996).

[89] D. Schuster, A. A. Houck, J. Schreier, A. Wallraff, J. Gambetta, A. Blais, L. Frunzio, J. Majer, B. Johnson, M. Devoret, et al., "Resolving photon number states in a superconducting circuit", Nature **445**, 515–518 (2007).

[90] L. S. Bishop, J. Chow, J. Koch, A. Houck, M. Devoret, E. Thuneberg, S. Girvin, and R. Schoelkopf, "Nonlinear response of the vacuum rabi resonance", Nature Physics **5**, 105–109 (2009).

[91] J. Fink, M. Göppl, M. Baur, R. Bianchetti, P. J. Leek, A. Blais, and A. Wallraff, "Climbing the jaynes–cummings ladder and observing its nonlinearity in a cavity qed system", Nature **454**, 315–318 (2008).

[92] E. Ginossar, L. Bishop, and S. Girvin, "Nonlinear oscillators and high fidelity qubit state measurement in circuit quantum electrodynamics", Fluctuating Nonlinear Oscillators. From Nanomechanics to Quantum Superconducting Circuits **8**, 198 (2012).

[93] V. Peano and M. Thorwart, "Quasienergy description of the driven jaynes-cummings model", Physical Review B—Condensed Matter and Materials Physics **82**, 155129 (2010).

[94] T. Bonsen, P. Harvey-Collard, M. Russ, J. Dijkema, A. Sammak, G. Scappucci, and L. M. Vandersypen, "Probing the jaynes-cummings ladder with spin circuit quantum electrodynamics", Physical review letters **130**, 137001 (2023).

[95] Y. Zhang, J. C. Curtis, C. S. Wang, R. Schoelkopf, and S. Girvin, "Drive-induced nonlinearities of cavity modes coupled to a transmon ancilla", Physical Review A **105**, 022423 (2022).

[96] M. Boissonneault, J. M. Gambetta, and A. Blais, "Nonlinear dispersive regime of cavity qed: the dressed dephasing model", Physical Review A—Atomic, Molecular, and Optical Physics **77**, 060305 (2008).

[97] J. Fink, L. Steffen, P. Studer, L. S. Bishop, M. Baur, R. Bianchetti, D. Bozyigit, C. Lang, < f. S. Filipp, P. J. Leek, et al., "Quantum-to-classical transition in cavity quantum electrodynamics", Physical review letters **105**, 163601 (2010).

[98] I. Rau, G. Johansson, and A. Shnirman, "Cavity quantum electrodynamics in superconducting circuits: susceptibility at elevated temperatures", Physical Review B—Condensed Matter and Materials Physics **70**, 054521 (2004).

[99] J. Burnett, L. Faoro, I. Wisby, V. L. Gurtovoi, A. V. Chernykh, G. M. Mikhailov, V. A. Tulin, R. Shaikhaidarov, V. Antonov, P. J. Meeson, et al., "Evidence for interacting two-level systems from the 1/f noise of a superconducting resonator", Nature Communications **5**, 4119 (2014).

[100] J. Béjanin, Y. Ayadi, X. Xu, C. Zhu, H. Mohebbi, and M. Mariantoni, "Fluctuation spectroscopy of two-level systems in superconducting resonators", Physical Review Applied **18**, 034009 (2022).

[101] S. De Graaf, S. Mahashabde, S. Kubatkin, A. Y. Tzalenchuk, and A. Danilov, "Quantifying dynamics and interactions of individual spurious low-energy fluctuators in superconducting circuits", Physical Review B **103**, 174103 (2021).

[102] L. Faoro and L. B. Ioffe, "Interacting tunneling model for two-level systems in amorphous materials and its predictions for their dephasing and noise in superconducting microresonators", Physical Review B **91**, 014201 (2015).

[103] U. Hatipoglu, S. Sonar, D. P. Lake, S. Meesala, and O. Painter, "In situ tuning of optomechanical crystals with nano-oxidation", Optica **11**, 371–375 (2024).

[104] W. Jiang, F. M. Mayor, S. Malik, R. Van Laer, T. P. McKenna, R. N. Patel, J. D. Witmer, and A. H. Safavi-Naeini, "Optically heralded microwave photon addition", Nature Physics **19**, 1423–1428 (2023).

[105] S. Meesala, S. Wood, D. Lake, P. Chiappina, C. Zhong, A. D. Beyer, M. D. Shaw, L. Jiang, and O. Painter, "Non-classical microwave–optical photon pair generation with a chip-scale transducer", Nature Physics, 1–7 (2024).

[106] P.-L. Yu, K. Cicak, N. Kampel, Y. Tsaturyan, T. Purdy, R. Simmonds, and C. Regal, "A phononic bandgap shield for high-q membrane microresonators", Applied Physics Letters **104** (2014).

[107] M. Chen, J. C. Owens, H. Putterman, M. Schäfer, and O. Painter, "Phonon engineering of atomic-scale defects in superconducting quantum circuits", Science Advances **10**, eado6240 (2024).

[108] A. B. Bozkurt, O. Golami, Y. Yu, H. Tian, and M. Mirhosseini, "A mechanical quantum memory for microwave photons", arXiv preprint arXiv:2412.08006 (2024).

[109] J. Atalaya, T. W. Kenny, M. Roukes, and M. Dykman, "Nonlinear damping and dephasing in nanomechanical systems", Physical Review B **94**, 195440 (2016).

[110] G. P. Srivastava, *The physics of phonons* (CRC press, 2022).

[111] Y. Yang, C. Callegari, X. Feng, and M. Roukes, "Surface adsorbate fluctuations and noise in nanoelectromechanical systems", Nano letters **11**, 1753–1759 (2011).

[112] K. Y. Fong, W. H. Pernice, and H. X. Tang, "Frequency and phase noise of ultrahigh q silicon nitride nanomechanical resonators", Physical Review B **85**, 161410 (2012).

[113] J. Atalaya, A. Isacsson, and M. Dykman, "Diffusion-induced dephasing in nanomechanical resonators", Physical Review B **83**, 045419 (2011).

[114] M. Wang, D. J. Perez-Morelo, G. Ramer, G. Pavlidis, J. J. Schwartz, L. Yu, R. Ilic, A. Centrone, and V. A. Aksyuk, "Beating thermal noise in a dynamic signal measurement by a nanofabricated cavity optomechanical sensor", Science Advances **9**, eadf7595 (2023).

[115] A. Cleland and M. Roukes, "Noise processes in nanomechanical resonators", Journal of applied physics **92**, 2758–2769 (2002).

[116] W. A. Phillips, "Two-level states in glasses", Reports on Progress in Physics **50**, 1657 (1987).

[117] R. O. Behunin, F. Intravaia, and P. T. Rakich, "Dimensional transformation of defect-induced noise, dissipation, and nonlinearity", Physical Review B **93**, 224110 (2016).

[118] G. Andersson, A. L. O. Bilobran, M. Scigliuzzo, M. M. de Lima, J. H. Cole, and P. Delsing, "Acoustic spectral hole-burning in a two-level system ensemble", npj Quantum Information **7**, 15 (2021).

[119] R. Manenti, M. Peterer, A. Nersisyan, E. Magnusson, A. Patterson, and P. Leek, "Surface acoustic wave resonators in the quantum regime", Physical Review B **93**, 041411 (2016).

[120] J. Burnett, L. Faoro, and T. Lindstrom, "Analysis of high quality superconducting resonators: consequences for tls properties in amorphous oxides", Superconductor Science and Technology **29** (2016).

[121] M. Lucas, A. Danilov, L. Levitin, A. Jayaraman, A. Casey, L. Faoro, A. Y. Tzalenchuk, S. Kubatkin, J. Saunders, and S. de Graaf, "Quantum bath suppression in a superconducting circuit by immersion cooling", Nature Communications **14**, 3522 (2023).

[122] C. R. H. McRae, H. Wang, J. Gao, M. R. Vissers, T. Brecht, A. Dunsworth, D. P. Pappas, and J. Mutus, "Materials loss measurements using superconducting microwave resonators", Review of Scientific Instruments **91** (2020).

[123] M. Kalaee, M. Mirhosseini, P. B. Dieterle, M. Peruzzo, J. M. Fink, and O. Painter, "Quantum electromechanics of a hypersonic crystal", Nature nanotechnology **14**, 334–339 (2019).

[124] D. B. Sullivan, D. W. Allan, D. A. Howe, D. Sullivan, and F. Walls, "Characterization of clocks and oscillators", (1990).

[125] E. Rubiola, *Phase noise and frequency stability in oscillators* (Cambridge University Press, 2008).

[126] J. A. Barnes, A. R. Chi, L. S. Cutler, D. J. Healey, D. B. Leeson, T. E. McGunigal, J. A. Mullen, W. L. Smith, R. L. Sydnor, R. F. Vessot, et al., "Characterization of frequency stability", IEEE transactions on instrumentation and measurement, 105–120 (1971).

[127] H. Bešić, A. Demir, J. Steurer, N. Luhmann, and S. Schmid, "Schemes for tracking resonance frequency for micro-and nanomechanical resonators", Physical Review Applied **20**, 024023 (2023).

[128] M. P. Maksymowych, M. Yuksel, O. A. Hitchcock, N. R. Lee, F. M. Mayor, W. Jiang, M. L. Roukes, and A. H. Safavi-Naeini, "Frequency fluctuations in nanomechanical resonators due to quantum defects", arXiv preprint arXiv:2501.08289 (2025).

[129] M. P. Maksymowych*, M. Yuksel*, O. A. Hitchcock, N. R. Lee, F. M. Mayor, W. Jiang, M. L. Roukes, and A. H. Safavi-Naeini, "Frequency fluctuations in nanomechanical resonators due to quantum defects", arXiv preprint arXiv:2501.08289 (2025),

[130] E. A. Wollack, A. Y. Cleland, R. G. Gruenke, Z. Wang, P. Arrangoiz-Arriola, and A. H. Safavi-Naeini, "Quantum state preparation and tomography of entangled mechanical resonators", Nature **604**, 463–467 (2022).

[131] V. Marx, "A dream of single-cell proteomics", Nature methods **16**, 809–812 (2019).

[132] A. P. Neumann, E. Sage, D. Boll, M. Reinhardt-Szyba, W. Fon, C. Masselon, S. Hentz, J. E. Sader, A. Makarov, and M. L. Roukes, "A hybrid orbitrap-nanoelectromechanical systems approach for the analysis of individual, intact proteins in real time", Angewandte Chemie **136**, e202317064 (2024).

[133] A. P. Neumann, *Towards single molecule imaging using nanoelectromechanical systems* (California Institute of Technology, 2020).

[134] J. Chaste, A. Eichler, J. Moser, G. Ceballos, R. Rurali, and A. Bachtold, "A nanomechanical mass sensor with yoctogram resolution", Nature nanotechnology **7**, 301–304 (2012).

[135] I. Bargatin, E. Myers, J. Arlett, B. Gudlewski, and M. Roukes, "Sensitive detection of nanomechanical motion using piezoresistive signal downmixing", Applied Physics Letters **86** (2005).

[136] H. Bhugra and G. Piazza, *Piezoelectric mems resonators* (Springer, 2017).

[137] D. M. Pozar, *Microwave engineering: theory and techniques* (John wiley & sons, 2021).

[138] A. W. Bowman and A. Azzalini, *Applied smoothing techniques for data analysis: the kernel approach with s-plus illustrations*, Vol. 18 (OUP Oxford, 1997).

[139] D. W. Scott, "On optimal and data-based histograms", Biometrika **66**, 605–610 (1979).

Appendix A

DEVICE DETAILS

The lithium niobate (LN) phononic crystal (PnC) nanoelectromechanical systems (NEMS) resonators studied in this thesis were fabricated at Stanford University in the Laboratory for Integrated Nano-Quantum Systems (LINQS), led by the group of Amir Safavi-Naeini. This work was part of a collaboration focused on NEMS mass sensing applications.

The devices are fabricated from a 250 nm thick X-cut congruent lithium niobate (LN) wafer bonded to a high resistivity $\langle 111 \rangle$ silicon handle. The fabrication details of our PnC NEMS resonators are explained elsewhere [23, 77, 128].

While the device fabrication is similar to that in previous works, the observation of strong coupling was enabled by two critical experimental conditions: 1) We probe the system at low phonon numbers to avoid TLS saturation and decoherence and, 2) Crucially, we employ a tunable DC bias to frequency match individual TLS with the resonator. The device we use in this work consists of an array of 9 resonators with slightly different defect cell dimensions, which enables frequency multiplexing. In addition to the resonator highlighted in the main text, we performed similar experiments on the other resonators in the array.

Silicon doubly-clamped beam resonators are fabricated at Caltech and the fabrication process is explained in the main-text.

Appendix B

DETAILED EXPERIMENTAL SETUP

For the experimental setup (Fig. 5.2) of piezoelectric actuation and detection of the NEMS, we employ a Zurich Instruments UHFLI lock-in amplifier (LI) to measure on-chip devices thermalized to the mixing chamber plate of a Bluefors horizontal (LH-400) dilution refrigerator. Due to the limited frequency range of the LI (0–600 MHz), the near-resonant drive signal ($\sim$ 1.9 GHz) is generated by mixing the output of the LI with a local oscillator (LO) at GHz frequency. After the mixing operation, the undesired sideband is filtered and the signal is transmitted to the device then passed to a superconducting output line via a cryogenic circulator (QCY-G0150201AM). The reflected signal is then mixed down to the LI frequency by the same LO, then filtered before reaching the LI input for demodulation. The LI and LO clocks are frequency locked. The reflected signal is amplified in two stages: first at the 4 K stage using a SiGe cryogenic amplifier (Cosmic Microwave CITLF3), and subsequently at room temperature using additional low-noise amplifiers (Mini-Circuits) as needed. An isolator at the 100 mK stage prevents amplifier input noise from reaching the device. The refrigerator drive line is highly attenuated and constructed from lossy beryllium copper (BeCu) coaxial cables to suppress thermal fluctuations from room temperature down to the 10 mK stage. Meanwhile, the readout line consists of superconducting niobium titanium (NbTi) coaxial cables from 10 mK to 4 K to minimize signal loss. A low-noise DC supply (Yokogawa; GS210) generates the static electrical bias across the device electrodes. The DC signal is routed through twisted-pair cables with sufficient thermalization at each stage within the dilution refrigerator, and a low-pass filter at the 4 K stage further reduces the high frequency noise. Just before reaching the device, the microwave drive and DC bias are combined using a bias tee circuit.

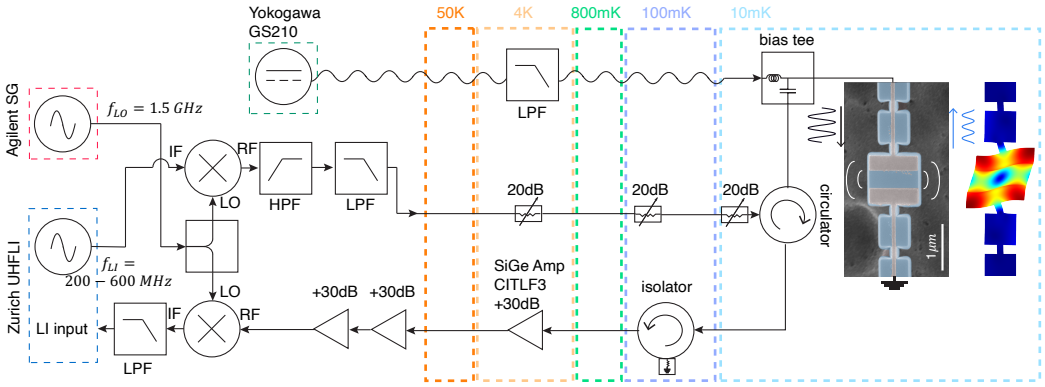

Figure B.1: **Detailed Experimental Setup.** Schematic of the horizontal dilution refrigerator measurement setup used to acquire all main text experimental data presented in this chapter. The microwave drive signal is generated by mixing the local oscillator (LO) tone from a signal generator (SG) at 1.5 GHz with the Zurich lock-in (LI) output in the DC - 600 MHz range. The signal is up-converted to near the resonance frequency ($\omega_m/2\pi \approx 1.87$ GHz) and the sidebands are removed by cascading the microwave tone through high pass (HPF) and low pass filters (LPF). The drive signal is then combined with the DC bias at the 10 mK stage via a bias tee circuit. The reflected signal is amplified at 4 K and at room temperature before being down-converted using the same LO tone and sent to the LI input for demodulation.

Appendix C

STRONG COUPLING MODELING AND SIMULATIONS

The simulated spectra of the double avoided crossing of individual TLSs are generated by solving the master equation Equation 5.5 for each DC detuning while varying the $\omega_{\mathrm{TLS}}(V_{\mathrm{dc}})$ according to the relation given in Equation 5.3. TLS,C1 and TLS,C2 frequency parameters (Δ_0, $\partial\varepsilon/\partial V_{\mathrm{dc}}$, ε_0), which determine their dependence on DC bias and yield excellent agreement with the experimental data, are provided in Table C. The NEMS-TLS coupling rate g is obtained by fitting the avoided crossing spectra in Fig. 5.7B. For all subsequent simulations, including those investigating power and temperature dependencies, the parameter set $\{\Delta_0, \varepsilon, \partial\varepsilon/\partial V_{\mathrm{dc}}, \mathrm{g}\}$ remains fixed, with only minor adjustments if the TLS frequency shifts slightly.

In addition to these fixed parameters, we allow the following parameters to vary with input drive power and temperature: the resonator's internal decay rate κ_i, the TLS decay rate γ_{TLS}, and the effective thermal occupancy n_{eff}. We also apply small adjustments to the external coupling rate κ_e to obtain optimal agreement. We determine these parameters based on best-fit estimates to the experimental data. To fit a single $|S_{11}|$ trace at a chosen DC bias, we first estimate κ_i and κ_e from the far-detuned response of the resonator— i.e., at large DC offset, where the resonator exhibits a single Lorentzian dip largely unaffected by the strongly coupled TLS. To fit to the split spectrum in the presence of strong coupling, we then employ a least-squares optimization to refine $\kappa_i, \kappa_e, \gamma_{\mathrm{TLS}},$ and n_{eff} by minimizing the mean squared error (MSE) between the simulated and experimental magnitudes of $|S_{11}|$. Concretely, $|S_{11}^{\mathrm{exp}}(\Delta_{m,i})|$ denotes the experimentally measured magnitude at the detuning $\Delta_{m,i}$, and $|S_{11}^{\mathrm{sim}}(\Delta_{m,i};\mathbf{p})|$ is the simulated magnitude obtained by numerically solving the master equation for a parameter set $\mathbf{p} = \{\kappa_i, \kappa_e, \gamma_{\mathrm{TLS}}, n_{eff}\}$. We then define:

$$\mathrm{MSE}(\mathbf{p}) = \frac{1}{N}\sum_{i=1}^{N}\left(|S_{11}^{\mathrm{sim}}(\Delta_{m,i};\mathbf{p})| \; - \; |S_{11}^{\mathrm{exp}}(\Delta_{m,i})|\right)^2, \tag{C.1}$$

where N is the total number of detuning points in that sweep. After several iterations, this procedure yields a set of parameters $\mathbf{p}' = \{\kappa_i', \kappa_e', \gamma_{\mathrm{TLS}}', n_{eff}\} = \mathrm{argmin}_{\mathbf{p}}\mathrm{MSE}(\mathbf{p})$ that provides good agreement with the experimental data, as demonstrated in the

TLS ID	Δ_0/h [GHz]	ε_0/h [GHz]	$\frac{1}{h}\frac{\partial\varepsilon}{\partial V_{\mathrm{dc}}}$ [GHz/V]	$g/2\pi$[MHz]
TLS,C1	1.8692	33.26	38.42	2.40
TLS,C2	1.8645	18.66	30.01	1.72

Table C.1: **TLS Parameters**. This table summarizes the key parameters of TLS,C1 and TLS,C2 used in simulations, where h is Planck's constant.

main text. Numerically simulating the system at high power and temperature requires a larger Fock-state basis in the master equation, increasing computational complexity.

The parameter n_{eff} accounts for the increased phonon occupancy arising from higher drive power or elevated temperature. We estimate the uncertainty in n_{eff} via the following approach. We fix all parameters in $\mathbf{p}'$ except n_{eff} and perform a one-dimensional sweep of n_{eff} in the vicinity of its initial best-fit value. We then define a threshold level $1.05\times\mathrm{MSE}(\mathbf{p}')$, corresponding to a 5% increase in MSE compared to the minimum MSE. The range of n_{eff} satisfying $\mathrm{MSE}(n_{eff}) \leq 1.05\times\mathrm{MSE}(\mathbf{p}')$ is taken to define the error bar of n_{eff} in the main text. An example of this sweep operation is illustrated in Fig. C.1.

The described method above for a single $|S_{11}|$ trace can be applied in two-dimensional parameter space by taking both Δ_m and DC bias V_{dc} as a sweep parameter. To capture the entire parameter space, we extend the MSE definition to include all $(\Delta_{m,i}, V_{dc,j})$ points in the spectra:

$$\mathrm{MSE}_{2\mathrm{D}}(\mathbf{p}) = \frac{1}{N_{\mathrm{total}}}\sum_{i=1}^{N_\Delta}\sum_{j=1}^{N_V}\left(|S_{11}^{\mathrm{sim}}(\Delta_{m,i}, V_{dc,j};\mathbf{p})| - |S_{11}^{\mathrm{exp}}(\Delta_{m,i}, V_{dc,j})|\right)^2, \quad \text{(C.2)}$$

where N_Δ is the number of detuning points, N_V is the number of DC bias points, and $N_{\mathrm{total}} = N_\Delta \times N_V$ is the total number of points. This approach assumes uncorrelated errors between the simulated and experimental data for each data point of the spectra. By minimizing $\mathrm{MSE}_{2\mathrm{D}}$ over the full $(\Delta_m, V_{\mathrm{dc}})$ plane, we obtain an optimized set of $\{\kappa_i, \kappa_e, \gamma_{\mathrm{TLS}}, n_{eff}\}$ that reproduces the system's response over a DC range that captures the TLS crossings. We find that optimization around critical DC tunings, where $\omega_m \approx \omega_{\mathrm{TLS}}$, yields parameter values consistent with those from the full 2D optimization. Table C.2 summarizes all the parameters that are used to produce simulated spectra in Fig. 5.7 and Fig. 5.10, along with the associated fitting errors (MSE, $\mathrm{MSE}_{2\mathrm{D}}$). For the single-phonon cooperativity values mentioned in the main-text, we use the decay rates of TLS and the mode for $n_{eff} \approx 1$ from the Table C.2.

P **[dBm]**	$\gamma_{\mathrm{TLS}}/2\pi$ [kHz]	$\kappa_i/2\pi$ [kHz]	$\kappa_e/2\pi$ [kHz]	n_{eff}	MSE	$\mathrm{MSE}_{\mathrm{2D}}$
−150	200	400	17	0.08	5.90×10^{-4}	2.12×10^{-4}
−149	184	180	18	0.22	7.80×10^{-4}	3.55×10^{-4}
−148	169	160	22	0.29	5.14×10^{-4}	2.49×10^{-4}
−147	150	150	25	0.31	5.36×10^{-4}	2.57×10^{-4}
−146	106	100	24	0.41	4.34×10^{-4}	2.49×10^{-4}
−145	81	112	17	0.40	2.88×10^{-4}	1.94×10^{-4}
−144	50	100	19	0.68	1.99×10^{-4}	1.56×10^{-4}
−143	87	95	20	0.73	1.52×10^{-4}	1.26×10^{-4}
−142	65	100	24	0.99	1.58×10^{-4}	1.22×10^{-4}
−141	55	80	24	1.37	0.99×10^{-4}	0.99×10^{-4}
−140	84	80	29	1.50	0.90×10^{-4}	1.01×10^{-4}
−139	60	67	29	1.75	0.77×10^{-4}	1.05×10^{-4}
−138	25	84	30	3.57	0.69×10^{-3}	0.78×10^{-4}
−137	23	71	30	3.84	0.54×10^{-4}	0.78×10^{-4}
−136	30	86	35	5.27	0.77×10^{-4}	0.89×10^{-4}

Table C.2: **Optimized Parameters for TLS,C1 Simulations**. The listed parameters were used to simulate the master equation and achieve a close match to the experimental data shown in Fig. 5.10. MSE values represent the error calculated for fixed DC bias in Fig.5.10C, while $\mathrm{MSE}_{\mathrm{2D}}$ corresponds to the errors associated with the spectra in Fig.5.10B.

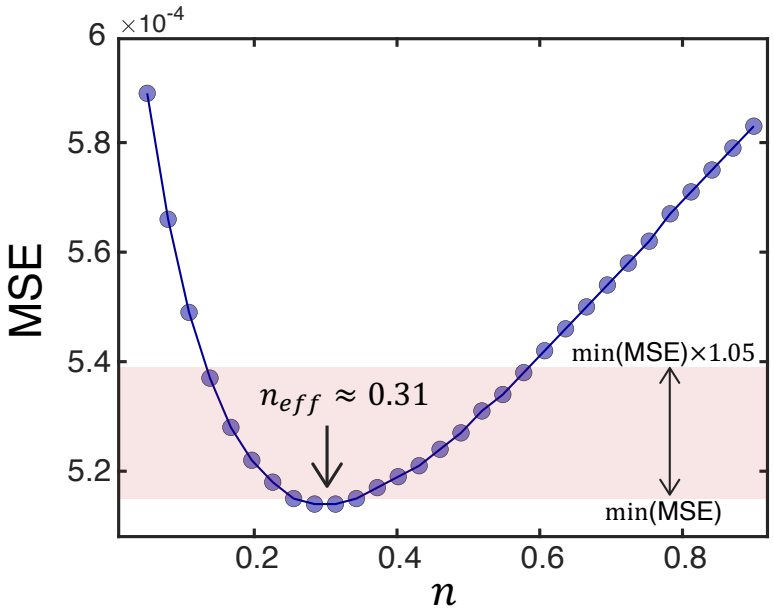

Figure C.1: **Characterization of** 5% **Tolerance Criterion for** n_{eff}**.** The plot displays the mean squared error (MSE) as a function of the estimated phonon number n. After iterative minimization of the fitting parameters, we sweep n around the optimized n_{eff} value to quantify the uncertainty in our estimation. This sweep identifies the regions $n < n_{eff}$ and $n > n_{eff}$ where the MSE increases by 5% above its minimum value (indicated by the shaded area). Notably, the error rises more steeply for $n < n_{eff}$ than for $n > n_{eff}$, as expected due to the $\sqrt{n}$ scaling of the energy levels. As n_{eff} increases further, achieving an accurate determination becomes increasingly challenging and computationally expensive.

Appendix D

DETAILS OF RESOLVING RANDOM TELEGRAPH SIGNALS

To analyze the RTS data, we calculate the probability distribution of the amplitude response using kernel density estimation (KDE) [138], as mentioned in the main text. This method provides a smooth estimate of the underlying distribution, allowing us to resolve closely spaced peaks in the presence of RTS. Once these peaks are identified, each point in the amplitude time trace is assigned to the nearest peak, producing a ladder plot (see red line, Fig. 5.20A) that reveals when the system transitions between states.

Once the two-valued ladder plot is constructed, we can easily determine the switching instants and corresponding dwell times—that is, the durations for which the system remains in each state (i.e., classical or quantum).The switching rate, λ, for each process is determined by applying a maximum-likelihood estimation (MLE) procedure to the raw, unbinned dwell times, fitting them to an exponential function. The uncertainty is derived from the 95% confidence interval of the MLE fit. These dwell times are then binned using Scott's rule [139] to produce a histogram that is normalized to form a probability density function, ensuring that the total area under the histogram equals unity. For the analysis presented in Fig.5.20B, the RTS data was taken from a dedicated 10-minute measurement with the on-resonance drive to serve as a high-quality benchmark for our fitting procedure. For other analyses, such as systematic sweeps, shorter acquisition times (20-120s) were implemented. These durations were found to be sufficient to resolve the probability distribution and observe the trend of the switching rates as a function of the sweep parameter.

INDEX